

THE INFLUENCE OF ROCK PROPERTIES ON BEDROCK AND SEDIMENT
ERODIBILITY IN RIVERS

AS
36
2012
GEO
.B49

A thesis submitted to the faculty of
San Francisco State University
In partial fulfillment of
The requirements for
The degree of

Master of Science
In
Geosciences

by

Jonathan David Beyeler

San Francisco, California

December, 2012

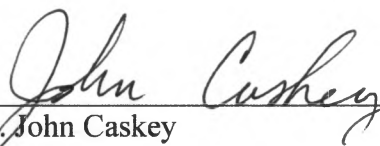
Copyright by
Jonathan David Beyeler
2012

CERTIFICATION OF APPROVAL

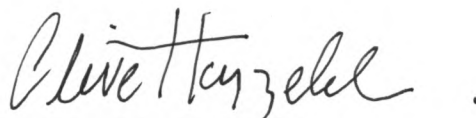
I certify that I have read *The Influence of Rock Properties on Bedrock and Sediment Erodibility in Rivers* by Jonathan David Beyeler, and that in my opinion this work meets the criteria for approving a thesis submitted in partial fulfillment of the requirements for the degree: Master of Science in Geosciences at San Francisco State University.



Dr. Leonard S. Sklar
Professor of Geosciences



Dr. S. John Caskey
Professor of Geosciences



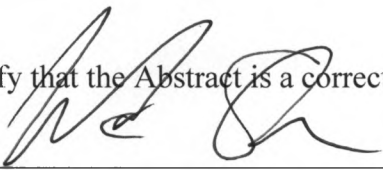
Dr. Clive Hayzelden
Manager of SFSU Electron Microscopy Facility

THE INFLUENCE OF ROCK PROPERTIES ON BEDROCK AND SEDIMENT
ERODIBILITY IN RIVERS.

Jonathan David Beyeler
San Francisco, California
2012

Erosion of landscapes depends on the physical and chemical attack on rock and the resistance to breakdown by bedrock and sediment. Physical erodibility of bedrock has been shown experimentally to scale with the square of tensile strength, but this correlation has not yet been extended to sediment or field predictions of breakdown. This work combines experimental studies and fieldwork to investigate the role of rock properties in bedrock erodibility and sediment comminution from fluvial transport, using lithologies spanning the variation of rock properties found in the field. The laboratory studies use rock property measurements to investigate variations in experimentally measured bedrock erosion rates and sediment abrasion rates. Scanning electron microscopy is used to investigate textures resultant from different erosional processes and the evolution of rock surface textures through sediment abrasion. In the field where lithologic contacts create discrete upstream source areas of distinct rock types, the evolution of sediment size distributions due to particle breakdown downstream of the contacts can be scrutinized. Field results are compared with laboratory tensile strength measurements and tumbling abrasion rates to distinguish in the field between sorting and comminution and to estimate field size reduction due to breakdown. This lab work shows the erodibility of bedrock and sediment varies systematically with tensile strength and mineral grain size, not elasticity. These field and lab results may be useful in developing theory for predicting sediment comminution rates and to help establish an empirical scaling relationship between the relative and absolute erodibility of bedrock and sediment.

I certify that the Abstract is a correct representation of the content of this thesis.



Chair, Thesis Committee

Dec. 14, 2012

Date

ACKNOWLEDGEMENTS

This thesis would not have been possible without the vast support and encouragement of my advisor, Dr. Leonard Sklar. I would also like to thank Dr. Bill Dietrich for allowing me to use laboratory space at the UC Berkeley Richmond Field Station for these experiments. I would also like to show my gratitude to the members of my thesis committee, Dr. John Caskey and Dr. Clive Hayzelden, for their expertise and feedback to help improve the content of this thesis. I would again like to thank Dr. Hayzelden for his much-needed assistance with SEM work. I also owe much gratitude to my sisters for family support throughout these last couple years. Additionally, I would like to thank Stuart Foster for all of his laboratory assistance in apparatus fabrication and maintenance. Finally, I am indebted to my many colleagues for their assistance in all aspects of life from lab and field work to matters of the heart: Russell MacArthur, Eric Donaldson, Kim Litwin, Peter Polito, Joe Farrow, Forrest Horton, Larry Alden, Claire Lukens, and Erin Stacy.

TABLE OF CONTENTS

LIST OF TABLES	viii
LIST OF FIGURES	ix
LIST OF APPENDICES	xi
1. Introduction.....	1
1.1 Rivers Drive Landscape Evolution	2
1.2 Previous Work on Erodibility	3
1.3 Influence of Rock Properties: Questions and Hypotheses	5
1.4 Overview of Thesis	6
1.4.1 Reanalysis of Previous Erosion Experiments	7
1.4.2 Sediment Abrasion Experiments	8
1.4.3 Laboratory to Field Scaling	9
2. Bedrock Erosion	10
2.1 Fracture Mechanics Theory	12
2.2 Tensile Behavior of Rocks	13
2.2.1 Scale Mismatch Between Fracture and Abrasion	15
2.3 Modeling Relative Bedrock Erodibility	16
2.4 Methods for Quantifying Rock Properties	17
2.4.1 Bedrock Abrasion Mills	17
2.4.2 Strength Measurements: Brazilian Splitting Test	18
2.4.3 Mineral Grain Size	19
2.4.4 Porosity and Density	20
2.4.5 Elasticity	21
2.4.6 Scanning Electron Microscopy Work	22
2.4.6.1 SEM Sample Preparation	22
2.4.6.2 Carl Zeiss Field Emission Ultra 55 SEM	23
2.5 Results	25
2.5.1 Material Properties	25
2.5.2 Modeling Bedrock Erodibility	26
2.5.3 SEM and Erosional Process	29
2.6 Discussion	31
2.6.1 Main Findings	31
2.6.2 Implications and Predictability	32
2.6.3 Limitations	32
2.6.4 Next Steps	33

3.	Sediment Abrasion.....	34
3.1.1	Downstream Fining of River Sediment	35
3.1.2	Modeling Sediment Abrasion with Rock Properties	37
3.2	Methods.....	38
3.2.1	Measuring Rock Properties.....	38
3.2.2	Barrel Tumbling Experiments	38
3.2.3	SEM to Investigate Surface Wear.....	39
3.3	Results	40
3.3.1	Tumbling Experiments	40
3.3.2	Modeling Results	41
3.3.3	Insight from SEM Anaglyphs	43
3.4	Discussion	44
3.4.1	Main Findings	44
3.4.2	Implications and Predictability	45
3.4.3	Limitations	46
3.4.4	Next Steps	46
4.	Laboratory to Field Scaling	47
4.1	Introduction	47
4.1.1	Bedrock Incision	47
4.1.2	Setting for a Natural Experiment	48
4.1.3	Dinkey Creek Field Site.....	49
4.1.4	Theory for Proposed Scaling Relationship	50
4.2	Methods to Estimate Abrasion in the Field.....	51
4.3	Results	53
4.3.1	Pebble Counts in Dinkey Creek.....	53
4.4	Discussion	54
4.6.1	Main Findings	54
4.6.2	Lab to Field Scaling	54
4.6.3	Exerimental Limitations	55
4.6.4	Future Research Needs	55
5.	Lab and Field Synthesis.....	57
5.1	Summary and Conclusions.....	57
5.2	Future Research Needs.....	59
6.	References.....	61

LIST OF TABLES

Table	Page
1. Rock Properties of Rocks Used in Bedrock Erosion Experiments.....	65
2. Metric Results from Modeling Bedrock Erosion With Rock Properties	66
3. Rocks and Properties from Tumbling Experiments.....	67
4. Results from Modeling Sediment Abrasion With Rco Properties	68
5. Pebble Count Data from Dinkey Creek, CA.....	69

LIST OF FIGURES

Figure	Page
1. Source to sink schematic.....	70
2. Pictures of alpine river and sediment.....	71
3. Pictures of sediment as tools and alluvial cover.	72
4. Log-log regression of erosion rate with tensile strength.....	73
5. Thin Sections of Rocks Used in Erosion Experiments.	74
6. Location Map of field study.....	79
7. Bedrock Abrasion Mill schematic.	80
8. Strain energy plot.....	81
9. Results of weathering on strength properties of granites.....	82
10. Updated and annotated log-log plot of erosion rate versus strength.....	83
11. Tensile strength and porosity samples.	84
12. Tinius Olsen and tensile strength experimental setup.....	85
13. Photomicrograph as grain map in ARCGIS.	86
14. Drying oven in Hensill Hall Room 112.....	87
15. Resonant frequency tester setup for elasticity measurements.....	88
16. Carl Zeiss Ultra-55 Field Emission SEM.	89
17. SEM images of un-tilted and tilted sandstone.	90
18. Log-log regression of erosion rate vs tensile strength by rock type.	91

19. Cumulative mineral size distributions of bedrock data set.	92
20. Schematic of K.....	93
21. Results from modeling erosion as 4-parameter model.	94
22. Covariation of Bedrock Properties.....	95
23. SEM Images of Porous Bedrock Erosion and Fracture Surfaces.	96
24. SEM Images of Crystalline Bedrock Erosion and Fracture Surfaces.	97
25. Schematic of downstream fining	98
26. Thin Sections of Rocks Used in Tumbling Experiments.....	99
27. Picture of tumbled rock types from the Sierra Nevada, CA.	102
28. Barrel and tumbling setup used for abrasion experiments.....	103
29. Schematic cross-section of barrel tumbler.....	104
30. SEM Images of Tumbled Rocks.....	105
31. Anaglyph creation from SEM stereopair images of rock surfaces.	106
32. Plot of total mass in tumbling barrel versus distance.	107
33. Measured abrasion rates plotted versus tumbling distance.....	108
34. Experimentally measured abrasion rates vary with strength.	109
35. Cumulative mineral size distributions of sediment data set.....	110
36. Results from modeling abrasion rates with strength and grain size.....	111
37. SEM Anaglyphs of Tumbled Rock Surface Textures.....	112
38. Covariation of Sediment Properties.....	115

39. Schematic of lithologic restriction to sediment source.....	116
40. Xenolith in igneous intrusive rock.....	117
41. Generalized geologic map of Dinkey Ck field area.....	118
42. Miwok grinding pits in channel margin of Dinkey Creek.....	119
43. Headwaters of Dinkey Creek.....	120
44. Topographic map of Dinkey Creek field area, CA.....	121
45. Pebble-count locations along Dinkey Creek.....	122
46. Photos of pebble-count sites along Dinkey Creek.....	123

LIST OF APPENDICES

Appendix	Page
1. JMP statistical output for multivariate models of erodibility.	124
2. JMP statistical output for multivariate models of sediment abrasion.	131

1. Introduction

Erodibility is a term used for over a century to describe how prone a material or rock substrate is to physical breakdown and mass loss through erosion (*e.g. Gilbert, 1877; Hack, 1973, 1975; Stock and Montgomery, 1999; Dietrich et al., 2003*). Since the days of G.K. Gilbert, researchers have used erodibility to qualitatively compare rock resistance to erosion, typically in terms of hard or soft. However erodibility is generally treated as an immeasurable quantity (*e.g. Whipple and Tucker, 1999; Willett, 2010*). The erodibility of rock plays an important role in governing what rocks are present at the surface of the Earth and the duration of time they remain there; from the resistant boulders and gravel in rivers to the alpine peaks and canyons surrounding river basins. Mountains have river networks that flow from upland regions to lakes and seas through basins and flood plains where much of the global population lives, schematic shown in Figure 1 (*from Allen, 2008*). The riverbeds have sediments (i.e., any mobile particles eroded from bedrock) that are periodically conveyed downstream when runoff events of sufficient magnitude occur. The sediment carried in rivers plays a vital role in many natural systems, from cobbles and boulders that provide fish habitat to the tools necessary for river incision (Figure 2) (*e.g. Heggenes, 1988; Sklar and Dietrich 1994; Sklar et al., 2006*).

1.1 Rivers Drive Landscape Evolution

Rivers drive landscape evolution through incision into bedrock and the downstream transport of material eroded from the surrounding watershed (*e.g. Beaumont et al., 1992; Howard et al., 1994; Whipple, 2004*). River incision can be described from two perspectives, the erosive attack and the resistant defense. The first perspective is the fluvial attack waged by rivers and sediment on bedrock, whereas the second is the rock and sediment resistance to physical erosion. The sediment in rivers plays a vital role in eroding the bed by providing both tools and cover depending on supply (Figure 3). The mixture of sediment carried by a river reflects a jumble of upstream processes, including particle production, size-selective mobility, comminution, and size reduction from collisions in transport. The grain size distribution of river sediments is ultimately governed by the initial headwater supply, resupply from adjacent hillslopes, sediment mixing at confluences, and breakdown in transport (*e.g. Kodama, 1994; Pizzuto, 1995; Heller et al., 2001; Sklar et al., 2006*). In many rivers the distribution of sediment mostly reflects proximal hillslope resupply, but abrasion and comminution in transport are expected to have some influence (*Sklar et al., 2006*). Rates of abrasion from grain-grain interactions in various types of transport (*e.g., eolian, fluvial, granular flow*) show a dependence on strength, shown experimentally by many researchers (*e.g. Attal and Lavé, 2009; Abbot and Peterson, 1978; Sklar and Dietrich 2001*). Laboratory abrasion experiments have shown that rates of size reduction vary by rock type, and with many

lithologies happens through fine-sediment production (e.g. *Kodama, 1994; Lewin and Brewer, 2002; Attal and Lavé, 2009*).

1.2 Previous Work on Erodibility

Despite a wealth of field studies and laboratory experiments on erodibility it remains difficult to predict erodibility beyond simple lithologic and durability classifications (e.g., *Attal and Lavé, 2009; Abbott and Peterson, 1978*). For many years field studies have been done comparing erodibilities of various global settings to investigate landscape evolution. For example, much of the difference in relief and hillslope angle between the rugged Alaskan Range and the adjacent low-lying foothills is attributed to lithologies of very different erodibility (*Ward, 2012*). In the French Alps *Schlunegger et al. (2001)* found that a shift in erosion rates through time could be explained simply by a drastic shift in the erodibilities of the exposed bedrock being eroded from the European Central Alps. Many researchers have modeled landscape evolution by glacial and fluvial erosion with expressions that often have a “black box” erodibility constant or exponent, containing information about lithology, rock strength, etc. However these terms are generally treated as tunable model parameters opposed to empirically determined or directly measurable values.

Downstream fining of bedload sediment in rivers is a widely observed phenomenon, but in the field the influence of particle breakdown on grain size

distributions is largely unknown and difficult to distinguish from other controlling factors, such as selective transport and sediment resupply. Many experimental erosion studies have modeled both the fluvial erosion of bedrock and the comminution of sediment in transport. Sklar and Dietrich (2001) found that for a comprehensive set of 22 rock types, laboratory measured erosion rates strongly scale with the square of tensile strength. However due to an order-of-magnitude variability in erosion rate for a given tensile strength, or respectively in tensile strength for a given erosion rate, strength alone does not directly dictate the erodibility of bedrock. Granular-flow transport (tumbler and flume) and erosional studies (Hsu *et al*, 2008) have similar findings that erosional efficiency is strongly related to strength. Previous material science studies have presented expressions for the erodibility of polycrystalline brittle synthetic materials (i.e. metals and ceramics), including relationships between tensile strength, grain size, and porosity, but to my knowledge this understanding has not yet been applied to real rocks (Knudsen, 1958). Even with all the previous work that has been done it is still unknown how to scale from laboratory experiments to field erosion estimates for both bedrock and sediment.

1.3 Influence of Rock Properties: Questions and Hypotheses

This work aims to elucidate both the processes of bedrock erosion by abrasion from sediment and the physical size reduction of sediment in rivers due to breakdown through transport. In this study I ask the following questions:

1. Can I predict the erodibility of bedrock and sediment in rivers by coupling rock properties?
2. Is it possible to scale from laboratory studies of relative rock erosion and sediment abrasion to absolute field estimates?
3. What can be learned about the relationship between surface roughness and travel distance from examining rock surfaces with scanning electron microscopy?

I have the following hypotheses:

1. Fracture mechanics theory suggests erodibility of bedrock and sediment should depend on rock properties, such as median grain size, porosity, density, and potentially elasticity.
2. If it is possible to estimate particle breakdown in the field, then I can compare field estimates to relative lab rates of tumbling breakdown to look for a scaling relationship.
3. Different processes, such as fracturing versus abrasion, should produce different textures, visible at the nanometer scale with SEM.

Sklar and Dietrich (2001) found that laboratory measured bedrock erosion rates scale inversely with the square of rock tensile strength, but with an order-of-magnitude variability about the best-fit power law (Figure 4). Including other rock properties in an erodibility model could explain the remaining variance in tensile strength for a given erosion rate.

1.4 Overview of Thesis

This work is comprised of three separate but related erosional studies (two parts laboratory and one part field study) and has three kinds of data: previously published, unpublished and supplemented; as well as SEM imagery work. I present a reanalysis of the material properties of the rocks used in previous bedrock erosion experiments by Sklar and Dietrich (2001) as well as new rock types with unpublished data. I measured abrasion rates of 5 new lithologies in laboratory tumbler experiments to investigate sediment comminution from grain-grain interactions in granular flows to combine with unpublished data from two previous student theses by Joe Farrow and Peter Polito. I conducted field work in the Sierra Nevada Mountains, CA, consisting mostly of pebble counts, to study two closely related but independent aspects of rivers; the downstream fining of sediment and particle breakdown resulting from downstream travel. I present predictive power-law expressions, with statistical analysis of model parameters, for both erodibility and abrasion that couples easily measurable rock material properties following

previous studies of polycrystalline brittle metal and ceramic materials (*Knudsen 1958*). Also I present a novel use of scanning electron microscopy (SEM) to investigate silt-production from mass-reducing impacts due to downstream transport at the micron-scale of rock microtextures (e.g., mineral grain size and porosity).

1.4.1 Reanalysis of Previous Erosion Experiments

The first piece of my story is an analysis of the material properties of the rocks eroded by Sklar and Dietrich (*2001*) combining new data with published strength and erosion rates measured in bedrock abrasion mills (BAMs). I investigated the mineralogy, grain size, cement, porosity, density, and elasticity of the previously eroded rocks. Figure 4 shows the data from the erosion experiments of Sklar and Dietrich (*2001*). I used thin sections of the rocks previously eroded by Sklar and Dietrich (*2001*) and the new rocks to investigate differences in the physical characteristics by lithology; such as grain size and cement composition (see Figure 5 for photomicrographs). I measured tensile strength, elasticity, mineral grain size, density and porosity, in order to form an expression for erodibility by coupling rock properties and microtextures, similar in form to the strength expression presented by Knudsen (*1958*). Using SEM, I compared the surfaces of eroded and freshly fractured rock to examine the mechanistic differences between silt-production from abrasion and fracturing rock through compressional loading.

1.4.2 Sediment Abrasion Experiments

In the second study I performed granular-flow tumbling experiments with new rock types to measure sediment abrasion rates by lithology (combined with unpublished data from previous SFSU student theses by Joe Farrow and Peter Polito) and to investigate variations in relative abrasability by microtexture. I sampled quartzite, biotite hornfels, granite, granodiorite, and diorite from the Sierra National Forest in the Sierra Nevada Mountains, CA, and combined them with a set of previously tumbled rock types; many of which are also present in the bedrock data set. This work presents an expression coupling material properties (e.g., tensile strength and mineral grain size) to model the measured abrasion rates. This expression is similar in form to that of erodibility and can be used to predict relative abrasion rates with rock properties. Akin to the bedrock study, I made thin sections and acquired photomicrographs to investigate lithologic differences in cement composition, mineral grain size, porosity and density. SEM was used in the abrasion study to investigate the process of sediment size reduction through the resultant mass removal from sediment interactions in granular flows. SEM was also used to compare the surficial textures of un-tumbled sediment by lithology, as well as textures produced from varying amounts of tumbling and respective erosion.

1.4.3 Laboratory to Field Scaling

The third portion of the work that I present here is a sediment-tracing field study. I investigated the decrease in bedload grain size due to particle breakdown with downstream transport within a Sierra Nevada watershed. In order to investigate downstream fining, I conducted pebble counts to estimate the grain size (median intermediate diameter) of two metamorphic lithologies (quartzite and biotite hornfels) that were transported downstream from a relatively restricted headwater source in Dinkey Creek, CA, a tributary to the North Fork of the King's River in the Sierra Nevada (Figure 6). The grain size data was used to evaluate possible tributary resupply, selective sorting, and estimate field rates of breakdown with downstream transport to compare to the laboratory-measured abrasion rates for the same two rock types.

2. Bedrock Erosion

Lots of field studies have been done to elucidate the processes and mechanisms of bedrock erosion by rivers (*e.g.*, *Beaumont et al., 1992; Howard et al., 1994; Whipple, 2004*). Despite a wealth of understanding on the feedbacks between rock uplift, climate driven erosion, and resistance by rock to the efficacy of river incision and landscape change, erodibility is generally considered immeasurable (*e.g.* *Whipple and Tucker, 1999; Willett, 2010*). Rock erosion in natural landscapes can be conceptually represented as the trade offs between the erosional attack and resistant defense:

$$Erosion = Attack / Defense \quad (1).$$

For decades researchers have done field studies and coupled them to landscape evolution models, such as the stream power erosion model (*Whipple and Tucker, 1999*). In the stream power model local erosion rate is a power-law function of upstream drainage area and channel slope such that river profile evolution can be written in the equation:

$$\frac{dz}{dt} = U(x, t) - Kk_a^m x^{hm} \left| \frac{dz}{dx} \right|^n \quad (2)$$

where dz/dt is the rate of change of bed elevation, U is rock uplift rate (defined relative to base-level), K is a dimensional coefficient of erosion, k_a is a dimensional constant, x is distance downstream, h is an exponent derived from Hack's Law (*i.e.*, drainage area increases downstream), dz/dx represents channel gradient, and m and n are positive constants that reflect erosion processes, basin hydrology, and channel hydraulic geometry

(Hack, 1973,1975; Whipple and Tucker, 1999). Models like the stream power erosion law conceptually lump aspects of both the attack and defense of rock into black-box empirical constants and coefficients, convoluting measurable and relatively immeasurable quantities as tunable parameters (Sklar and Dietrich, 2004, 2006).

Rock resistance to fluvial abrasion by bedload sediment impacts has been shown experimentally by Sklar and Dietrich (2001) to depend on the square of rock tensile strength across the full range of rock strengths encountered in the field. Figure 4 is a log-log regression plot of laboratory measured bedrock erosion rates against tensile strength showing order-of-magnitude variability about the power-law best-fit, particularly for stronger rocks. Figure 7 shows the experimental setup. This scaling with the square of tensile strength is consistent with fracture mechanics theory, which predicts that fractures propagate in brittle materials when the capacity to store impact energy by elastic deformation is exceeded. Strain energy, SE , is the area under the curve in Figure 8 and depends on the square of tensile strength, σ_t , and the elastic modulus, Y :

$$SE = \sigma_t^2 / 2Y \quad (3).$$

In this work I use a comprehensive data set of rock types, composed of rocks previously eroded by Sklar and Dietrich (2001) combined with new data to explain the variability in erosion rate for a given tensile strength, or in tensile strength for a given erosion rate, with other rock material properties. In addition to tensile strength I

investigated elastic modulus, crystal grain size, porosity, cementation, and both rock dry bulk density and solid density.

2.1 Fracture Mechanics Theory

According to fracture mechanics theory, brittle failure occurs in rock when a series of neighboring inherent flaws or microcracks coalesce. The largest inherent flaw in a rock is described as a Griffith crack, whose size is dependent on the mineral grain size and size of pore spaces (*Brace, 1961*). Individual impacts from sediment initiate and propagate small fractures in bedrock mass, often times through mineral grains, along weaknesses such as parting and cleavage planes, and along mineral boundaries (*Brace, 1961; Kumano and Goldsmith, 1982*). Erosion occurs when these small failures conjoin and consequently mass may be removed. Fractures lose less energy and therefore can propagate further through weaknesses in individual crystals or along mineral grain boundaries, opposed to through and around a series of many interlocked crystals (*Brace, 1961*). Griffith crack theory for the behavior of brittle solids says the scale of inherent weaknesses in a rock is set by rock properties (*Brace, 1961; Kumano and Goldsmith, 1982*). This suggests that mineral grain size should have a strong influence on the ability of fractures to propagate through rock, and could explain some of the variability in measured tensile strength for a given erosion rate.

Fractures propagate in a brittle solid when the material can no longer store impact energy by elastic deformation. The largest flaws or microcracks in a rock mass susceptible to tensile failure are often along mineral grain boundaries and between minerals, at the scale of the largest mineral grains and pore spaces (i.e., voids between minerals) (*Brace, 1961; Kumano and Goldsmith, 1982*). Effective porosity (i.e. porosity measured through sample saturation limited by fluid connectivity of voids, not capturing influence of vugs on total porosity) may play an important role in setting the frequency and size of inherent flaws within many rocks, such as clastic or weathered rocks that are naturally porous. This is consistent with previous studies showing an inverse relationship between strength and the degree of weathering of granites due to weathering along grain boundaries and within feldspars and phyllosilicates, introducing porosity to generally low-porosity rocks (i.e., <3%) (*Tuğrül and Zarif, 1999*).

2.2 Tensile Behavior of Rocks

Rocks are typically strongest under compressional loading, but in nature often fracture in shear or under tension as opening-mode fractures pulling rock masses apart. It has long been understood from a material science perspective that the strength of synthetic brittle materials, such as metals and ceramics, is related to grain size and porosity (*Kumano and Goldsmith, 1982; Knudsen, 1958*). *Brace (1961)* showed that the tensile strength of crystalline limestone could be predicted from the mineral grain size, by

assuming the largest grains define the size of the largest inherent weaknesses in the rock, in the relationship:

$$T_0 = (2 Y \gamma / \pi a)^{1/2} \quad (4)$$

where T_0 is tensile strength, Y is Young's modulus of elasticity, γ is specific surface energy, and a is the half-length of the Griffith crack. The scale of the Griffith crack is set by mineral grain size, therefore tensile strength is inversely proportional to the square root of grain size, a . Similarly, Merriam et al. (1970) found that the tensile strength of granites is inversely proportional to quartz content and can be predicted from mineral texture. Rocks with high quartz content tend to have an aplitic texture characterized by many small grains with little interlocking or intergrowth, whereas rocks with low quartz content tend to be coarser grained with interlocking feldspar prisms (Merriam et al., 1970). Tuğrul and Zarif (1999) studied the mechanical and physical properties of a variety of granitic rocks from Turkey and found significant correlations between tensile strength and mineralogy, measured as quartz-to-feldspar ratios. Results from Tuğrul and Zarif (1999) show that in granitic rocks as the abundance of quartz increases, the abundance of feldspars decreases, corresponding with an increase in strength. The shift from feldspars to quartz abundance corresponds with less grain interlocking but more directly, finer grain size (Tuğrul and Zarif, 1999). Tuğrul and Zarif (1999) show that uniaxial compressive strength is correlated with many rock properties including

mineralogy, tensile strength, grain size, and porosity; as well as modulus of elasticity, Schmidt Hammer Value, and point-load strength index.

Vasconcelos et al. (2008, 2009) found that weathering of granites greatly decreases strength by increasing inter-grain porosity and show an inverse relationship between critical crack opening (measured in mm) and tensile strength, as well as elastic modulus (Figure 9). These results are similar to previous findings from studies of synthetic brittle solids showing a relationship between strength, grain size, and porosity but have yet to be coupled in an expression for rock erodibility.

2.2.1 Scale Mismatch Between Fracture and Abrasion

Results from previous studies (*Sklar and Dietrich, 2001*) suggest a mismatch between the length scale of fractures that propagate through rock under tension and that of microcracks that coalesce during abrasion by sediment impacts that erode rock mass. Sklar and Dietrich (2001) noted that the BAMs became murky during the erosion experiments as evidence of fine sediment production, on a scale fundamentally smaller than the mineral grain scale of most rocks (except fine-grained rocks such as some limestones, marbles, siltstones, mudstones, claystones). This scale mismatch suggests that rock microtextures may play a key role in explaining the variation in tensile strength for a given erosion rate. Grain size is hypothesized to be influential among the non-porous rocks (e.g., unweathered igneous and many metamorphic rocks), whereas porosity

might couple with grain size as explanatory variables for the porous (e.g., sedimentary and weathered) rock types.

2.3 Modeling Relative Bedrock Erodibility

Erosion rates, E , scale with the square of tensile strength, σ_t , shown by results from Sklar and Dietrich (2001) with additional data in Figure 10 and modeled as:

$$E^{-1} = k (\sigma_t^2) \quad (5).$$

This equation is logarithmically transformed from linear form:

$$\log(E) = k + c_1 \log(\sigma_t) \quad (6)$$

where c_1 is 2 according to results from Sklar and Dietrich (2001). Brittle failure in rocks depends on the bulk strength properties but following fracture mechanics theory and results from previous studies, should also depend on the elastic properties, measured as Young's modulus of elasticity, Y (Tuğrul and Zarif, 1999). Strain energy combines strength and Young's modulus in Equation 3. Modeling bedrock erosion with strain energy in the form of Equation 5 suggests the equation:

$$E^{-1} = k (\sigma_t^2 / Y) \quad (7).$$

Fracture mechanics and toughness theory describe crack growth as the mechanism for tensile failure, an initial length scale dependent on mineral grain size. Following Griffith theory for the fracture behavior of brittle solids and incorporating the square of grain size, D , yields:

$$E^{-1} = k(\sigma_t^2 / Y)(D^{1/2}) \quad (8).$$

The aforementioned mismatch between the length scale of macro-scale fractures produced in rock through erosion by abrasion with sediment suggests a relationship between strength and grain size. Knudsen (1958) found an inverse relationship between strength and both grain size and porosity for polycrystalline synthetic brittle materials.

This suggests including porosity, n , in the erodibility function for rock:

$$E^{-1} = k(\sigma_t^2 / Y)(D^{1/2})e^n \quad (9).$$

2.4 Methods for Quantifying Rock Properties

2.4.1 Bedrock Abrasion Mills

Sklar and Dietrich (2001) conducted erosion experiments in bedrock abrasion mills (BAMs) using a comprehensive set of 22 rock types spanning the full range of durability encountered in the field. A schematic of the BAMs is shown in Figure 7. 8” diameter cylindrical discs were cut of each rock type and mounted below a cylinder of water with varying amounts of sediment. A propeller attached to an electric motor creates rotational flow in the BAM, initiating sediment saltation and incipient erosion of the bedrock disc. Erosion rates were measured as mass loss over a given experimental run time and were compared to laboratory-measured tensile strengths (Figure 10). Sklar and Dietrich (2001) present a much more comprehensive explanation of the experiments,

including the effects of variable grain size mixtures and amounts of sediment.

2.4.2 Strength Measurements: Brazilian Splitting Test

Tensile strength measurements were made by Sklar and Dietrich (2001), and supplemented with some measurements by myself, to increase the BAM-measured erosion rate data sets. Samples were prepared for the tensile strength tests according to standard specifications for the Brazilian-type splitting tests. Cylindrical cores were cut (~30–50 cm in diameter) of each rock type with a drill press equipped with a diamond-tipped coring bit at the UC Berkeley Richmond Field Station. The cores were trimmed to dimensions of approximately 1:1 (Figure 11) using a diamond tipped lapidary saw at the UC Berkeley Thin Section Lab. Using a set of calipers (with a systematic uncertainty of 0.02 mm) measurements were taken of the length and diameter of each sample (Litwin, 2010). Each rock sample was weighed using an Ohaus Scout Pro scale, with a precision of 0.1 g.

The simplest geometry for tensile failures in rock is in direct tension, or orthogonal to the axis of compression. The experimental setup for Brazilian Splitting tests uses uniaxial compression to induce an orthogonally oriented tensile failure in the test samples. Brazilian tensile strength is estimated by measuring the maximum compressive force needed to induce an orthogonal opening-mode tensile failure by applying quasi-static compression. The maximum compressional force measured for each

rock type in multiple cylinders (i.e. 3–10) using the Tinius Olsen machine in the Engineering Department at SF State University (Figure 12). Second, the maximum compressional force is coupled with the geometry of the cylinder and fracture area to convert to a tensile strength, according to:

$$\sigma_t = \frac{2F_p}{\pi ld} \quad (10)$$

where tensile strength, σ_t , is calculated from the peak force, F_p , applied to the sample at failure; l is the length and d is the diameter of the sample, assuming the fracture deviates little from a plane through the diameter of the cylinder (Figure 12c and 12d) (*Vutukuri, 1974*).

2.4.3 Mineral Grain Size

Grain size data for each rock type was estimated through point-counts of long and short axes of mineral grains on photomicrographs, compiled with ARCGIS. Standard (~6cm x 2cm x 30 μ) thin-sections were prepared by myself in the UC Berkeley Thin-Section Lab and also by National Petrographics Laboratory in Houston, TX, in order for me to examine mineralogy and measure grain size. I acquired photomicrographs of all the thin-sections at SFSU with the help of Dr. Mary Leech and her microscope and camera. Following Bunte and Abt (2001), I did point-counts on the photomicrographs using the grid-by-number method, which requires no correction when converting from

the 2-dimensional image to a volumetric representation of the sample because the conversion factors cancel out (i.e., $D^{-3} * D^3$).

The point-counts were done with ARCGIS by treating each photomicrograph as a map, overlaying a grid over the image, and measuring the length of the major and minor mineral axes under each grid node. Figure 13 shows photomicrographs as grain-maps. The lengths were measured in pixels and tabulated in a database by ARCGIS, and then exported to JMP for statistical analysis. I converted the pixel measurements to meters using a scaling factor determined from photos of a mm ruler.

2.4.4 Porosity and Density

I prepared small cylindrical core samples (~100g samples shown in Figure 11) of all of the bedrock types (in Table 1) and submerged them in water at standard room temperature and atmospheric conditions until saturated. I determined the rocks were saturated when they ceased absorbing water, measured as no additional gain in mass (g). While wet, surface water was removed with a hand towel and the saturated rock masses were measured with an Ohaus scale, with associated error of 0.05 grams in Dr. Petra Deken's lab at SFSU. The volume of each sample was measured in volumetric glassware by water displacement (error from uncertainty in glassware is $\pm 0.5\%$). I dehydrated the saturated samples in a standard drying oven (Figure 14) at ~140 degrees Celsius and reweighed them. I compared the wet and dry weights for each measured volume of rock

to get the absorbed mass of water, normalized by the density of water, and expressing porosity, n , as a percentage:

$$n = [(mass_{wet} - mass_{dry})/\rho_{H2O}]/volume_{wet} * 100 \quad (11)$$

With this method, I also estimated the dry bulk density of the rocks:

$$\rho_{rock} = mass_{dry} / volume_{wet} \quad (12)$$

This method measures the “effective porosity” of the lithotypes, and is limited by both permeability and the lack of natural conditions (i.e., temperature and pressure) but yields representative values (*Tuğrul and Zarif, 1999*).

2.4.5 Elasticity

Fractures propagate through rock often due to compression or tension, but many rocks experience elastic deformation prior to failure. Uniaxial compression of rocks causes expansion (i.e. strain) in the perpendicular directions. This stretching is measured as Poisson’s ratio, which compares the amount of axial shortening due to the applied pressure to the amount of resulting perpendicular strain. Young’s modulus is the slope of the line that defines strain energy, which is the area under the curve on a stress versus strain diagram (Figure 8). Young’s modulus of elasticity for the rocks in the data set was measured in one of two ways to study variations in the brittle behavior of the rocks eroded in BAMs by rock type. Joel Johnson estimated the elastic modulus of a subset of the rocks acoustically from measurements of the velocity of ultrasonic pulses through

core samples, at MIT/NER (labeled in Table 1 part A). For the remainder of the rocks in the data set, I used a resonant frequency tester to measure vibrations in a cylindrical sample induced by an operator with a small hammer, as shown in Figure 15. The resonant frequency tester is a simple setup, composed of a handheld computer connected through a wire to an accelerometer, which is affixed with putty to a cylindrical rock sample (length-to-width ratios of ~3–5:1 are desirable). The resonance tester is capable of three forms of frequency measurements in either the longitudinal, transverse, or torsional directions. I made longitudinal measurements, as shown in Figure 15b. Dynamic Young's Modulus, Y , is calculated in the longitudinal direction from the following equation:

$$Y = 5.093(L/d^2)M(n')^2 \quad (13)$$

where M is mass (kg), n' is the measured fundamental frequency (Hz), L is the core length (m), and d is the diameter (m) (*ASTM Standard C215, 2008*).

2.4.6 Scanning Electron Microscopy Work

2.4.6.1 SEM Sample Preparation

SEM is an emerging tool for understanding fine-scale surface textures on various materials (e.g., paper, quartz sand grains, artifacts) such as the impacts that smooth sand grains in Aeolian processes and abrasion scars on artifacts and bone (e.g. *Russ and Russ,*

1987; Banerjee et al., 2009). I sampled eroded bedrock surfaces from the BAM discs previously used by Sklar and Dietrich (2001) to investigate the textures produced from different processes such as mass removal by sediment abrasion or fracture through tensile failure. I cut cubic samples from the eroded surface of the discs and mounted them to standard 1 cm aluminum SEM stubs with colloidal silver paint. Mounted specimens were coated with a ~15nm layer of evaporated carbon, using a Cressington Carbon Evaporator, to electrically ground the rock surfaces to the metal stub. The eroded bedrock surfaces were compared to fractured surfaces, resulting from opening-mode tensile failures for the same respective rock type, prepared following the same procedures.

2.4.6.2 Carl Zeiss Field Emission Ultra 55 SEM

I used the Carl Zeiss Field Emission Ultra 55 SEM in the SFSU Electron Microscopy Facility for the SEM work in this thesis (Figure 16). SEM uses an electron beam to examine very small features (i.e., nanometer to micron scale) on specimen because the topographic representation of the surface is coupled with a large depth of field to produce a 2-dimensional image that appears to be 3-dimensional representation of topology and topography (peaks and valleys). Figure 16b shows a schematic of the Zeiss booster electron column. Sending high amounts of voltage (i.e., 1–30 KeV) through a source in a vacuum at the top of the column generates an electron cloud. This cloud is electromagnetically focused into a beam through a series of apertures and lenses and shot

down through the column at the stage in the vacuum chamber. The interaction between the primary electrons in the beam and the molecules in the specimen produces many kinds of electrons (e.g., backscattered, auger, etc.) but the main type used for SEM imagery in this work is secondary electrons (SE2). I investigated and imaged fractured and abraded rock surfaces with the Everhart-Thornley detector at accelerating voltages of 10–20 KeV and typical working distances of 7-10 mm (Figure 16c, inset of rock in chamber thru TV camera mode).

Secondary electrons are defined as low energy electrons produced from the interactions between the primary electrons bending towards and around molecules in the specimen. SEM imagery is produced by different detectors on the side of vacuum chamber or within the column that detect the electrons emitted from the specimen as the electron beam rasters across the surface (example of tilted and un-tilted abraded sandstone in Figure 17). Due to the low energy of SE2 electrons, they are only emitted from the specimen when produced very close to the surface, lending to the pseudo 3-dimensionality of the topography and high resolution of small-scale features in SEM images. The interaction volume between the incoming electron beam and the specimen takes the shape of a teardrop due to scattering of electrons within the molecular matrix of the specimen. The contrast in SE2 images is largely due to the orientation of features on the specimen surface with respect to the detector. This is seen in Figure 17a from the perspective of looking down the electron column as the detector seemingly illuminates

the topography of the sandstone optically (thin section LI in Figure 5) producing brightness and shadows, highlighting edges of mineral grains and surficial roughness features. High brightness areas are largely due to many SE2 electrons escaping easily from small features on the surface that are angled toward the detector. Figure 17b shows the same abraded sandstone after being tilted, effectively directing the electron emission towards the SE2 detector.

2.5 Results

2.5.1 Material Properties

I measured median mineral grain sizes (D50), porosity, density, and elasticity to explore variations in the erosion rates from previous BAM experiments by rock type (Table 1). In Figure 18 the full data set is highlighted by rock type (i.e., igneous, sedimentary, and metamorphic) and cement type (i.e., silica versus calcite) in a log-log regression of erosion rate versus tensile strength. Figure 5 displays the photomicrographs and shows the variation in grain size and porosity (black interstitial space in photomicrographs) by rock type for the full bedrock data set. Cumulative mineral size distribution curves are shown in Figure 19. The mineral size variation of the rock types spans two orders of magnitude and the statistical analysis (i.e., D50, 10th quantile D10, 90th quantile D90) is shown in Table 1.

The porosity values vary from less than a single percent in some of the finest grain crystalline rocks, such as andesite, greenstone, quartzite, limestone, and schist (A, G, TQ, LL, TA from Figure 5), to roughly 22% in sandstones from the Colorado Plateau (LI and PS). The densities span a natural range from less than 2.4 kg/m^3 for many of the Colorado Plateau sandstones (KSS, WSA, PS, RS, UR, LI from Figure 5) to greater than 2.8 kg/m^3 for greenstone and basalt. The rocks span a wide range of elasticity from $\sim 1 \text{ GPa}$ for greywacke (HS) to 94 GPa for greenstone (G), shown in Table 1.

2.5.2 Modeling Bedrock Erodibility

In this section I present the results from both theoretical models and best-fit multivariate regression modeling of the BAM measured bedrock erosion rates using measured rock properties, for a data set supplemented from Sklar and Dietrich (2001). Table 1 displays the measurements of tensile strength, elasticity, mineral grain size, porosity, and density for the rock types from the bedrock erosion experiments. Figure 10 is log-log plot of erosion rate versus tensile strength. The negative slope of the best-fit line shows that erosion rates decrease as tensile strengths increase, or inversely high relative erodibility corresponds with low tensile strength. The best-fit slope (-2) corresponds with fracture mechanics theory showing that erosion scales with the square of tensile strength. However there is no expectation for the intercept of the best-fit line. By assuming the best-fit line represents the theoretical prediction for erosion based on strength, moving

the best-fit line allows for an investigation of the spread in the data in terms of distance from the best-fit line, K , shown in Figure 20.

Following the model expectations for relative erodibility laid out in section 2.3, I tabulated the results of log-log multi-variate regression models based on tensile strength alone (*Eq. 5*), strain energy (*Eq. 7*), fracture toughness (*Eq. 8*), and fracture toughness with Knudsen's porosity relation (*Eq. 9*). The metrics that I used to evaluate the models are the explanation of variance (R^2 value), significance (%), and the 95% confidence prediction interval (integer in logarithmic scale), shown in Table 2 for the various models. The inclusion of elasticity in a relationship like strain energy does not explain any additional variance in erosion rate for a given tensile strength, in fact it adds scatter to the models; R^2 values decrease from *Eq. 5* ≈ 0.47 to *Eq. 7* ≈ 0.37 , *Eq. 8* ≈ 0.42 , and *Eq. 9* ≈ 0.42 . The prediction interval starts at 2.31 (*Eq. 5*) and increases in all other theoretical cases (2.38). The influence of porosity is greatest among the sedimentary and metamorphic rocks tested here, whereas the igneous rocks tested tend to have low porosities except when weathered, such as the weathered granite (WG in Figure 5) in Table 1. Grain size proves to be influential for all rock types and in all the theoretical models, whereas porosity does not explain any of the remaining information in erosion rate for a given strength measurement in any model.

After testing the theory expectations, I conducted a statistical fishing expedition to find which combination of rock properties best explains the information contained in

erosion rate. Results from multi-variate regression modeling show that grain size and dry bulk density appears along side tensile strength in the best model for relative bedrock erodibility. Figure 21 is a log-log regression of the measured erosion rates versus the proposed model for relative erodibility of bedrock, coupling strength, grain size, and density in the exponential relation:

$$E^{-1} = k (\sigma_t^{1.81} D^{0.47} e^{5.7\rho}) \quad (14)$$

where relative erodibility scales with roughly the square of tensile strength (σ_t), the square root of grain size (D), and rock density (ρ) in place of Knudsen's exponential n .

Figure 22 shows the covariation of the following rock properties: tensile strength, elastic modulus, porosity, density, and grain size measured as D10. Tensile strength varies strongly with elastic modulus, porosity, and density. Elastic modulus varies strongly with tensile strength, porosity, and density. Porosity varies strongly with tensile strength, elastic modulus, and density. Similarly density varies strongly with tensile strength, elastic modulus, and porosity. All of the previously mentioned correlations are significant at greater than 98% with R^2 values ranging from 0.24–0.70, however neither tensile strength, elastic modulus, porosity, nor density covary significantly with grain size. Therefore it is reasonable to believe that including grain size in the erodibility model adds independent information not contained in the tensile strength relation.

2.5.3 SEM and Erosional Process

Four rock types that were previously eroded by Sklar and Dietrich (2001) were selected for SEM analysis of the rock surface textures, produced through erosion in the BAMs, across gradients in rock properties and microtextures. Figure 23 compares SE2 images of Mode-1 tensile-fractured and BAM-eroded surfaces for a porous arkosic sandstone (LI in Table 1) and a nonporous quartzite (Q in Table 1), for an examination of textures by rock type (e.g., roughness at the individual mineral scale or smoothing at the scale of silt-production) with varying rock microtexture, specifically porosity and grain size (e.g., Knudsen, 1958). Similarly Figure 24 compares SE2 images of a fine-grained basalt (rock # in Table 1) and a coarse-grained granite (rock # in Table 1) to look at the influence of mineral grain size. Each fractured rock surface shows roughness relief at the individual mineral scale, whereas each respective abraded rock surface shows the emergence of a planar, smoothed erosional surface. The roughness relief of the smoothing on each abraded surface is at the scale of silt-production (~2–63 μm) evidenced by Figures 23b and 23d, as well as 24b and 24d. The fractured sandstone shows conchoidal fractures along grain boundaries and mineral surfaces and the failure plane appears to utilize void spaces, consistent with fracture mechanics theory. This is contrasted with the eroded sandstone that displays the emergence of a smoothed, planar erosional surface, emphasizing the inherent pore space weaknesses and highlighted by tilting the rock sample (Figure 23b). The quartzite has very similar mineralogy to the

sandstone but is far less porous, and displays conchoidal fractures predominantly along grain boundaries versus the erosional smoothing of saltation-abraded surface, in lieu of preexisting fractures shown in Figures 23d.

Figure 24 highlights the influence of grain size on tensile fracture in rock. The basalt shows a rough fracture surface with resistant phenocrysts (Figure 24a) versus the reduced surface-roughness produced by abrasion with gravel (Figure 24b). Figure 24b shows concentrated erosion on similar olivine phenocrysts. The rough fractured granite surface, Figure 24c, shows conchoidal, cleavage and parting surfaces on individual minerals, contrasted with very little surface roughness after abrasion with sediment in Figure 24d. Saltation-abrasion utilizes voids and preexisting fractures, increasing the erodible surface area. Indurating-cement, fine-grained crystalline groundmasses, and mineral interlocking reduce porosity. Saltation-abrasion erosion is shown to be on a fundamentally smaller length-scale than that which the Brazilian strength test directly measures, eroding mass with less energy per impact compared to that required to propagate tensile failures along grain boundaries and through minerals.

2.6 Discussion

2.6.1 Main Findings

Relative bedrock resistance to erosion shows a strong power-law scaling relationship with tensile strength, grain size, and density. Fracture mechanics theory and results from previous studies by Knudsen (1958) support this result. The SEM work presented here exposes a fundamental difference in length scale between the mineral-scale tensile fracturing (e.g. mm-cm) of the Brazilian tensile strength tests and the micrometer-scale texture and roughness relief resulting from abrasion with sediment and silt-production (Figures 23 and 24).

Despite the expectations developed from fracture mechanics theory, elasticity does not explain any of the variability in tensile strength for a given erosion rate. Results from multivariate regression modeling of erodibility show that the combination of tensile strength, grain size, and dry bulk density reduces the variability in erosion rate (R^2 increases from 0.47 to 0.69) and increases the predictability (95% confidence interval reduces from 2.31 to 1.81 orders of magnitude on logarithmic scale) of the relative erodibility model.

These data show that porosity is not a significant explanatory variable for bedrock erosion rates, but density does explain some of the variability (~2%) about the power-law fit of erosion rate versus tensile strength. This could be because the range in porosity values is limited with sparse data, while the density data incorporate porosity and vary over a more representative lithologic range. I performed an analysis of which grain size

statistic (D10, D50, D90) adds the most information to the erodibility model and the 10th quantile, D10, proved to be the most robust (see Appendix 1). My regression parameter estimates of 1.8, .47, and 5.7 (from Equation 14) are within the margin of error of expected values of 2, ½, and 5 respectively. Furthermore these parameter values are supported by fracture mechanics and toughness theory and are consistent with results from Knudsen (1958) regarding the strength of synthetic polycrystalline brittle materials.

2.6.2 Implications and Predictability

The combination of tensile strength, grain size, and density yield a predictive model (R^2 of 0.69) for relative bedrock resistance to erosion. However tensile strength is relatively hard to measure and the strong covariation with elasticity suggests that other rock property measurements (e.g. Schmidt hammer, indentation hardness) may be combined in a similar manner to predict relative erodibilities.

2.6.3 Limitations

This work aims to dig deeper into the relationship between erodibility and strength, specifically using other rock properties such as elasticity, grain size, density and porosity. Bedrock erosion experiments done by Sklar and Dietrich (2001) provide an interesting method for experimentally modeling the fluvial abrasion of bedrock with gravel sediment. However the BAM experiments cannot fully represent natural

conditions due to the complications from factors such as time and weathering. The strength measurements assume that quasi-static compression-induced tensile failures represent mass-removal by rivers, but other mechanisms are likely to be influential. The porosity measurements presented here are truly effective porosities and likely to have uncertainty due to the lack of natural conditions, a pervasive theme in laboratory experiments. Therefore the insights from bedrock experiments on erosion, presented here, actually discuss the relative erodibility of rocks opposed to an absolute and quantifiable erodibility.

2.6.4 Next Steps

These experiments shed new insight on the relative erodibility of bedrock substrate, however it is still unclear of how to relate these laboratory findings to field applications. Work could be done to shed light on this lab-to-field scaling in order to estimate, predict, and compare erodibilities in the field.

SEM is emerging as a tool for investigating surface textures on various materials (*e.g.*, Russ and Russ, 1987; Banerjee *et al.*, 2009) and resulting from different processes, specifically rock abrasion by sediment shown by this work. More work could be done to investigate and quantify process-based textures. Further studies could investigate the aforementioned scale-mismatch between silt-production from bedrock abrasion by sediment and how tensile fractures propagate through bedrock.

3. Sediment Abrasion

Tectonics, climate, and bedrock material properties are fundamental drivers that influence the evolution of mountain topography. As rain falls on a landscape, a multitude of hillslope and debris flow processes produce mobile material from bedrock (i.e., sediment) and deliver it to the channel network (e.g., *Dietrich et al., 2003; Stock and Dietrich, 2003*) where fluvial processes take over and bounce and roll (saltate) material downstream (*Sklar and Dietrich, 2001*). Figure 1 shows a sediment source-to-sink schematic. In recent years, tumbler and flume experiments have been used to explore the mechanics behind the attack that rivers wage on rocks (e.g., *Kodama, 1994; Lewin and Brewer, 2002; Attal and Lavé, 2009*). Rivers are primary drivers of landscape evolution by first incising into bedrock, effectively lowering valley bottoms, steepening channels and hillslopes, and creating gravitational instabilities that lead to landslides (e.g., *Dietrich et al., 2003; Stock and Dietrich, 2003; Attal and Lavé, 2009*). And second, rivers transport all the mobile sediment downstream as dissolved load, suspended load, and bedload (*Sklar et al., 2006*). Sediment reduces in size (downstream fining) while saltating downstream. Sediment particles collide with bedrock and other clasts as they travel from headwater tributaries and upland regions—where there is little storage of sediment—to depositional fans and sedimentary basins; these processes have been modeled by many as the effects of diminution, splitting and breaking, comminution, and attrition (e.g., *Kodama, 1994; Lewin and Brewer, 2002; Attal and Lavé, 2009*). Recent

work (*e.g.*, Sklar *et al.*, 2006; Lewin and Brewer, 2002; Attal and Lavé, 2009) shows there is active debate over the mechanisms of abrasion, and this study aims to interrogate abraded rocks with SEM, at a scale not previously used to explore downstream fining in rivers. I also use SEM to help develop scale-based methods for investigating how bedload evolves in a river, how rivers abrade rock, and how bedload resists erosion with downstream transport. This work aims to offer a new scale-based perspective to understanding rock strength limitations and the interpretation of topographic gradients in actively uplifting terrain.

3.1.1 Downstream Fining of River Sediment

The downstream fining of sediment in gravel-bedded rivers (those that transport grains larger than sand) is a widely recognized and unexplained phenomenon. It is often described by tradeoffs between downstream transport limitations (*i.e.*, selective transport of finer grains in bigger sluggish channels) and pulverizing of sediment with distance travelled downstream (*e.g.*, Ferguson *et al.*, 1996; Sklar *et al.*, 2006; Attal and Lavé, 2009); shown schematically in Figure 25. Selective transport has been shown to cause rapid downstream fining over short distances in alluviated valleys, nested within upland regions (Ferguson *et al.*, 1996) but on geologic timescales sorting explains transient states of aggradation (*i.e.*, woody debris, log jams, debris-flow dams, manmade dams, glacial pulses, local base-level changes) (*e.g.*, Montgomery *et al.*, 2003). Even at the

scale of small drainage basins (10–100 km²), abrasion and splitting processes arguably control the efficiency of downstream fining in rivers, particularly for intermediate rock strengths (*Sklar et al., 2006*).

Sklar et al. (2006) found that rock durability is the dominant factor in the abrasional efficiency of rivers and furthermore sets the abrasion length scale of bed material evolution (i.e., downstream distance at which sediment reduces in size to suspended load). This is supported by results from studies by Abbott and Peterson (1978) and Attal and Lavé (2009), showing that the erodibility of rock varies over orders of magnitude by lithology. Sediment abrasion is parameterized as wear per distance in Sternberg's Law,

$$D = D_0 e^{-\alpha x} \quad (12)$$

where particles wear down from an initial size D_0 to D over a distance of x , at a rate scaled by α (1/m). Despite decades of research (e.g., *Kodama, 1994; Sklar and Dietrich, 2001; Sklar et al., 2006; Attal and Lavé, 2009*) and attempts to simulate high-energy flood conditions (*Kodama, 1994*) no quantitative model exists to simulate natural conditions and α remains somewhat of a black-box term with mostly unmeasured influences.

The dependence of abrasion on rock durability is akin to the relation found by Sklar and Dietrich (2001) where bedrock resistance to fluvial abrasion scales with rock tensile strength (i.e., $E_{rate} \approx \sigma_t^2$). At the laboratory scale, bedrock resistance to wear by

saltating bedload is strongly coupled to tensile strength (Figure 10) although order-of-magnitude variability, particularly among stronger rock types, limits the applicability of this finding to the field (*Sklar and Dietrich, 2001*). Insights from bedrock erodibility suggest that coupling this strength relation with grain size and porosity or density may yield a highly predictive 4-parameter model for sediment abrasion rates.

3.1.2 Modeling Sediment Abrasion with Rock Properties

Following theory and results for modeling relative bedrock erodibility one could expect sediment “abradability” to follow similar dependencies on rock properties such as tensile strength, grain size, and density or porosity. It is reasonable to believe that abrasion rates scale in the same manner with tensile strength, σ_t , in the expression:

$$\alpha_{rate} = f(\sigma_t)^2 \quad (13)$$

Brittle failure in sediment is described as comminution and should depend on bulk strength properties as well as on the elastic rock properties. However the inclusion of Young’s modulus of elasticity, Y , does not help explain erodibility and therefore is abandoned here. Following fracture toughness theory, grain size and porosity set the scale of inherent weaknesses in a rock mass which are exploited by brittle failure (*Brace, 1961*). Incorporating the square of grain size, D , yields the expression:

$$\alpha_r = f(\sigma_t^2 D^{1/2}) \quad (14)$$

Incorporating Knudsen's (1958) exponential relationship between strength and porosity yields this form of the abrasion function:

$$\alpha_r = f(\sigma_i^2 (D^{1/2}) e^n) \quad (15)$$

However insight from modeling bedrock erodibility suggests including rock density, ρ , instead of porosity, as:

$$\alpha_r = f(\sigma_i^2 (D^{1/2}) e^\rho) \quad (16)$$

3.2 Methods

3.2.1 Measuring Rock Properties

Material rock properties of the rock types were measured using the same methods outlined previously to measure: tensile strength, elasticity, mineral grain size, density, and porosity; shown in Table 3. Figure 26 shows photomicrographs for all rocks in the sediment data set.

3.2.2 Barrel Tumbling Experiments

Tumbling experiments simulate comminution in a granular flow to investigate mass transfer from bedload to suspended load due to silt-production from abrasion in a barrel tumbler. Five rock types: granite, granodiorite, diorite, hornfels, and quartzite (Figure 27) were collected in the Sierra National Forest, CA for tumbling experiments

and measurements of rock properties. Rock samples included: boulders to core for strength and elasticity measurements, ~100g sediment grains for tumbling experiments, gravel samples for porosity measurements and thin section preparation to look at mineralogy and grain size. Roughly 1700g (17 x ~100g rocks of a single rock type) were placed in a barrel tumbler, filled with water, and tumbled at ~14 rpm for increments of 3.5–15 hours (converted to distances of ~1–18 km). Figure 28 shows the barrel and tumbler setup. I sieved everything in the barrel to measure comminution of individual grains bouncing and grinding in a granular flow (schematic shown in Figure 29) and measured the mass (in grams) of each grain larger than 1mm (i.e. larger than the sand fraction, thought to move as washload). I sampled (i.e., replaced one tumbled rock with a fresh quarry sample of comparable size and weight) at each weighing to investigate the evolution of the surface texture of the gravel due to mass loss (Figure 30).

3.2.3 SEM to Investigate Surface Wear

SEM is an emerging tool for understanding process-based textures, such as the submicron-scale smoothing of rock due to silt-production by abrasion (*e.g.*, *Lindé and Mycielska-Dowgiałło, 1980; Van Hoesen and Orndorff, 2004; Kasper-Zubillaga and Faustinos-Morales, 2007*). I am using SEM to quantify the extent of rock surface modification by silt-producing abrasion from transport in granular flows, simulated through barrel tumbler experiments at the UCB RFS. Rock specimen were cut from the

edge of tumbling samples and mounted to standard 1" aluminum SEM stubs with colloidal silver paint (Figure 16c). Mounted specimen were coated with a ~15nm layer of evaporated carbon to ground the rock surface to the metal stub. Using the Carl Zeiss Ultra 55 FE-SEM, rock surfaces were investigated and imaged with Everhart-Thornley detector at accelerating voltages of 12 KeV and typical working distances of 7-10 cm (see Figure 30 for SE2 images for each rock type). Anaglyphs were created with the Carl Zeiss FE-SEM software from image stereo pairs (i.e., images of the same field of view compiled by imaging the rock surface and then tilting it 7° and refocusing, to acquire a second image of the same surface). Figure 31 shows two stereo pairs and accompanying anaglyphs.

3.3 Results

3.3.1 Tumbling Experiments

Five rock types from the Sierra Nevada, CA, were used in barrel tumbling experiments to explore variations in sediment abrasion rates across gradients in rock strength and microtextures (shown in Table 3 and Figure 27). Plotting the total mass (in the barrel) versus the total distance (converted from tumbling duration and speed) allows for the calculation of an abrasion rate (i.e., the exponent on each best-fit curve in Figure 32). Figure 33 shows a general reduction in abrasion rate as the tumbling experiments

progress, evidencing that as the individual sediment grains reduced in size, the accompanying mass-reducing collisions were less energetic as well. The abrasion rates calculated from Figure 32 were combined with preexisting data from previous student theses the full sediment data set in Figure 34, showing a strong power-law relationship between measured abrasion coefficient, α_r , and tensile strength, σ_t .

3.3.2 Modeling Results

In this section I present the results from multi-variate regression modeling of the sediment abrasion rates measured from barrel tumbling experiments. Table 3 displays the measured rock properties for the bedrock experiments. Figure 26 shows the photomicrographs and hints at the systematic influence of grain size and porosity by rock type. Similar to the bedrock data set and results, mineral grain size is expected to be influential in explaining variance among the non-porous rocks (e.g., unweathered igneous and many metamorphic rocks), whereas porosity might prove to be influential among the porous (e.g., sedimentary) rock types expected to have a combined effect on the spectrum of rocks in the data set. Figure 35 shows cumulative mineral size distributions for the sediment data set, showing variation over 2 orders of magnitude.

Following the model expectations and results for relative erodibility laid out in the previous chapter, I tabulated the results of models based on strength alone (*Eq. 13*), fracture toughness (*Eq. 14*), fracture toughness with Knudsen's porosity relation (*Eq. 15*),

and fracture toughness with density (*Eq. 16*). The metrics that I used to evaluate the models are the explanation of variance (R^2 value), significance (%), and the prediction interval (integer in logarithmic scale), shown in Table 4 for the various models mentioned above. The inclusion of elasticity in a relationship like strain energy does not explain any of the variance in erosion rate for a given tensile strength; in fact it adds variance to the models, similar to the bedrock modeling results (see Appendix 2 for statistical analysis of individual model outputs). Grain size proves to be influential, explaining roughly a third of the remaining variance in α , following *Eq. 14*. The addition of density in *Eq. 15* surprisingly does not explain any of the additional variance in abrasion data. The parameter estimates for density yield it insignificant at roughly the 97% level (<3% significance). The inclusion of porosity is also not highly significant, but significant to ~80% level. This is encouraging because the parameter estimates for an abrasion model of the form in *Eq. 15* yield exponent estimates of roughly:

$$\alpha_r = f(\sigma_t^{3/2} (D^{1/2}) e^{6\rho}) \quad (17)$$

This result is consistent with fracture mechanics theory and is similar to results from Knudsen (1958) yielding a parameter estimate for grain size of roughly $\frac{1}{2}$, and 6 for porosity, within the margin of error on my parameter estimates. Despite the parameter estimates and variance explained, the inclusion of porosity renders all of the variables in the model not highly significant so this form of the model is abandoned. The most

statistically robust model for sediment abrasion (Figure 36) supported by the data presented here is:

$$a_r = f(\sigma_t^{3/2} D^{1/2}) \quad (18)$$

It is reasonable to believe that the exponent on tensile strength should be close to 2, but not necessarily precisely 2. This will be described further in the discussion section. See Table 4 for sediment abrasion model metric results.

3.3.3 Insight from SEM Anaglyphs

SEM was used to investigate the process of mass transfer, through granular-flow tumbling, from the gravel sediment to fine sediment. Figure 30 shows SEM image series for the three Providence Creek rocks (diorite, granodiorite, and granite) comparing relatively untumbled surfaces with intermediate tumbling, and the final tumbled surface after concluding the experiments. The first column displays the least tumbled diorite, granite, and granodiorite in ascending order corresponding to coarsening grain size. The second and third columns of images show the same rocks after progressively longer barrel tumbling. Each row of images (i.e., rock type) shows high roughness relief to the left, at the mineral grain scale, and a reduction in roughness relief to the right as the tumbling experiments progressed. The resultant textures in the third column display the same roughness relief; that which is at the scale of mass removal through tumbling abrasion. The silt particles noted in many of the images are evidence that mass removal

through abrasion happens as silt production, also evidenced by the lack of sand production throughout the experiments, noted previously (Section 3.3.1).

Figure 37 displays a series of anaglyphs for each rock type discussed in Figure 30. They nicely show the reduction of roughness relief through silt-production from tumbling abrasion. Mineral grain size sets the roughness relief of the fractured surfaces on the rocks supplied fresh from a hillslope outcrop, while silt-production takes over during tumbling and eventually erases much of the previous mineral texture. This is evidenced by comparing the untumbled and tumbled surfaces (top and bottom images) in Figure 37a, b, c.

3.4 Discussion

3.4.1 Main Findings

The covariation of tested rock properties for the sediment data set is shown in Figure 38. Tensile strength, elastic modulus, and porosity significantly covary with each other. Density only slightly covaries strength, elasticity, and porosity. Similar to the bedrock results, grain size does not significantly covary with any of the rock properties and is the only independent new information to couple with strength in an abrasion expression. Density shows less correlation with all of the other rock properties compared to porosity, again consistent with the bedrock data set results.

However contrary to the bedrock results, D90 shows to be more demonstrative in explaining variance in abrasion rates for a given measured tensile strength rather than D10. The reason for this difference could be rooted in the fact that two processes (saltation-abrasion and granular flow) are fundamentally different; saltation impacts in BAMs versus bouncing and sliding in the barrel tumbler. This may explain why the slope of the power-law relationship (Figure 34) between abrasion and tensile strength is $3/2$ and not 2, as with the bedrock data set.

Anaglyphs in Figure 37 show the texture of erosion through grain-grain impacts versus the mineral-scale roughness from fracturing through and around grains, similar to Mode-1 fracturing under tension shown in Section 2.5.2.

3.4.2 Implications and Predictability

As shown in Table 4, coupling strength and mineral grain size in an expression for sediment abrasion rates explains 83% of the model variance, with a prediction interval of 1.9. This work shows that grain size greatly increases the predictability of the observed and understudied relationship between abrasion rates and strength. I believe it shows that not only can we measure meaningful laboratory sediment abrasion rates, but also we can predict them (with a reasonable margin of error) with strength and grain size.

3.4.3 Limitations

Although downstream fining in rivers by fluvial processes was the motivation for this study and this work mainly studied granular-flow processes, the two processes are relatable. Akin to the bedrock study, this work models the relative abrasion of sediment due to the lack of natural conditions (e.g., time, weathering, true fluvial processes).

3.4.4 Next Steps

This work lends new understanding to sediment abrasion experiments, however it is an understanding inherently limited to the laboratory setting. Relationships have been recognized between field and laboratory estimates of abrasion, however no quantitative scaling yet exists between the two settings. If an ideal natural experiment presented itself with the appropriate field setting, a well directed field campaign could attempt to estimate field abrasion rates of particle breakdown by excluding resupply and selective transport to relate to preexisting or easily measured laboratory abrasion rates.

4. Laboratory to Field Scaling

4.1 Introduction

The downstream fining of river sediment is a widely discussed phenomenon, but understudied in terms of decoupling process and mechanism natural landscapes (*e.g.*, *Hack, 1957; Miller, 1958; Brush, 1961; Ferguson, 1994; Heller et al., 2001*). Theory and procedures are needed to estimate field rates of downstream fining and the influence of abrasion. It is possible to measure relative rock erodibility and rates of sediment abrasion in the laboratory, however until these are directly relatable to field estimates they remain “relative” quantities. In general field estimates of sediment abrasion and downstream fining are higher (by a factor roughly between 2–10) than lab estimates for the same rock types, and this is attributed to an issue with the inherent scale differences between laboratory experiments and the natural processes. This suggests the likelihood of a systematic scaling relationship between laboratory experiments and field estimated rates, however the nature of this proposed relationship is not well understood.

4.1.1 Bedrock Incision

Rivers set the pace of landscape evolution by first lowering valley bottoms through incision into bedrock and, second, by transporting all the mobile sediment

downstream, as mentioned previously in Chapter 2. Sediment supply and grain size affect rates of incision into bedrock as well as channel slope and fluvial relief because rivers need tools to erode their beds (*e.g. Sklar et al., 2006*). Mobile sediment moves downstream as bedload, suspended load, and dissolved load. Strong feedbacks exist between the bedrock topography supplying the sediment, the downstream resupply from hillslope processes, and particle breakdown due to collisions in transport; causing the grain size distributions of sediment in rivers to evolve downstream and consequently producing suspended sediment from bedload and bedrock (*Sklar et al., 2006*). It is widely observed that variations in the size of river sediments vary systematically with river network attributes such as channel geometry (slope, depth, width) and drainage area. Despite the wealth of previous field and laboratory studies of sediment size reduction, it remains difficult to scale from laboratory measurements of particle abrasion to predict rates of downstream size reduction in rivers. This study attempts to link fieldwork in the Sierra Nevada, CA, to the sediment abrasion experiments of the previous chapter.

4.1.2 Setting for a Natural Experiment

The ideal location for a natural experiment to study sediment abrasion in rivers would be a watershed with the following attributes: multiple different and identifiable rock types, a distinct upstream limit to the source area of the lithologies, no downstream

resupply of sediment from hillslopes or tributaries, long enough travel pathways within the watershed to allow for breakdown in transport, moderate topographic relief, no net deposition (aggradation in valley bottoms) within watershed, bedrock channels with little to no sediment cover and storage in alluvial deposits (e.g. fluvial terraces). The simplest version of a restricted upstream source is a lithologic contact, shown schematically in Figure 39.

4.1.3 Dinkey Creek Field Site

Dinkey Creek is a tributary to the North Fork of the Kings River in the Sierra National Forest in Fresno County, CA (Figure 6). Despite the name, Dinkey Creek is a sizable watershed (~85,000 km² drainage area) and the headwaters flow from alpine cirques through Sierran bedrock in the Dinkey Creek Wilderness down into the Pine Flats Reservoir just after joining the North Fork of the Kings River (*Gallegos, 2002*). The geology of the watershed tells a complex story; from the intrusion of the Sierran batholith up into the country rock (much of which was marine sediments which now make up the metasedimentary roof pendants, shown in Figure 40) to the uplift of the Sierra Nevada and the consequent fluvial and glacial erosion responsible for carving the modern peaks and canyons (see Figure 41 for generalized geologic map). The watershed has a deep land-use history over a much shorter time span; from centuries of Central Miwoks living in the Sierra Nevada prior to contact with the Spanish missionaries (evidenced by

bedrock mortars shown in Figure 42), to the gold mining after 1848 that scarred much of the landscape, to the modern day logging and dam building (*Barrett and Gifford, 1933; Gallegos, 2002*).

Most of the bedrock exposed in the watershed is Dinkey Creek granodiorite, however roof pendant rocks (e.g., quartzite, biotite hornfels, biotite schist, calc silicates) outcrop in the headwaters of Dinkey Creek and the Dinkey Creek Geological Area (Figure 43). The roof-pendants relatively overly the Sierran batholith and are mostly composed of metamorphosed marine sediments with varying degrees of alteration, resulting from contact and deformation from the intrusion of the batholith. Quartzite and hornfels are generally restricted to headwater outcrops and glacial deposits, however they also outcrop at high elevations along peaks and ridges that feed smaller tributaries (e.g., Deer, Laurel, and Bear Creeks shown in Figure 44).

4.1.4 Theory for Proposed Scaling Relationship

Recalling theory from the previous chapter, Sternberg's Law (1875) has been used for over a century to describe the reduction in grain size of sediment in rivers as:

$$D = D_0 e^{-\alpha x} \quad (12)$$

where the initial grain size, D_0 , evolves to, D , exponentially over some distance, x .

Results from sediment abrasion experiments of the previous chapter show that laboratory

abrasion rates can accurately be modeled by coupling tensile strength and grain size in the expression:

$$\alpha_{lab} = f(\sigma_t^{3/2} D^{1/2}) \quad (19)$$

As suggested above, field-estimated abrasion rates may generally be higher than those measured in the laboratory for the same rock types. This suggests a systematic scaling relationship, possibly of the form:

$$b = \alpha_{field} / \alpha_{lab} \quad (20)$$

where b is a scaling factor. Field sediment abrasion rates are very difficult to estimate, but laboratory experiments accurately measure relative abrasion rates (*Attal and Lavé, 2009*). By assuming that lab experiments can be done to measure a relative reference abrasion rate, α_{ref} , and by solving Equation 20 for α_{field} , the expression can be arranged to incorporate the scaling factor and reference abrasion rate as:

$$\alpha_{field} = b \alpha_{ref} \quad (21)$$

The scale of silt production and the previous sediment-abrasion modeling results suggest the form:

$$\alpha_{field} = b \sigma_t^a D^b \quad (22)$$

4.2 Methods to Estimate Abrasion in the Field

I went to Dinkey Creek in the Sierra National Forest, CA, (Figure 6 and 45) to estimate median grain size of two lithologies (quartzite and biotite hornfels) and to track

particle breakdown through travel downstream from a restricted bedrock source. The recognizable difference in relative durability justifies using quartzite and hornfels for this study; evidenced by different tensile strengths (Table 3 and 5b) and shown by results from Abbot and Peterson (1978) and from Attal and Lavé (2009) where schist and quartzite straddle the range of reported rock durability. By identifying the headwater outcrops and glacial moraines as the upstream source of quartzite and hornfels to Dinkey Creek, I went downstream to various points in the channel (Figure 45) to estimate the median grain size passing through that point in the watershed by doing pebble counts. The sourcing is mostly restricted by bedrock contacts, but the absolute upstream limit is restricted to eroding moraines in adjacent hillslopes.

Pebble count site selection was based on the extent of bedrock exposed in the channel, minimal degree of apparent local selective transport, and accessibility. The local hydraulics at sites must be comparable to avoid variations based on facies or different local channel geometry. Channel geometry was held constant by selecting relatively straight reaches, avoiding sinuous reaches, bends, pools, and gravel bars. Once I selected a reach, I stretched a tape across the active part of the channel, as shown in Figure 46. Pebble counts have been done for decades with the goal of quantitatively characterizing the sediment at a given location, through unbiased random sampling (e.g., random walks, zigzagging, blind selection, walking a tape with specific sampling intervals, etc.). The pebble counting method employed here characterized the sediment

in Dinkey Creek in a relatively unorthodox manner. I walked the width of the channel and measured the intermediate axis of every hornfels and quartzite clast that lay on the surface of the channel bed below the tape, within a 10 cm window (approximated by the width of my fist). The grain size data were tabulated to investigate breakdown in the channel and identify resupply from hillslopes and tributaries, shown in Table 5.

4.3 Results

4.3.1 Pebble Counts in Dinkey Creek

A downstream limit to the hillslope sourcing of quartzite and hornfels was determined in the field and pebble counts were done progressively downstream (Figure 45) to characterize the size of the sediment moving through that given point in the channel network (Table 5). Reach-specific abrasion rates (calculated reach alpha) were calculated by measuring the distance between sites and comparing the change in median grain size of each lithology over that distance (% change/km), shown in Table 5a. Negligible resupply was observed between sites 5 and 6 (Figure 45) despite the large addition of drainage area and discharge from the inputs by Laurel and Bear Creek tributaries (Figure 44) and therefore respective reach-specific abrasion rates (i.e. $\alpha_{DCQ} = 0.026$, $\alpha_{DSH} = 0.173$) represent grain size reduction through particle breakdown with transport.

4.4 Discussion

4.4.1 Main Findings

Analyzing the calculated reach alphas in Table 5a allows for many interpretations of downstream fining. Any negative reach alphas are strong indications of hillslope or tributary resupply of coarser sediment (intuitively sediment grain sizes should not increase from downstream transport unless more sediment is added) to the mainstem channel of Dinkey Creek, between sampling sites. Very large reach alpha values can be interpreted as selective transport of finer material, leaving behind the coarser material. By interpreting that there is little if any resupply of hornfels or quartzite between sites 5 and 6, it is reasonable to believe that the calculated reach alphas represent breakdown through transport. The similarity in calculated alpha between the two final sites ($\alpha_{\text{quartzite}} \approx 0.0589$ and $\alpha_{\text{hornfels}} \approx 0.0547$), regardless of the strength differences among the rock types, is highly suggestive of selective transport conditions.

4.4.2 Lab to Field Scaling

By assuming that the calculated reach alphas (α_{field}) between sites 5 and 6 for hornfels and quartzite accurately represent downstream fining due to particle breakdown in Dinkey Creek, CA, (Figure 45) then these field estimates can be compared with the

barrel-tumbling abrasion rates (α_{lab}) for an investigation of the previously proposed scaling relationship, Equation 20. Table 5b compares the data and corresponding scaling factor values, b , for both rock types. Intriguingly, the b values are similar to each other ($b_{quartzite} = 6.5$ and $b_{hornfels} = 7.5$). This suggests an average scaling factor of $b = 7$ for this experimental setup (discussed in Chapter 3).

4.4.3 Experimental Limitations

Although the results from this study are not conclusive, they highlight the potential to connect laboratory experiments with a directed field study of the fluvial breakdown of sediment. This study was limited by the availability of field sites and attainable data. If multiple field sites could be coupled into the study, or more rock types for a more robust data set of field abrasion rates, then hopefully more conclusive results could be drawn about the proposed lab-to-field scaling of sediment abrasion rates.

4.4.4 Future Research Needs

Few studies with sparse data exist discussing field estimates of sediment abrasion and downstream fining of variable lithologies. I believe more studies of this sort would be a worthy endeavor to help understand the processes of downstream fining with transport and how sediment grain size distributions evolve in rivers. This work partially answers the questions that I asked at the beginning (Section 1.3), however they have also

lead to new ones. How can we scale from lab-to-field for estimates of particle breakdown in rivers? What can be measured to understand how far sediment has travelled downstream? Can SEM work quantify the degree of surface texture modification from abrasion?

5. Lab to Field Synthesis

5.1 Summary and Conclusions

Rivers drive landscape evolution through bedrock incision and sediment removal from watersheds. Strong feedbacks exist between rivers, the sediment in rivers, the neighboring hillslopes and the bedrock landscape. Rivers lower valley bottoms by using sediment as tools, and they create gravitational instabilities that lead to mass wasting processes (e.g., mudflows, landslides, rockfalls) that deliver more sediment to river valleys. The efficacy of river incision depends on the available sediment and water discharge, but primarily on the erodibility of the rock substrate.

Bedrock erodibility has been shown experimentally to vary strongly with the square of tensile strength (*Sklar and Dietrich, 2001*). Similarly, experimentally measured sediment abrasion rates (presented in Chapter 3) also depend on strength and vary by rock type (*Attal and Lavé, 2009; Abbot and Peterson, 1978*). Despite decades of research on the downstream fining of river sediments, little is known about the influence of breakdown in the field (*e.g., Hack, 1957; Miller, 1958; Brush, 1961; Ferguson, 1994; Heller et al., 2001*). Modeling of river network dynamics shows that breakdown in the field should have a strong influence on the evolution of grain size distributions between tributary junctions, particularly for intermediate rock strengths (*Sklar et al., 2006*).

This work comprises three studies investigating rock erodibility. The first is a reanalysis of the material properties of the rocks used in previous bedrock erosion experiments by Sklar and Dietrich (2001). Coupling tensile strength, mineral grain size, and density in a power function (Equation 11) forms a predictive expression for the relative erodibility of bedrock (Figure 21). SEM work exposes a length-scale mismatch between the erosion of rock by fluvial abrasion with sediment and fracturing rock through tension with quasi-static compression (Figures 23 and 24). Bedrock erosion from sediment impacts is shown to be at the sub-mineral-grain scale suggesting that fluvial abrasion for many rock types largely produces silt and fine material (Chapter 2).

The second study consists of sediment abrasion experiments. Abrasion rates were measured using a barrel tumbler (Figure 28), to investigate size reduction from grain-on-grain interactions in a granular flow, by rock type. Results from multivariate regression modeling show that coupling tensile strength and grain size (Equation 19) accurately predicts the relative “abradability” of sediment (Figure 36). I used SEM imagery to investigate the evolution of the surface texture of the tumbled sediment for three lithologies from Dinkey Creek, CA (Figures 30, and 31). Anaglyphs of the sediment textures (Figure 37) show that mass removal through tumbling (to represent downstream transport) happens as silt-production, erosion producing fine-grained material, at a length scale smaller than the mineral grains in most rocks (see Chapter 3).

The final study presented here is a field campaign to estimate rates of abrasion of two lithologies in Dinkey Creek in the Sierra National Forest, CA (Figure 6) to investigate a proposed scaling relationship between laboratory and field abrasion rates (Equation 20). Bedrock outcrops and glacial deposits were identified as the upstream source of quartzite and biotite hornfels to the mainstem channel (Figure 44). I performed pebble counts at 8 sites downstream of the sourcing limit to characterize the median grain size of the sediment, of both lithologies, moving through a given point in the watershed (Figure 45). Pebble count results were compared to the measured tensile strengths to identify potential breakdown as well as size-selective transport and resupply. Abrasion rates were calculated for both lithologies by measuring the decrease in grain size over the travel distance between sites (Table 5). From Equation 20, I calculated a scaling factor ($b = 7$) specific to the tumbling setup used in these experiments. Coupling this scaling factor with results from modeling sediment abrasion rates yields an expression for field estimates of abrasion (see Equation 22 in Chapter 4). These are not conclusive results yet they shed light on the understudied process of downstream fining in rivers due to sediment breakdown and highlight new methods to estimate field rates of sediment abrasion.

5.2 Future Research Needs

SEM is an emerging tool for studying process-based rock textures (i.e., smoothing from abrasion versus grain-by-grain roughness from fracturing) but more work could be done to quantify and compare surface textures, specifically roughness relief. This work elucidates downstream fining in rivers through particle breakdown, but it is still unknown how to definitely understand how far downstream sediment at a given point in a stream network has travelled.

6. References

- Allen, P. A. (2008), From landscapes into geological history. *Nature*, 451(7176), 274-276.
- ASTM Standard C215 (2008), "Standard Test Method for Fundamental Transverse, Longitudinal, and Torsional Resonant Frequencies of Concrete Specimens," ASTM International, West Conshohocken, PA, 2008, DOI: 10.1520/C0215-08, www.astm.org.
- Attal, M., and J. Lavé (2009), Pebble abrasion during fluvial transport: Experimental results and implications for the evolution of the sediment load along rivers, *J. Geophys. Res.*, 114, F04023, doi:10.1029/2009JF001328.
- Banerjee, S., R. Yang, and C. E. Courchene, (2009), Scanning Electron Microscopy Measurements of Surface Roughness of Paper. *Ind. Eng. Chem. Res.*, 48(09), doi: 10.1021/ie900029v.
- Barrett, S. A., & Gifford, E. W. (2006). *Miwok material culture*. Kessinger Publishing.
- Beaumont, C., Fulsack, P., Hamilton, J. (Eds.), 1992. *Erosional Control of Active Compressional Orogens. Thrust Tectonics*. Chapman and Hall, New York. 1–18 pp.
- Beyeler, J. D. (2010), The dependence of bedrock erodibility on rock material properties: is tensile strength enough? Bachelor thesis submitted to the SF State Dept. of Geosc.
- Brush, L.M. (1961), *Drainage Basins, Channels, and Flow Characteristics of Selected Streams in Central Pennsylvania*, USGS Prof. Paper 282-F, 175 pp., U.S. Gov. Print. Off., Washington, D.C.
- Dietrich, W. E., D. Bellugi, L. S. Sklar, J. D. Stock, A. M. Heimsath, and J. J. Roering (2003), Geomorphic transport laws for predicting landscape form and dynamics, in *Prediction in Geomorphology*, *Geophys. Monogr. Ser.*, vol. 135, edited by P. Wilcock and R. Iverson, pp. 103-132, AGU, Washington, D. C.
- Engle, P. A. (1978), *Impact Wear of Materials*, Elsevier Sci., New York.
- Ferguson, R. I., T. Hoey, S. Wathen, and A. Werritty (1996), Field evidence for rapid downstream fining of river gravels through selective transport, *Geology*, 24, 179-182
- Howard, A.D., Dietrich, W.E., Seidl, M.A., 1994. Modeling fluvial erosion on regional to continental scales. *Journal of Geophysical Research-Solid Earth* 13971–13986.
- Gilbert, G.K., (1877), *Report of the Geology of the Henry Mountains*, Geographical and Geological Survey of the Rocky Mountain Region, Government Printing Office: Washington, DC.
- Gomez, V., B. J. Rosser, D. H. Peacock, D. M. Hicks, and J. A. Palmer (2001), Downstream fining in a rapidly aggrading gravel bed river, *Water Resources Research*, 37, p. 1813-1823.
- Grady, D.E. and M. E. Kipp (1987), *Fracture mechanics of rock*: London, Academic Press Inc., p. 444.

- Hack, J. T. (1957) Studies of longitudinal stream profiles in Virginia and Maryland, USGSPP 294-B.
- Hack, J. T. (1975). Dynamic equilibrium and landscape evolution. Theories of landform Evolution (Melhorn, WN; Flemal, RC; editors). Alien and Unwin, 87-102.
- Heggnes, J. (1988). Physical habitat selection by brown trout (*Salmo trutta*) in riverine systems. *Nordic Journal of Freshwater Research*, (64).
- Heller, P. L., Beland, P. E., Humphrey, N. F., Konrad, S. K., Lynds, R. M., McMillan, M. E., and Furbish, D. J. (2001). Paradox of downstream fining and weathering-rind formation in the lower Hoh River, Olympic Peninsula, Washington. *Geology*, 29(11), 971-974.
- Hsu, L., W. E. Dietrich, and L. S. Sklar (2008), Experimental study of bedrock erosion by granular flows, *J. Geophys. Res.*, 113, F02001, doi:10.1029/2007JF000778.
- Kasper-Zubillaga, J. J. and R. Faustinos-Morales (2007), Scanning electron microscopy analysis of quartz grains in desert and coastal dune sands, Altar Desert, NW Mexico. *Ciencias Marinas*, 33(1), p. 11-22.
- Kodama, Y. (1994), Experimental study of abrasion and its role in producing downstream fining in gravel-bed rivers, *J. Sediment Res., Sect. A*, 64, 76-85.
- Kumano, A., & Goldsmith, W. (1982). An analytical and experimental investigation of the effect of impact on coarse granular rocks. *Rock Mechanics and Rock Engineering*, 15(2), 67-97.
- Lewin, J., and P. A. Brewer (2002), Laboratory simulation of clast abrasion, *Earth surf. Processes Landforms*, 27, 145-164
- Lindé, K. and E. Mycielska-Dowgiało (1980), Some experimentally produced microtextures on grain surfaces of quartz sand, *Geogr. Ann.*, 62 A (3-4), p. 171-184.
- Litwin, K. L. (2010), Influence of Ice Composition on Tensile Strength and Erosion Rates on Titan, Master's thesis, San Francisco State University.
- Miller, J. P. (1958). High Mountain Streams: Effects of Geology on Channel Characteristics and Bed Material. Interpretation of Quantitative Measurements Made in the Sangre de Cristo Range, North-central New Mexico. State Bureau of Mines and Mineral Resources, New Mexico Institute of Mining and Technology.
- Merriam, R., H. H. Rieke, and Y. C. Kim (1970), Tensile strength related to mineralogy and texture of some granitic rocks, *Eng. Geol.*, 4, p. 155-160.
- Montgomery, D. R., T. M. Massong, and S. C. S. Hawley (2003), Influence of debris flows and log jams on the locations of pools and alluvial channel reaches, Oregon Coast Range, *Geol. Soc. Am. Bull.*, 115, 78-88.
- Pizzuto, J. E. (1995). Downstream fining in a network of gravel-bedded rivers. *Water Resources Research*, 31(3), 753-759.
- Russ, J. C., & Russ, J. C. (1987). Feature-specific Measurement of Surface Roughness in SEM Images. *Particle & Particle Systems Characterization*, 4(1-4), 22-25.

- Schlunegger, F., Melzer, J., & Tucker, G. (2001). Climate, exposed source-rock lithologies, crustal uplift and surface erosion: a theoretical analysis calibrated with data from the Alps/North Alpine Foreland Basin system. *International Journal of Earth Sciences*, 90(3), 484-499.
- Sklar, L. S. and W. E. Dietrich (2001), Sediment and rock strength controls on river incision into bedrock, *Geology*, 29, No. 12, p. 1087-1090.
- Sklar, L. S. and W. E. Dietrich (2004), A mechanistic model for river incision into bedrock by saltating bedload, *Water Resources Research*, 40, W06301, doi:10.1029/2003WR002496.
- Sklar, L. S. and W. E. Dietrich (2006), The role of sediment in controlling bedrock channel slope: implications of the saltation–abrasion incision model, *Geomorphology*, 82, p. 58-83, doi: 10.1016/j.geomorph.2005.08.019.
- Sklar, L. S., W. E. Dietrich, E. Fofoula-Georgiou, B. Lashermes, and D. Bellugi (2006), Do gravel bed river size distributions record channel network structure?, *Water Resources Research*, 42, W06D18, doi:10.1029/2006WR005035.
- Stock, G. M., T. A. Ehlers, and K. A. Farley (2006), Where does sediment come from? Quantifying catchment erosion with detrital apatite (U-Th)/He thermochronometry, *Geology*, 34(9), 725–728, doi: 10.1130/G22592.1
- Stock, J. D., & D. R. Montgomery, (1999). Geologic constraints on bedrock river incision using the stream power law. *JOURNAL OF GEOPHYSICAL RESEARCH-ALL SERIES-*, 104, 4983-4994.
- Stock, J. D., and W. E. Dietrich (2003), Valley incision by debris flows: Evidence of a topographic signature, *Water Resour. Res.*, 39(4), 1089, doi:10.1029/2001WR001057.
- Stockli, D. F., K. A. Farley, and T. A. Dumitru (2000), Calibration of the apatite (U-Th)/He thermochronometer on an exhumed fault block, White Mountains, California, *Geology*, 28(11), p. 983– 986.
- Strand, R. G., (1967) *Geologic Atlas of California – Mariposa Sheet, California Geological Survey, Geologic Atlas of California Map No. 009, 1:250,000.*
- Tug̃rul, A. and I. H. Zarif (1999), Correlation of mineralogical and textural characteristics with engineering properties of selected granitic rocks from Turkey, *Eng. Geol.*, 51, p. 303-17.
- Van Hoesen, J. and R. Orndorff (2004), A comparative SEM study on the micromorphology of glacial and nonglacial clasts with varying age and lithology, *Can. J. Earth Sci.*, 41, p. 1123-1139, doi:10.1139/E04-056.
- Vasconcelos, G., P. B. Lourenço, C. A. S. Alves, and J. Pamplona (2008), Experimental characterization of the tensile behaviour of granites, *Int. J. Rock Mechanics & Mineral Sciences*, 45(22), p. 268–277.

- Vermeesch, P. (2007), Quantitative geomorphology of the White Mountains (California) using detrital apatite fission track thermochronology, *J. Geophys. Res.*, 112, F03004, doi:10.1029/2006JF000671.
- Vutukuri, V. S., R. D. Lama, and S. S. Saluja (1974), *Handbook on mechanical properties of rocks, Volume 1: Testing techniques and results*: Bay Village, Ohio, Trans Tech Publishers, p. 105-115.
- Ward, D. J., R. S. Anderson, and P. J. Haeussler (2012), Scaling the Teflon Peaks: Rock type and the generation of extreme relief in the glaciated western Alaska Range, *J. Geophys. Res.*, 117, F01031, doi:10.1029/2011JF002068.
- Whipple, K. X., & Tucker, G. E. (1999). Dynamics of the stream-power river incision model: Implications for height limits of mountain ranges, landscape response timescales, and research needs. *Journal of Geophysical Research*, 104(B8), 17661-17.
- Whipple, K.X., 2004. Bedrock rivers and the geomorphology of active orogens. *Annual Review of Earth and Planetary Sciences* 32, 151–185.
- Willett, S. D. (2010). Erosion on a line. *Tectonophysics*, 484(1), 168-180.

Table 1: Properties of rocks used in bedrock erosion analysis. All rocks were previously eroded and strength tested by *Sklar and Dietrich (2001)*.

Rock Type	Thin Section	Tensile Strength (Mpa)	E (g/hr)	Elastic Modulus (Mpa)	Porosity (%)	Density (kg/m ³)	D10 (m)	D50 (m)	D90 (m)
Basalt (Oz)	Z	11.6	0.16	74800	0.037	2.841	0.00004491	0.00009844	0.00037921
Utah Red Sandstone	UR	4.25	0.36	19000	0.102	2.27	0.00007188	0.00013866	0.00021805
Tyee Sandstone	TY	4.33	0.261	35000	0.027	2.58	0.0000172	0.00009178	0.0003056
Tachia Sandstone	TS	5.25	0.244	41000	0.032	2.64	0.00000781	0.00002479	0.00006577
Taroko Quartzite	TQ	9.45	0.074	58400	0.008	2.58	0.00006019	0.00015264	0.00037964
Taroko Marble	TM	5.41	0.63	53700	0.056	2.649	0.00010855	0.00028286	0.00046902
Taroko Schist	TA	5.31	0.13	23000	0.009	2.555	0.00000596	0.0000155	0.000057
Blonde Tuff	T	10.9	0.034	59100	0.034	2.475	0.00000582	0.00001163	0.00005817
Weak Sandstone	WS	1.583	2	17000	0.139	2.482	0.00002715	0.00010858	0.00030054
C' Sandstone (RED)	RS	4.48	0.042	27000	0.076	2.35	0.00006387	0.00010364	0.00022028
Red Marble	RM	9.75	0.264	53000	0.012	2.67	0.00001341	0.00003427	0.00026533
Quartzite	Q	18.95	0.0044	83900	0.049	2.535	0.00021352	0.00056977	0.00161515
Wafer' Sandstone (PINK)	PS	4.26	0.065	26800	0.217	2.365	0.00005673	0.00011863	0.00021782
Lichen Sandstone	LI	5.01	0.04	30600	0.216	2.17	0.00007367	0.00015204	0.00020385
Granite	GG	7.14	0.013	30600	0.018	2.633	0.00043517	0.00114672	0.00252023
Greenstone	G	23.8	0.04	94000	0.006	2.928	0.00000858	0.00002336	0.00021718
Eel Sandstone	E	6.65	0.19	37900	0.083	2.551	0.00006389	0.0001257	0.00026628
Andesite	A	24.4	0.044	79500	0.005	2.676	0.00000742	0.00004504	0.00025838
Wingate Sandstone	WSA	1.85	5	10700	0.156	2.369	0.00002715	0.00009501	0.00013573
Kayenta Sandstone	KSS	2.53	0.76	19600	0.099	2.399	0.0000446	0.00018033	0.00028309
Henry Mtns. Diorite	HMD	12.9	0.059	54700	0.051	2.51	0.00002526	0.00004547	0.00100028
Green Sandstone	GSS	12.1	0.033	22000	0.028	2.493	0.00007368	0.00013573	0.00020359
Limestone	LL	9.78	0.33	52020	0.008	.	0.0000067	0.00001344	0.00004209
Greywacke	HS	9.1	0.06	1060	0.056	.	0.00004875	0.0001525	0.00037434
Weathered Granite	WG	2.03	0.204		0.041	2.49	0.00052442	0.00092758	0.00144163
Green Marble	GM	16.7	0.186		0.011	2.64	0.00001218	0.00004529	0.00017636
Eel Mudstone	M	2.68	3.06		.	.	0.00000367	0.00000918	0.00002203

Table 2: Statistical metric results from modeling bedrock erosion with rock properties, following discussion in Section 2.5.2.

Model for explaining spread in E (power relations)	Variance Explained (r²)	Significance (p>F)	Prediction Interval range
Tensile Strength	0.47	<.0001	2.31
Strain Energy	0.37	0.0017	2.38
Fracture Toughness	0.42	0.0006	2.28
Knudsen Form of Eq	0.42	0.0006	2.28
Strength, grain size, & density	0.69	<.0001	1.81

Table 3: Properties of rocks used in tumbling experiments. All rocks (except the DCQ, DSH, PFG, PGD, and PSP) were previously tumbled and strength tested by Sklar and Dietrich (2001).

Rock Type	Thin Section	Alpha Tumbler (% loss/km)	Tensile Strength (MPa)	Elastic Mod (Mpa)	Porosity (%)	Density	D10 (m)	D50 (m)	D90 (m)
Navajo Sandstone	NS	4.1181	0.25	3680.0	0.210	2.3	6.2E-05	0.000139608	0.000215
Wingate Sandstone	WSA	6.73	1.850	10700.0	0.156	2.37	2.71E-05	0.000095011	0.000136
RC Serpentinite	RCS	0.0679	5.37	29900.0	0.117	2.477	9.7E-06	0.000023268	0.000512
RC Basalt	RCB	0.0567	11.79	38900.0	0.037	2.554	2.75E-06	0.000008262	1.93E-05
Prov. Ck Diorite	PSP	0.017	9.16	37560.0	0.018	2.915	0.000162	0.000368796	0.000793
Prov. Ck Granodiorite	PGD	0.013	7.67	28600.0	0.016	2.443	0.000374	0.000752748	0.001793
Prov. Ck Granite	PFG	0.006	5.85	34900.0	0.015	2.392	0.000273	0.000676968	0.001051
Ortega Quartzite	OQ	0.018	12.16	69070.0	0.006	2.541	0.000162	0.000348588	0.000546
Kayenta Sandstone	KSS	1.48	2.53	19600.0	0.099	2.399	4.46E-05	0.000180327	0.000283
Kayenta Sandstone	KSS	0.1048	2.53	19600.0	0.099	2.399	4.46E-05	0.000180327	0.000283
Henry Mtns. Diorite	HMD	0.0081	12.9	54700.0	0.051	2.51	2.53E-05	4.54671E-05	0.001
Entrada Sandstone	ESS	3.004	0.68	4100.0	0.191	2.399	1.55E-05	0.000067865	0.000136
Dinkey Ck Hornfels	DSH	0.023	12.69	81600.0	0.020	2.545	2.91E-05	0.000089194	0.000213
Dinky Ck Quartzite	DCQ	0.004	13.7049	40000.0	0.014	2.449	9.6E-05	0.000318276	0.001
Limestone	LL	0.0282	9.78	52020.0	0.008		6.7E-06	1.34408E-05	4.21E-05
RC Sandstone	RCG	0.0988	5.02		0.092	2.557	1.16E-05	0.000027146	7.76E-05

Table 4: Statistical metric results from modeling sediment abrasion with tensile strength and coupling strength with grain size.

Model for explaining spread in Alpha (power relations)	Variance Explained (r²)	Significance (p>F)	Prediction Interval range
Tensile Strength	0.75	<.0001	2.56
Strength and grain size	0.83	<.0001	1.9

Table 5: Pebble count data from Dinkey Creek, CA (a) negative reach alpha values indicate resupply. Scaling data (b) shows.

a.

Site #	Distance Downstream (km)	Quartzite D50 (mm)	Calculated Reach Q_Alpha	Hornfels D50 (mm)	Calculated Reach H_Alpha
1	0	46		54	
2	0.82539683	45	0.0773081	37	0.8218109
3	1.65079365	35	0.6415005	25.5	0.8149386
4	5.65079365	47.5	-0.3749089	29.5	-0.1370664
5	8.31746032	35	0.2249781	30	-0.0193928
6	11.4920635	34	0.0262359	23	0.1730517
7	17.9047619	40	-0.0979826	31	-0.2258812
8	29.6507937	27	0.0589521	22	0.0547058

b.

Rock	Tensile Strength (mPa)	Upstream St.5 D50 (mm)	Downstream St.6 D50 (mm)	Field Alpha (%/km)	Lab Alpha (%/km)	b
DC Quartzite	13.705	35	34	0.026	0.004	6.5
DC Hornfels	12.686	30	23	0.173	0.023	7.522

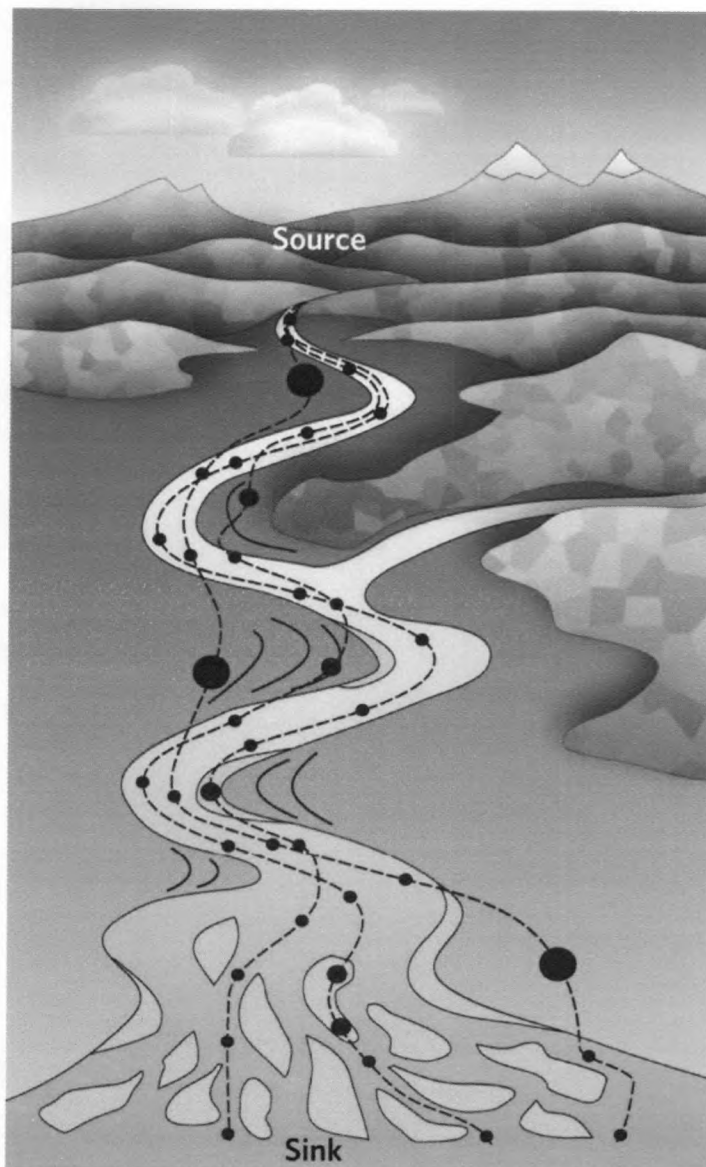


Figure 1: Source to sink schematic. Rivers transport water and sediment from upland regions to alluvial flood plains and basins, such as lakes and oceans. Larger dots represent more time spent at specific location, before experiencing further downstream transport. From Allen (2008).

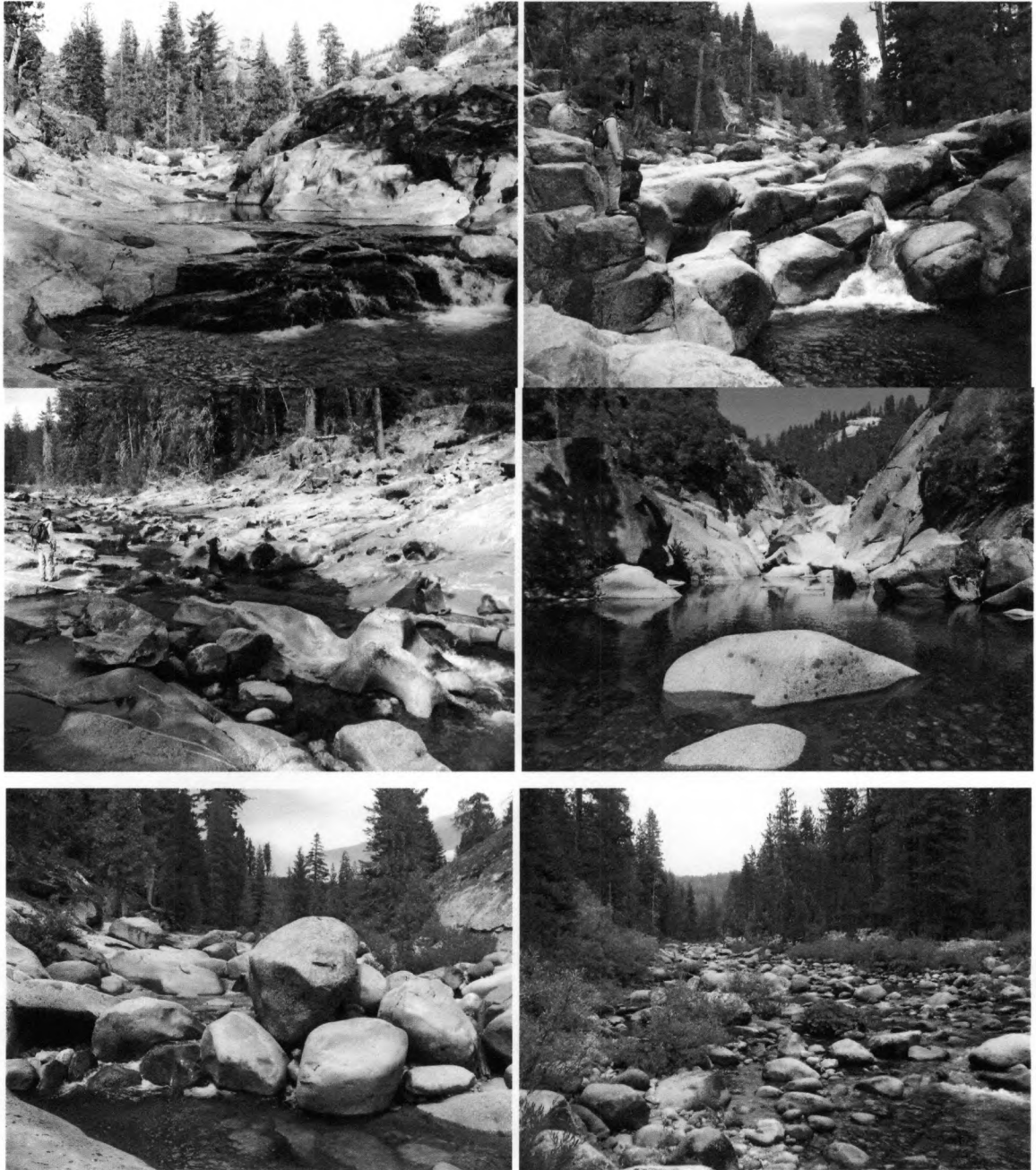


Figure 2: Pictures of Dinkey Creek, CA, an alpine river with sediment. Bedrock reaches alternate with boulder and alluvium reaches, stepwise downstream. Note the imbricated boulders and pothole scars in channel and along channel margins.



Figure 3: Tools for river incision. Sediments in rivers, like Dinkey Creek, CA, provide both tools to erode the bedrock and alluvial cover to protect it.

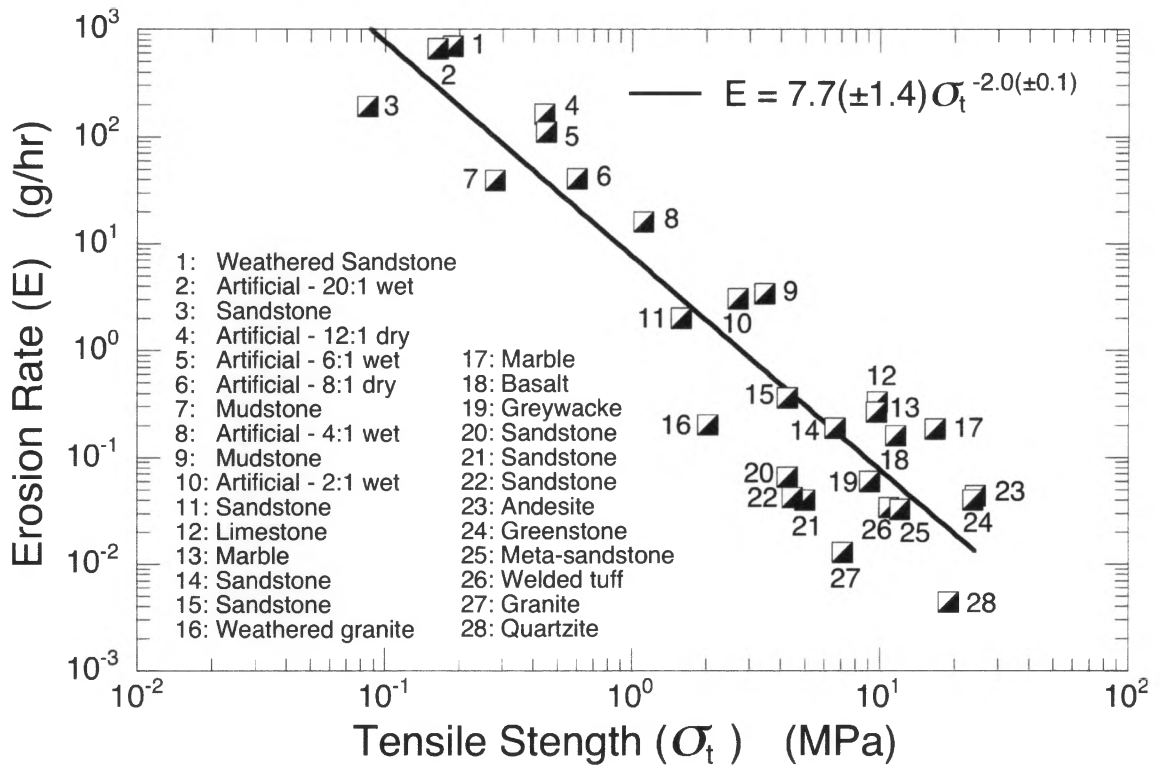


Figure 4: Log-log regression of erosion rate with tensile strength. From Sklar and Dietrich (2001).

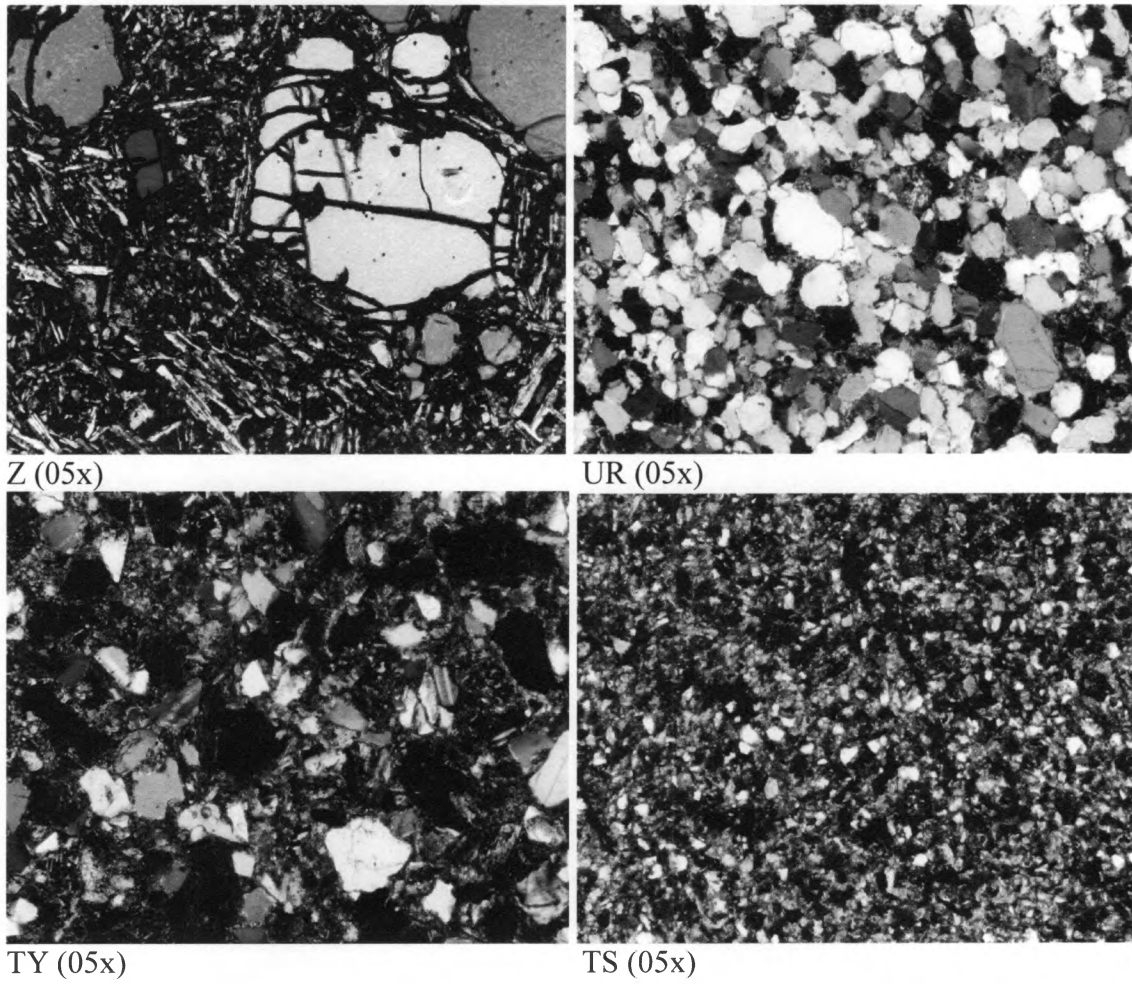
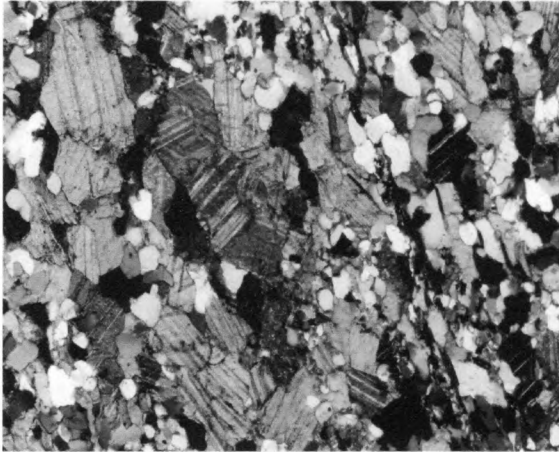
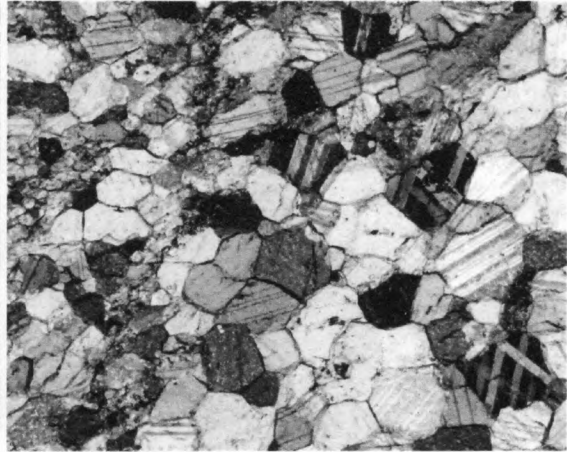


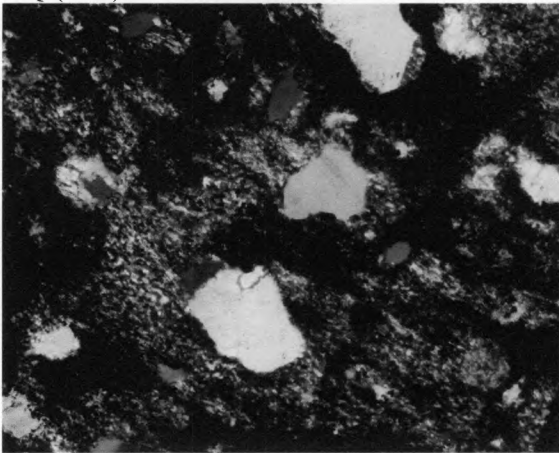
Figure 5: Photomicrographs from thin sections of rocks used in previous erosion experiments by *Sklar and Dietrich* (2001) in Table 1.



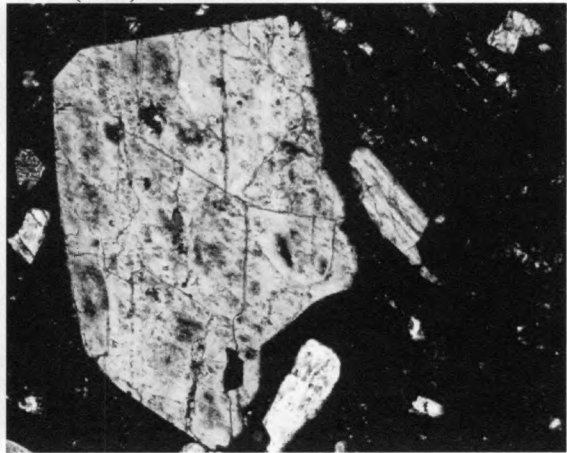
TQ (05x)



TM (05x)



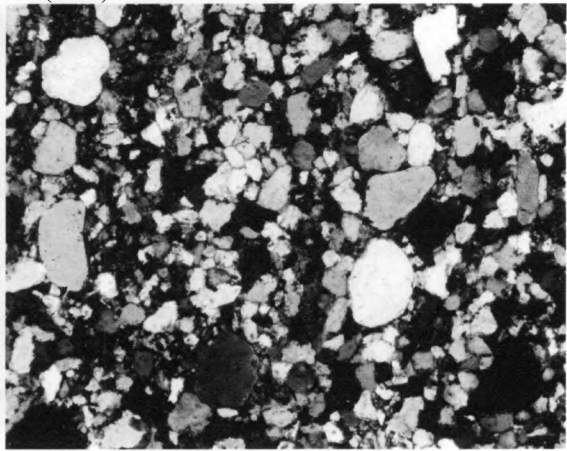
TS (05x)



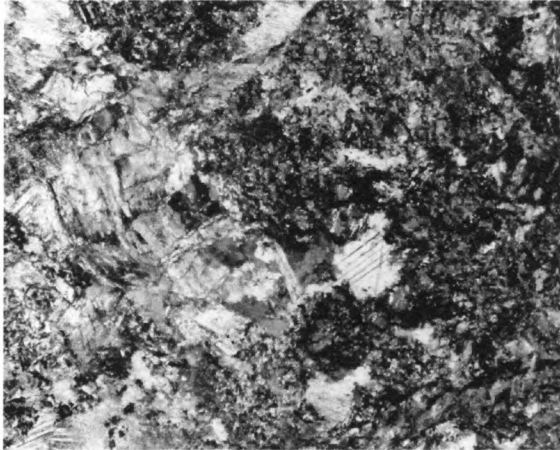
T (05x)



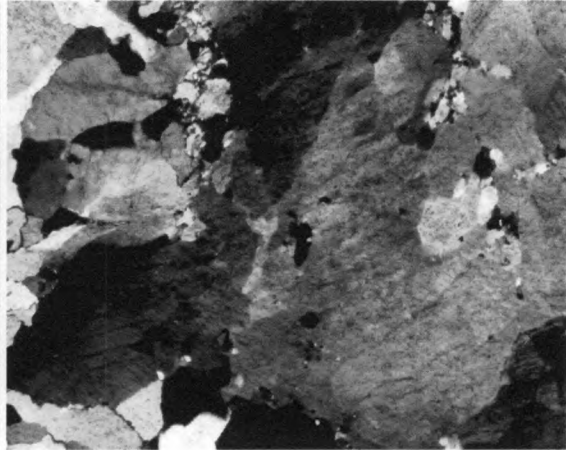
WS (05x)



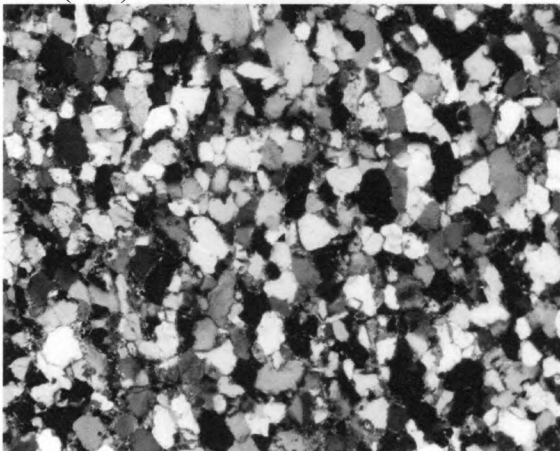
RS (05x)



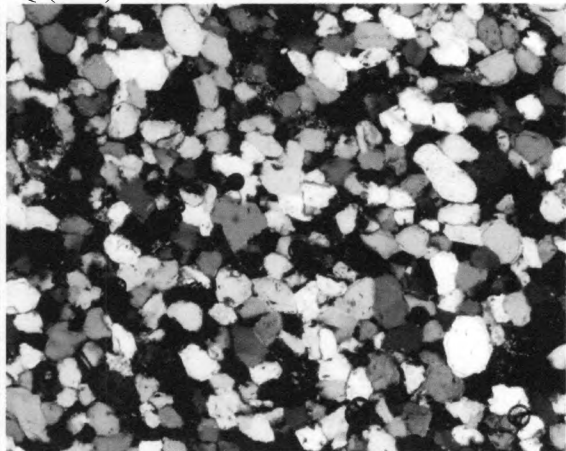
RM (05x)



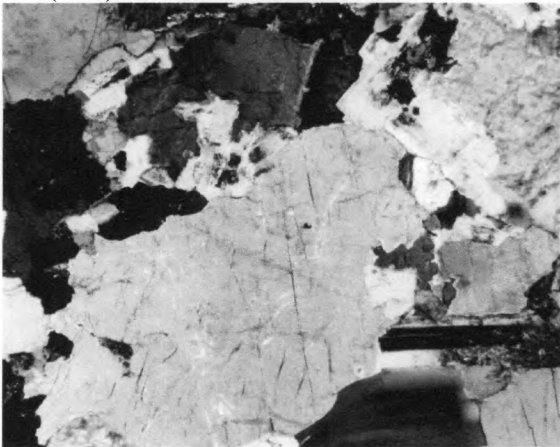
Q (05x)



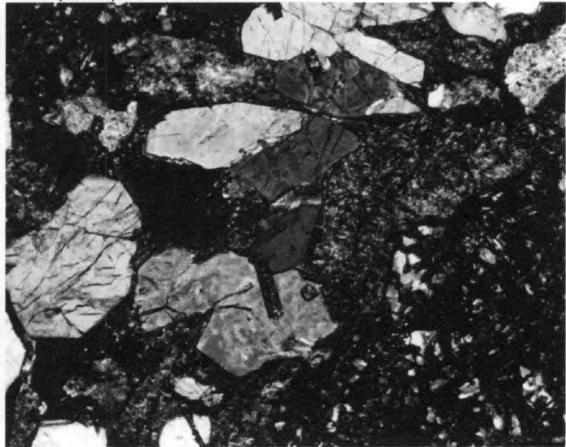
PS (05x)



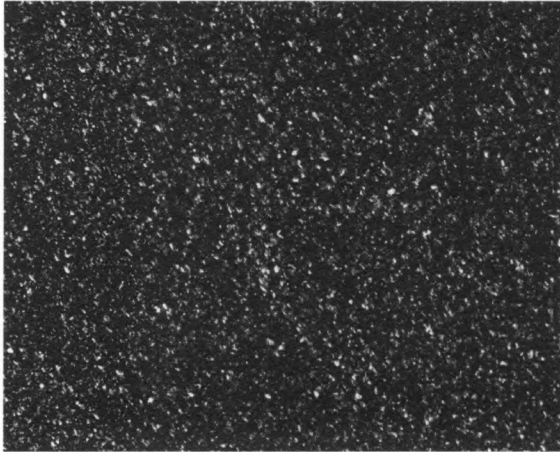
LI (05x)



GG (02x)



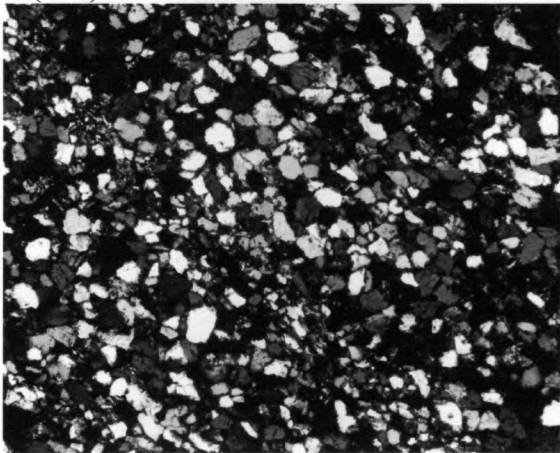
G (05x)



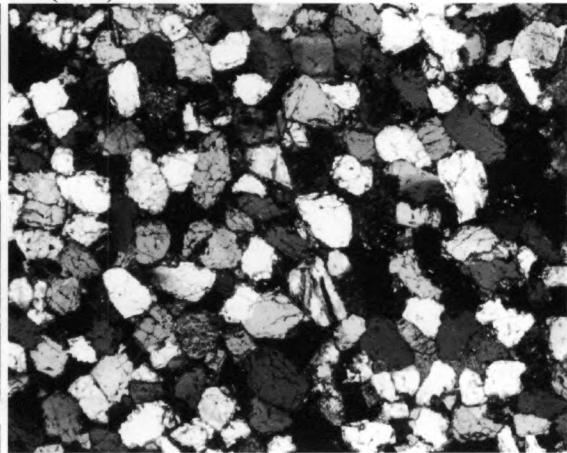
E (05x)



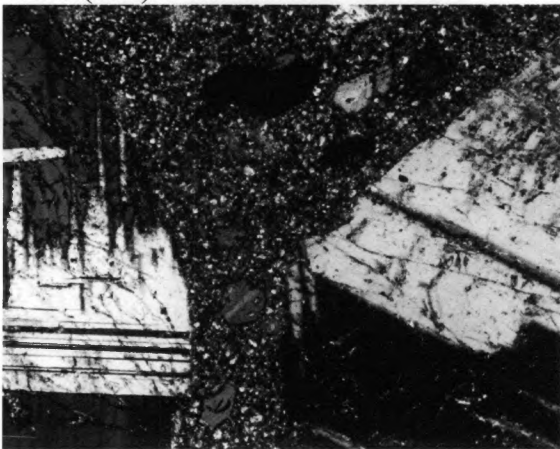
A (05x)



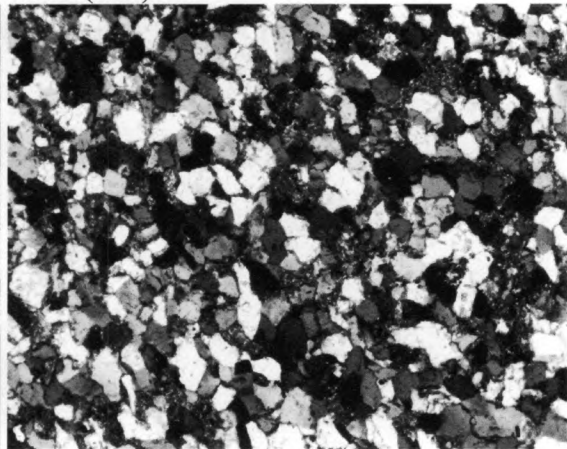
WSA (05x)



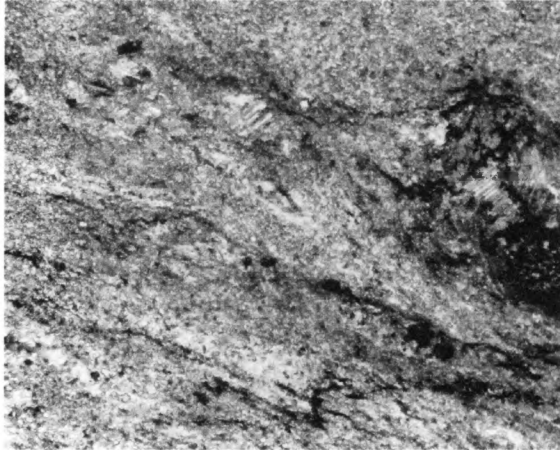
KSS (05x)



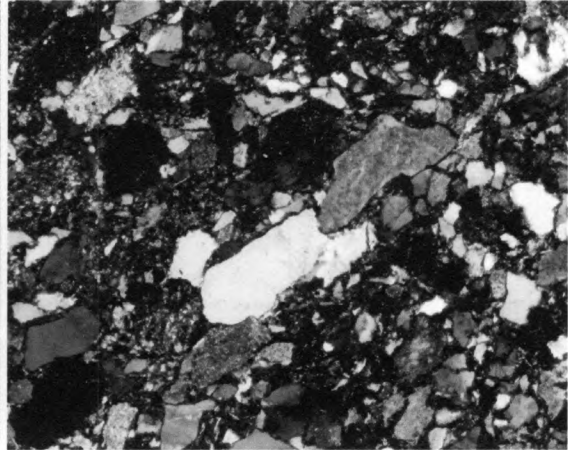
HMD (05x)



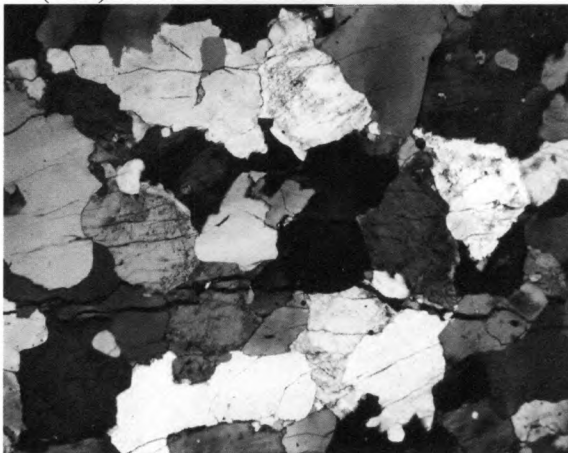
GSS (05x)



L (05x)



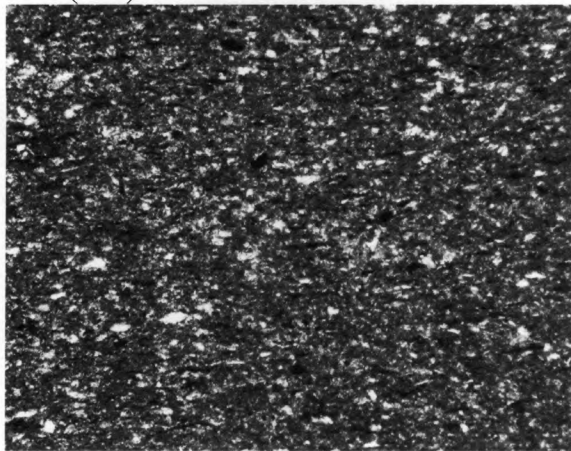
K (05x)



WG (02x)



GM (05x)



M (10x)

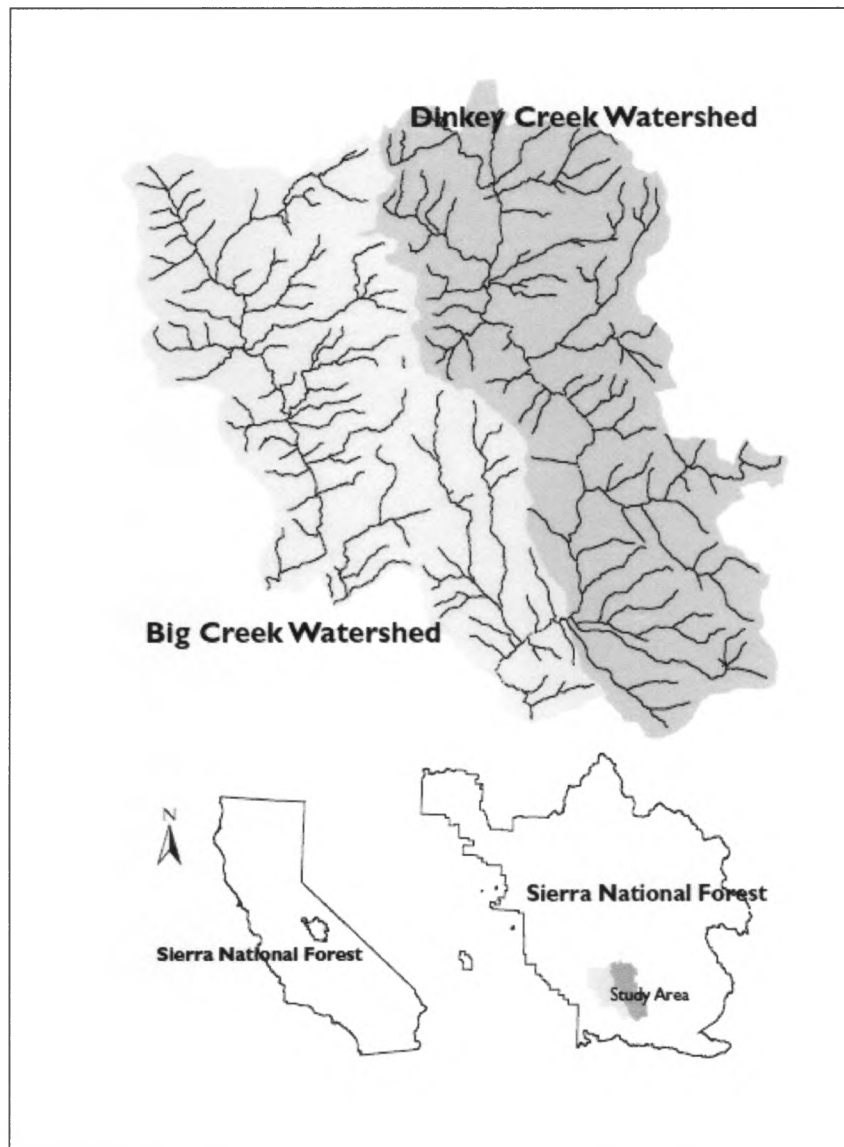


Figure 6: Location map of Dinkey Creek field study in the Sierra Nevada east of Fresno, CA. From Gallegos (2002).

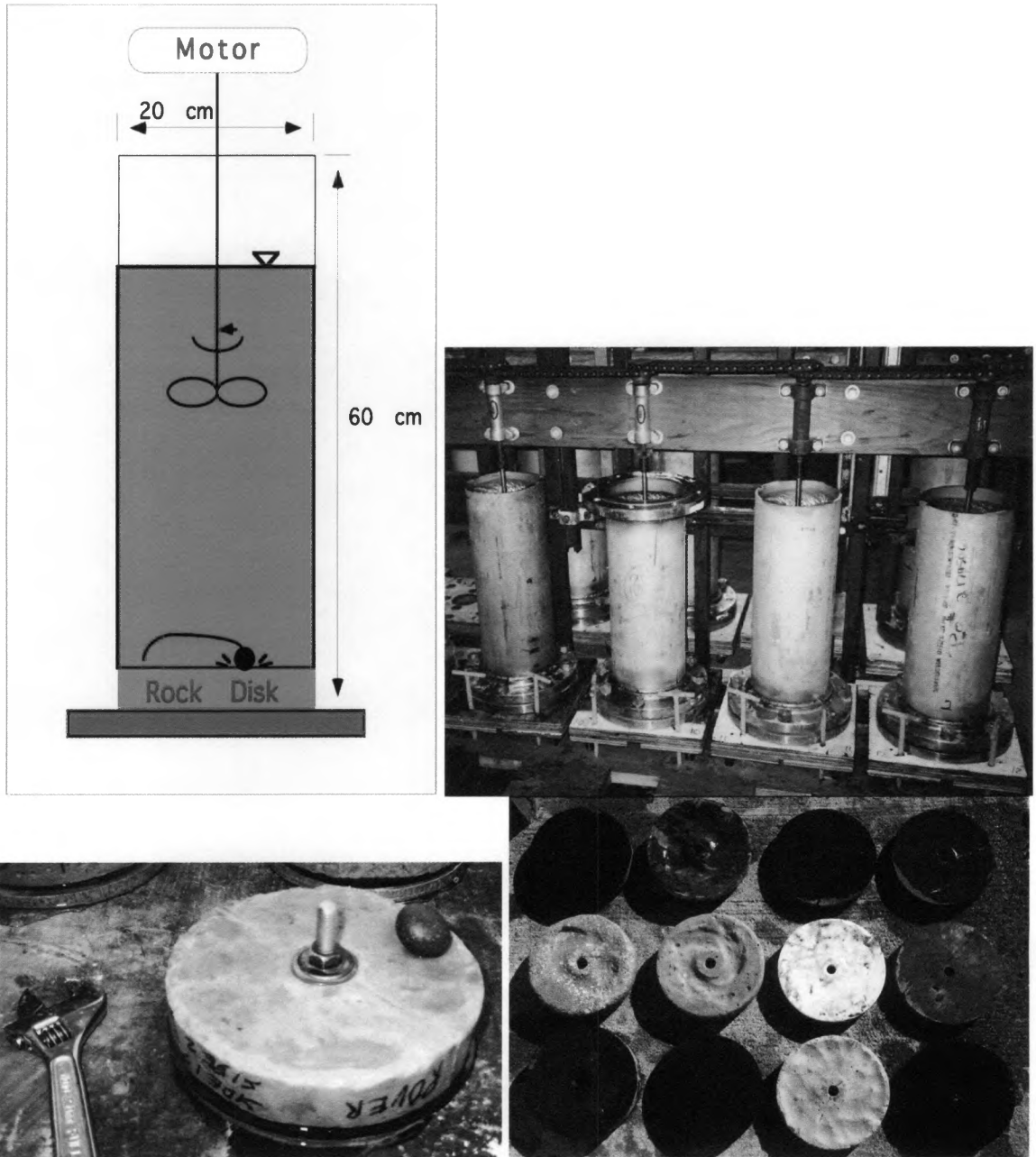


Figure 7: Bedrock Abrasion Mill schematic and photos, from Sklar and Dietrich (2001).

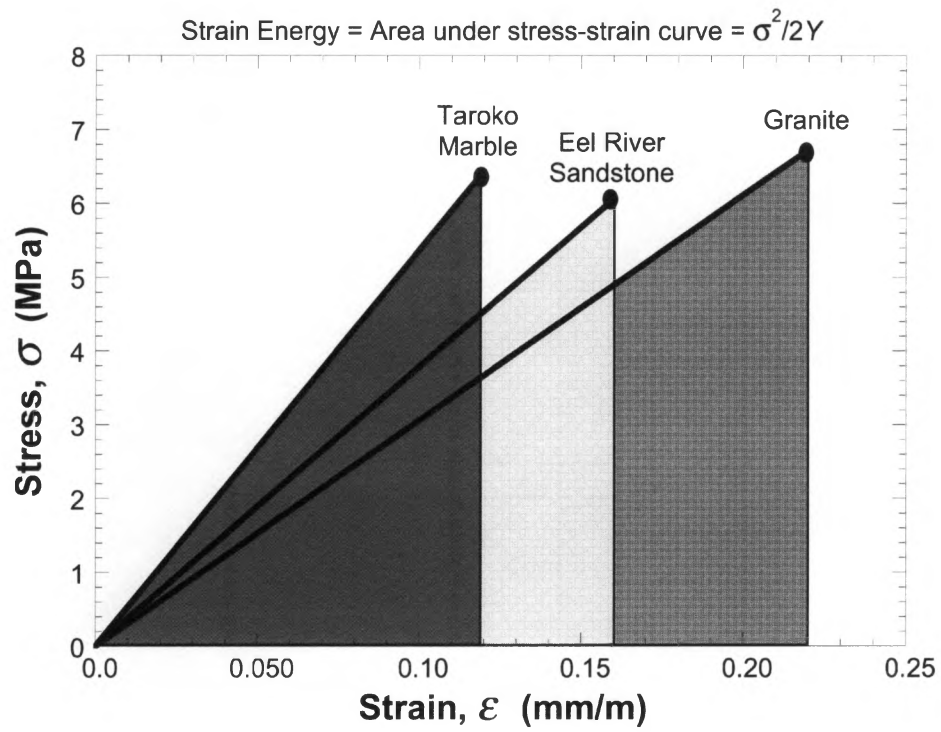


Figure 8: Strain energy is the area under the curves in this plot of stress versus strain.

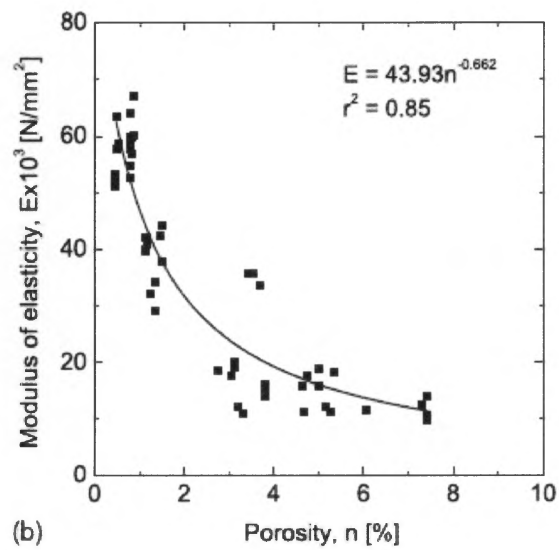
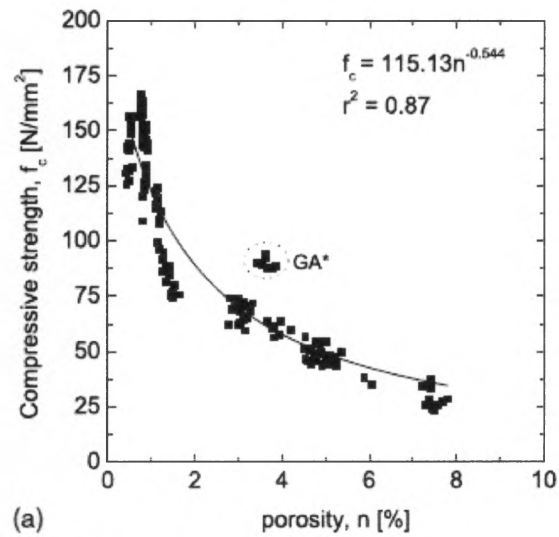


Figure 9: The effects of weathering can be measured as an increase in porosity. Power-law relation between both strength and elasticity with porosity. From Vasconcloos et al. (2009).

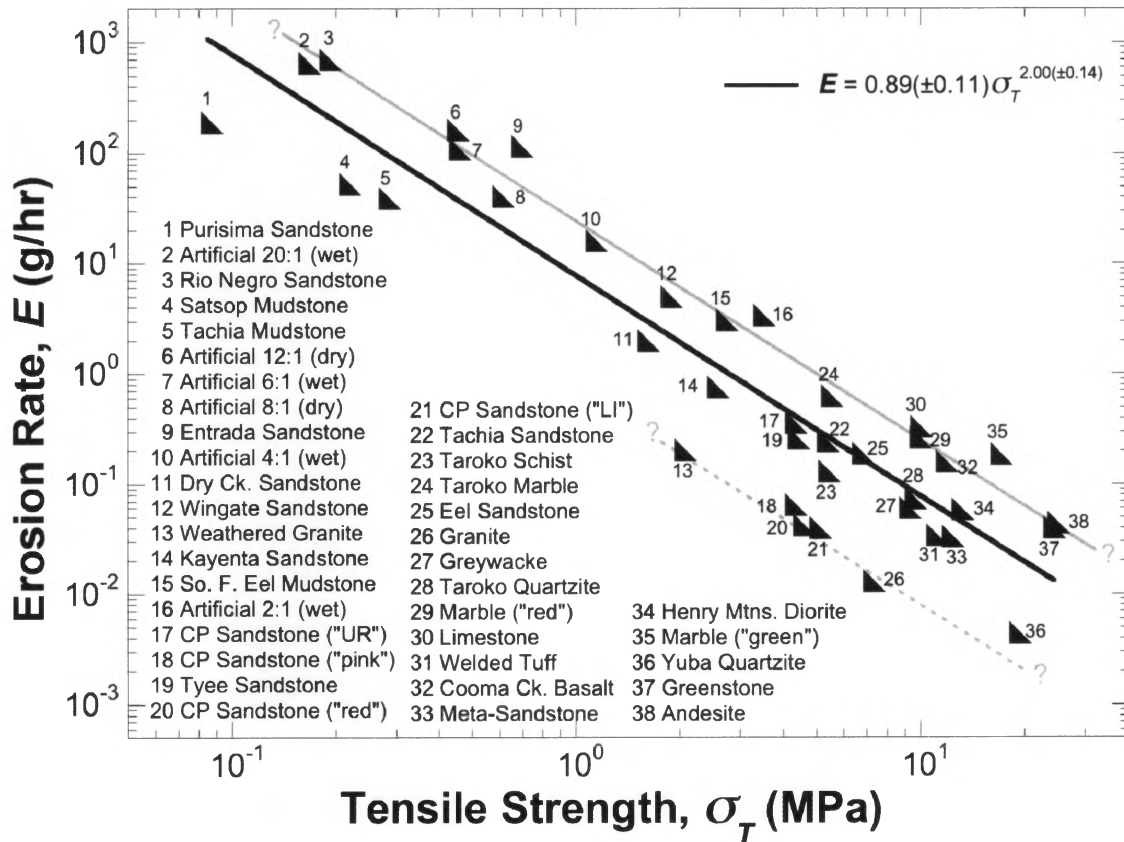


Figure 10: Log-log regression of erosion rate versus tensile strength; increased dataset from Sklar and Dietrich (2001). Theory predicts the scaling relationship with the square of strength (slope of -2). However there is no theory to predict the intercept of the best-fit line. The dashed line represents a coarse-grained subset of the rocks, while the gray line represents a non-porous and fine-grained subset of the data.

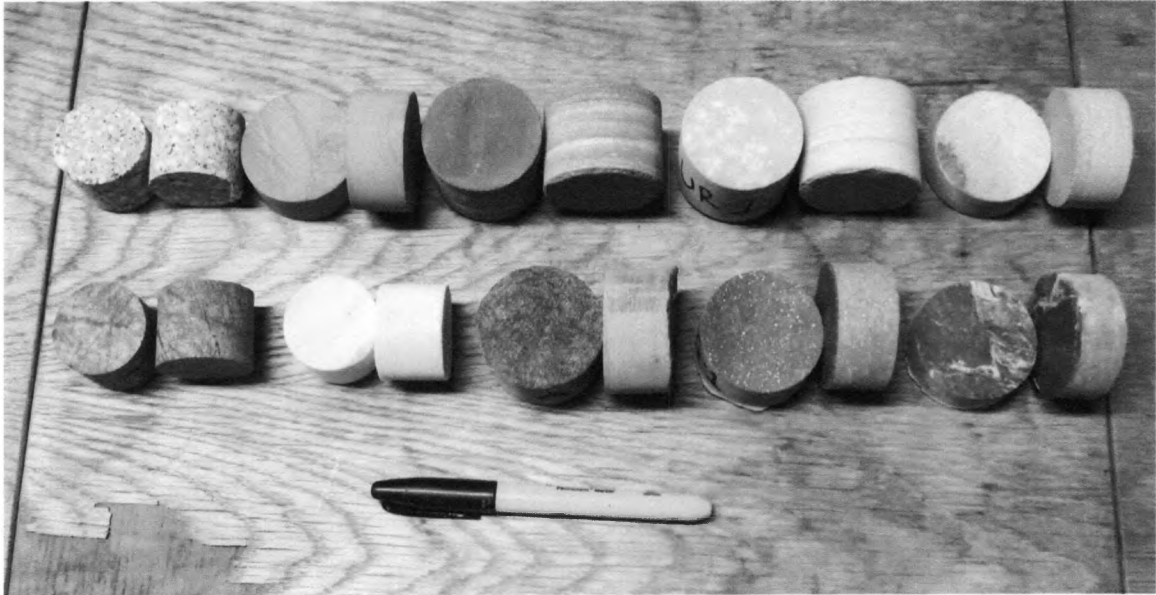


Figure 11: Tensile strength and porosity samples.

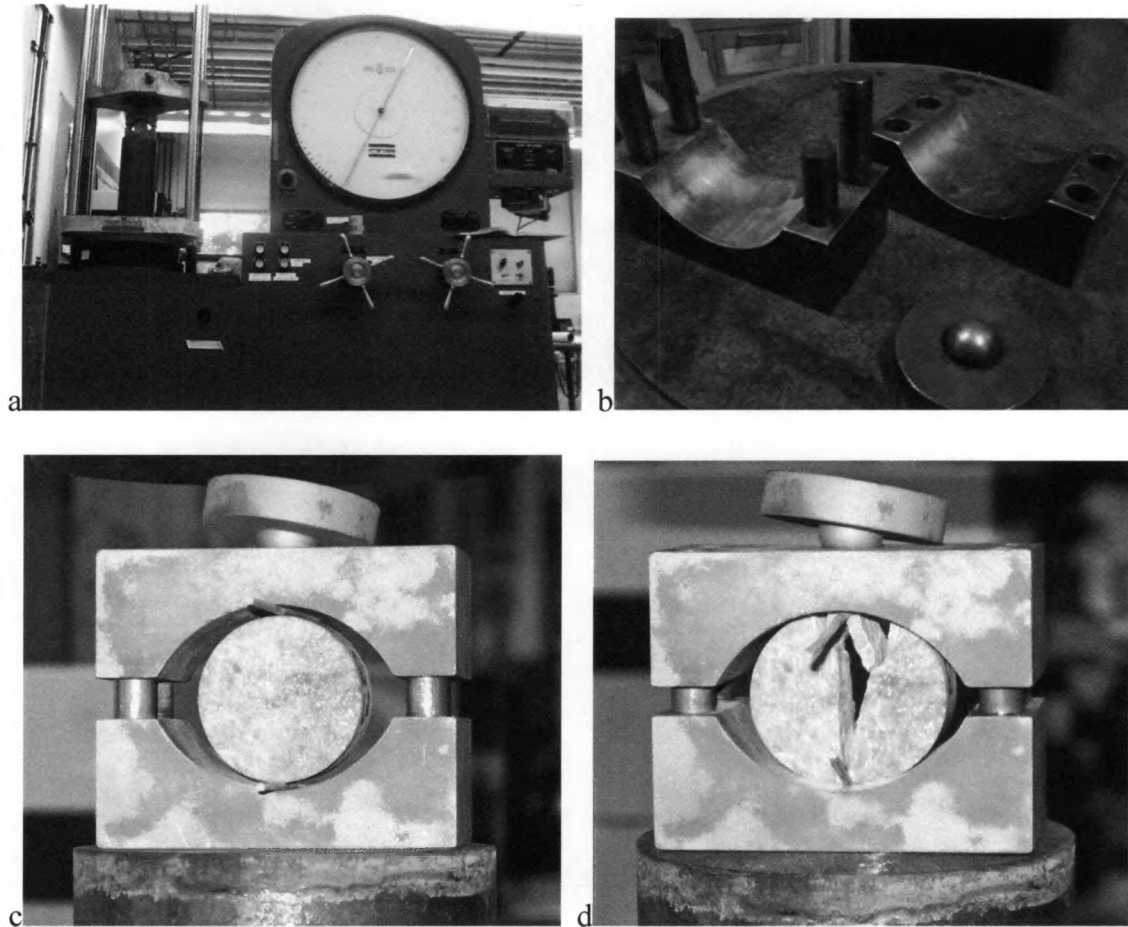


Figure 12: Tinius Olsen compression machine (a) and strength fixture (b), fixture with rock cylinder before (c) and after (d) tensile strength test. Bamboo sticks help disperse load across multiple mineral grains opposed to single point loading.

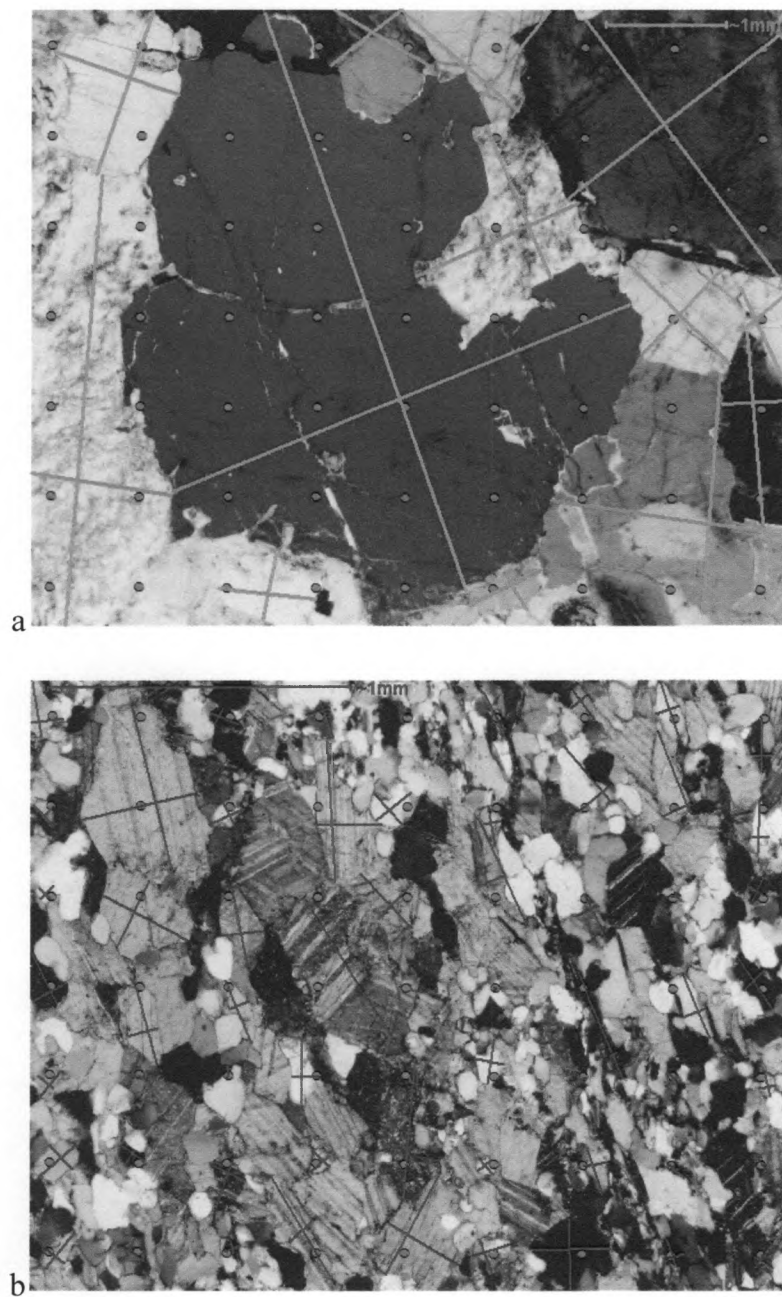


Figure 13: Photomicrographs of granite (a) and quartzite (b) with grid overlaid for point counts. Grid overlaid and axis measured in ARCGIS.



Figure 14: Drying oven used in porosity measurements. Oven is located in Hensil Hall room 112 at SFSU.

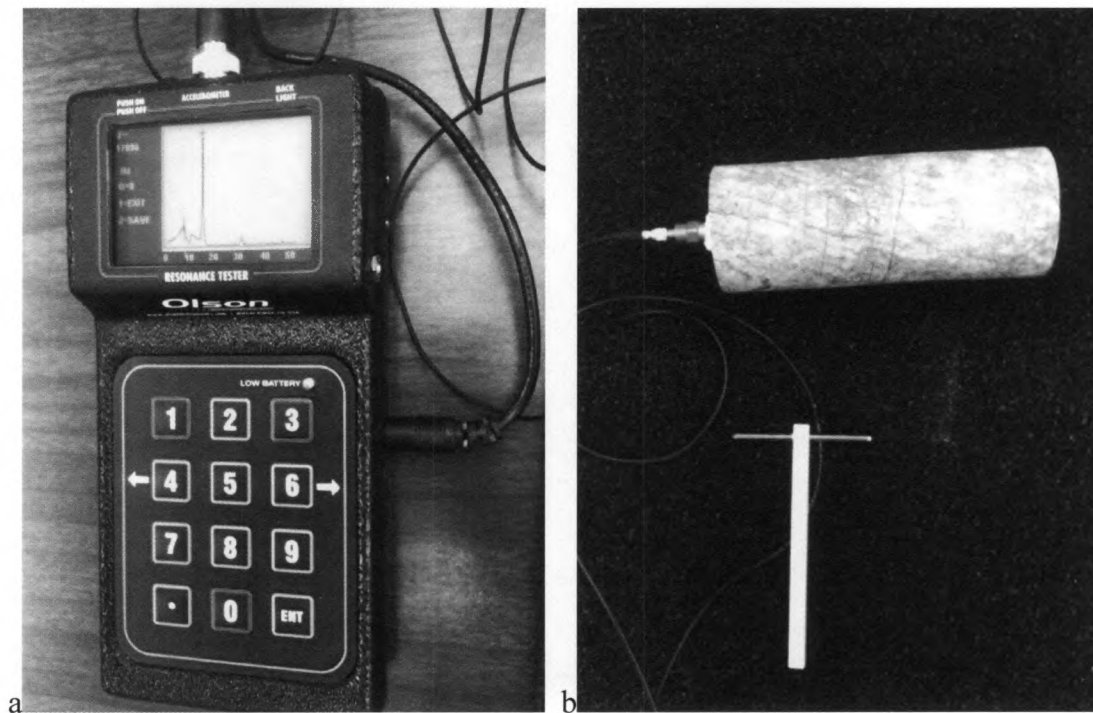


Figure 15: Olson resonant frequency tester setup for elasticity measurements, in the longitudinal direction. Tester (a) is connected to accelerometer (b) affixed to the rock core. Test is conducted by striking the center of cylinder, opposite the accelerometer, with the hammer in bottom of (b).

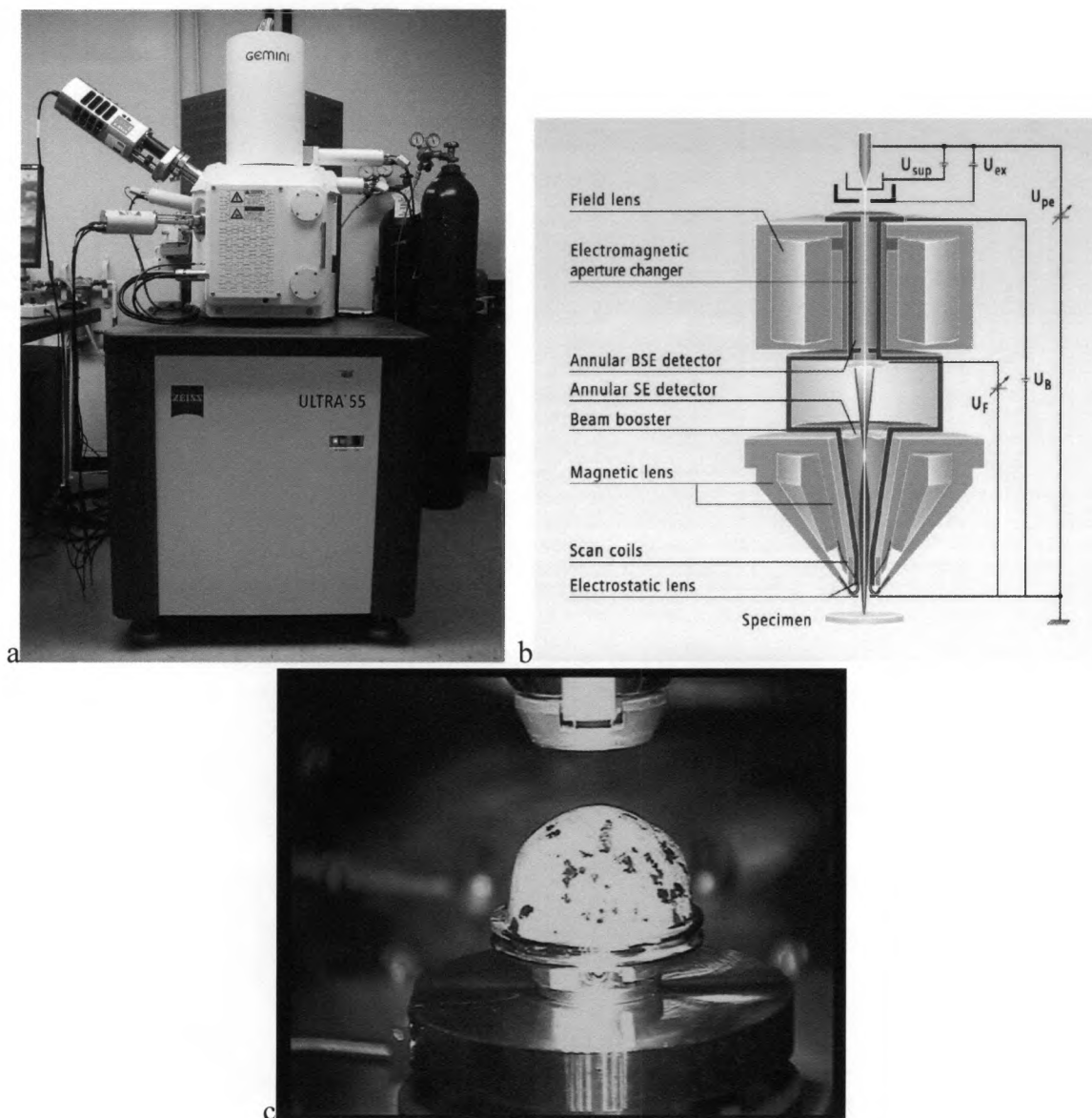


Figure 16: Carl Zeiss Ultra-55 Field Emission SEM (a) and schematic of column (b). Inset (c) shows mounted Providence Creek granodiorite inside the SEM vacuum chamber, below the electron beam column and seen through the TV camera mode.

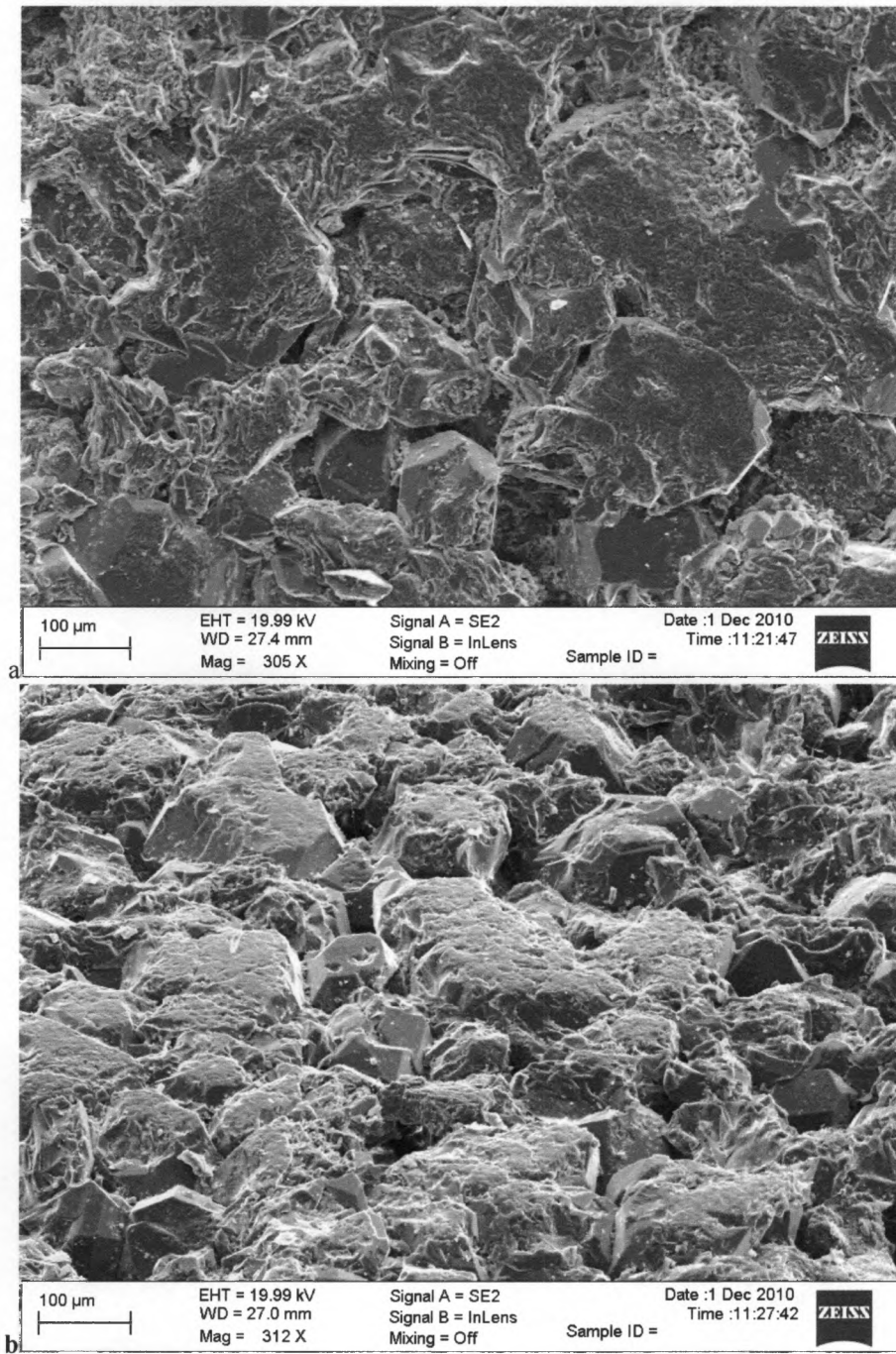


Figure 17: SEM images of un-tilted (a) and tilted (b) abraded sandstone (LI in Figure 5).

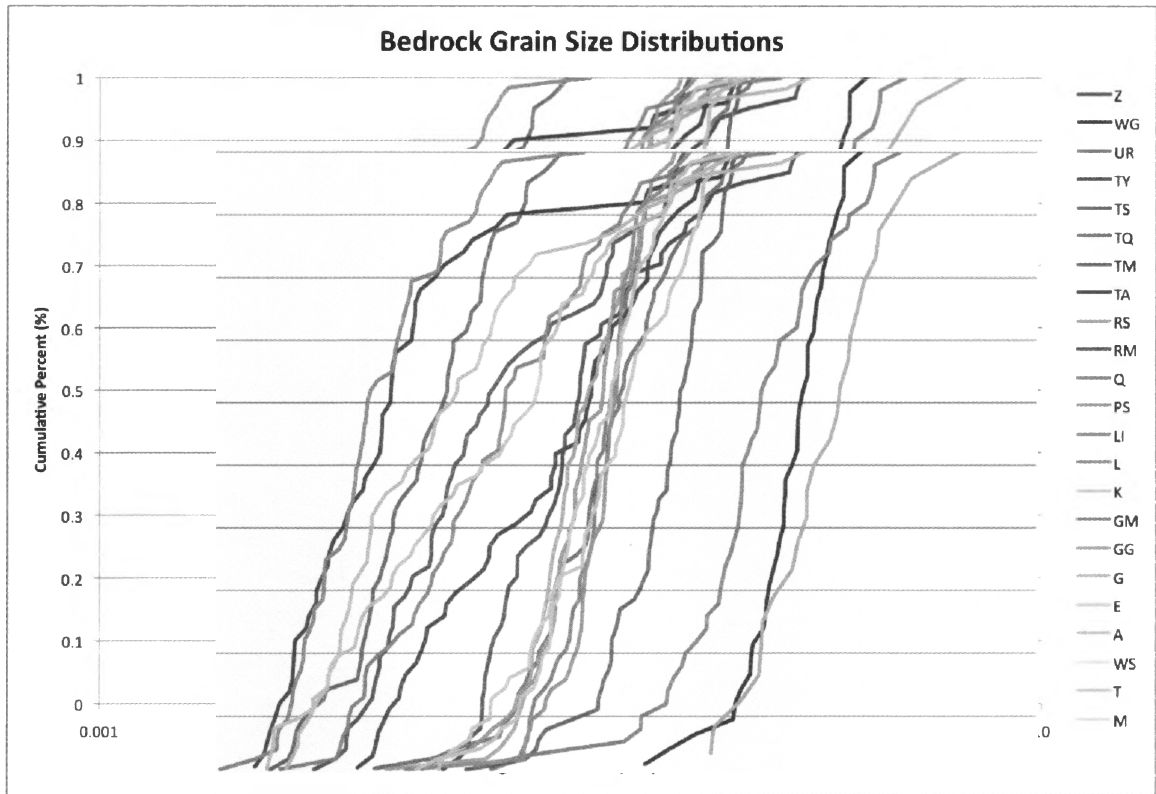


Figure 19: Cumulative mineral size distribution for bedrock data set.

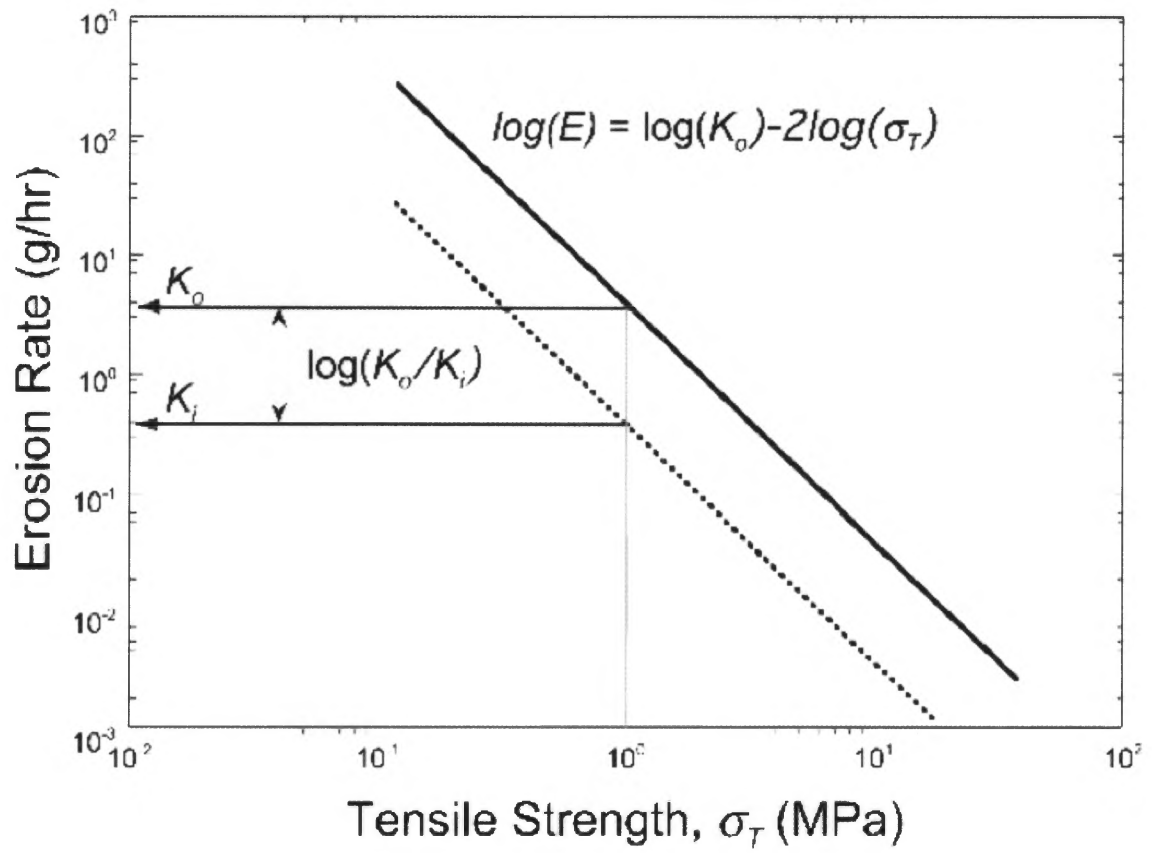


Figure 20: Schematic of K , defined as distance from best-fit line.

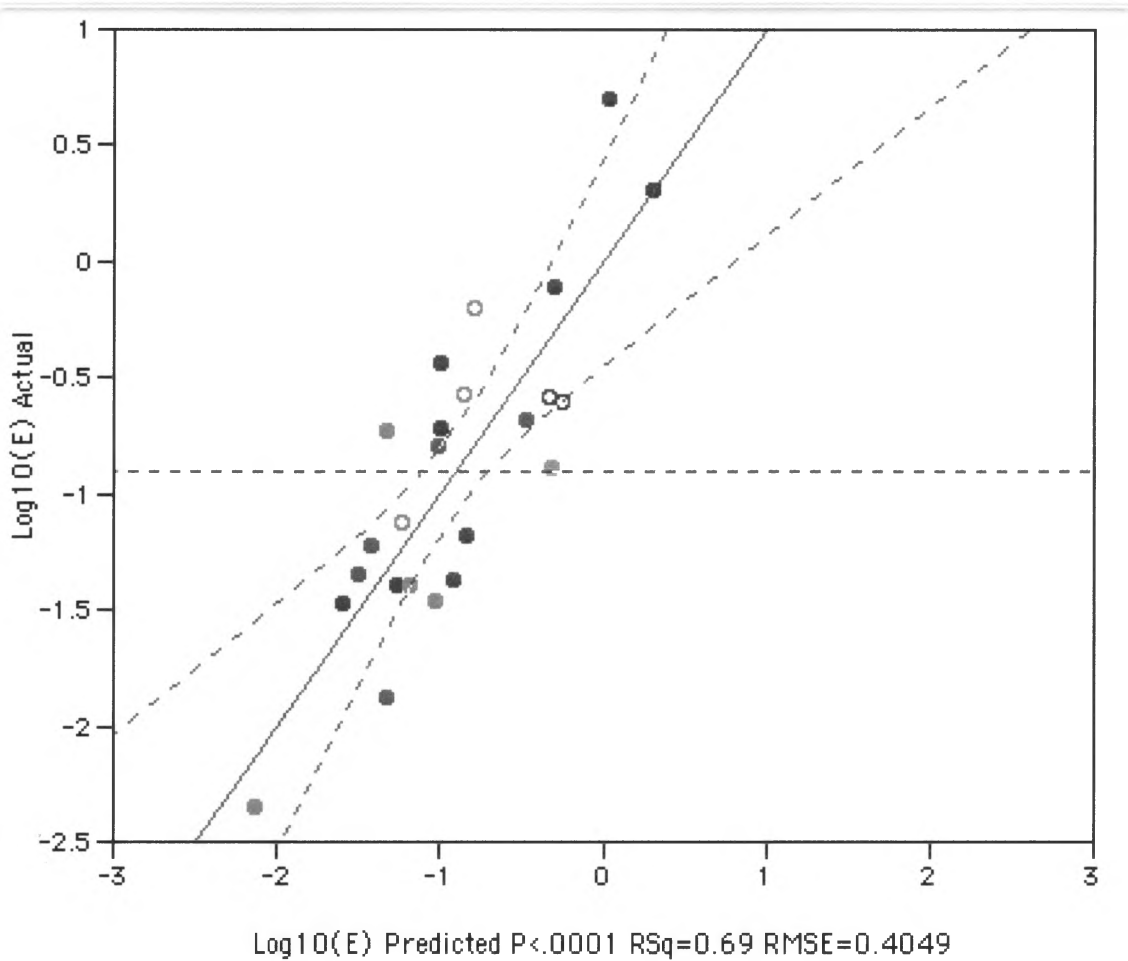
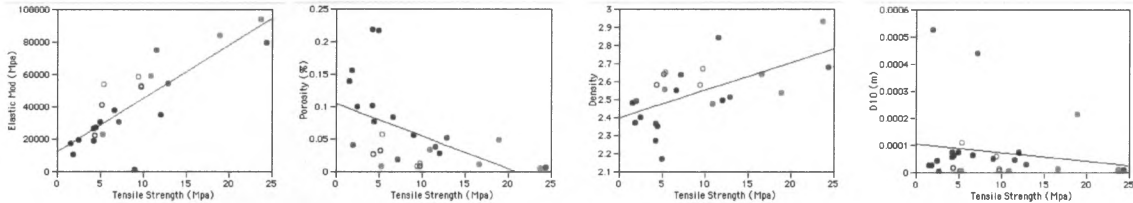
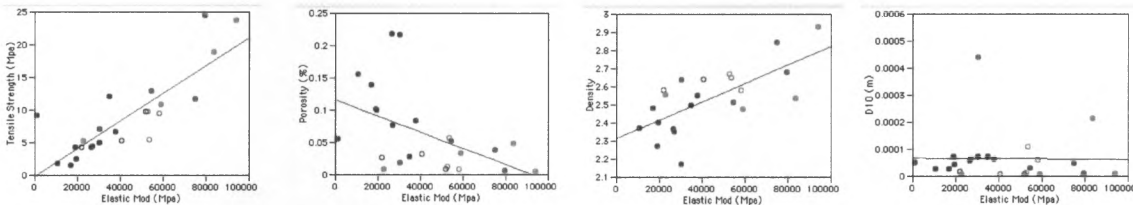


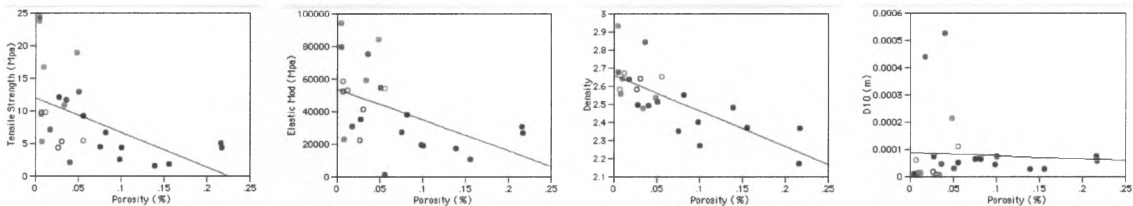
Figure 21: JMP statistical output regression of measured erosion rates vs. multivariate model in Log-Log space. The model yielding the best parameter estimates and R^2 value (0.69) models erosion as a function of strength, grain size, and density. Modeling erosion only with strength, for the same data points, yields an R^2 value of 0.47; so grain size and density couple together to explain nearly a quarter (~ 0.22) of the remaining variance. Red, green, and blue represent igneous, metamorphic, and sedimentary rocks. Open circles represent calcite cement, versus silica.



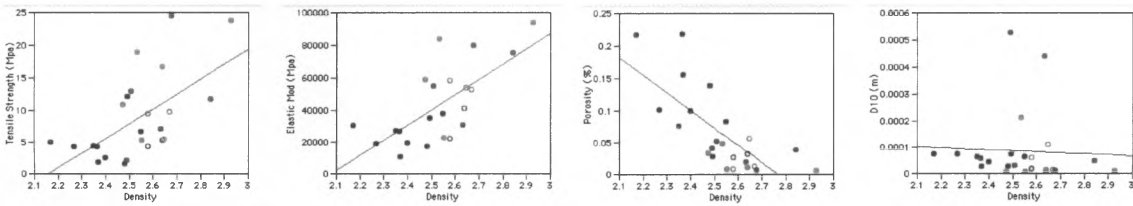
Tensile strength versus elastic modulus, porosity, density, and grain size (D10).



Elastic modulus versus tensile strength, porosity, density, and grain size (D10).



Porosity versus tensile strength, elastic modulus, density, and grain size (D10).



Density versus tensile strength, elastic modulus, porosity, and grain size (D10).

Figure 22: Regression plots showing the covariation of the following bedrock rock properties: tensile strength, elasticity, porosity, density, and grain size measured as D10. The red, green, and blue circles respectively represent the igneous, metamorphic, and sedimentary rocks tested. The open circles represent rock types with calcite cement, while the solid circles are siliceous rocks. All of the variables covary with each other, except grain size, with more than the 98% significance in the relationships. Grain size is the only new truly independent information, which supports its role in an explanatory expression for relative erodibility.

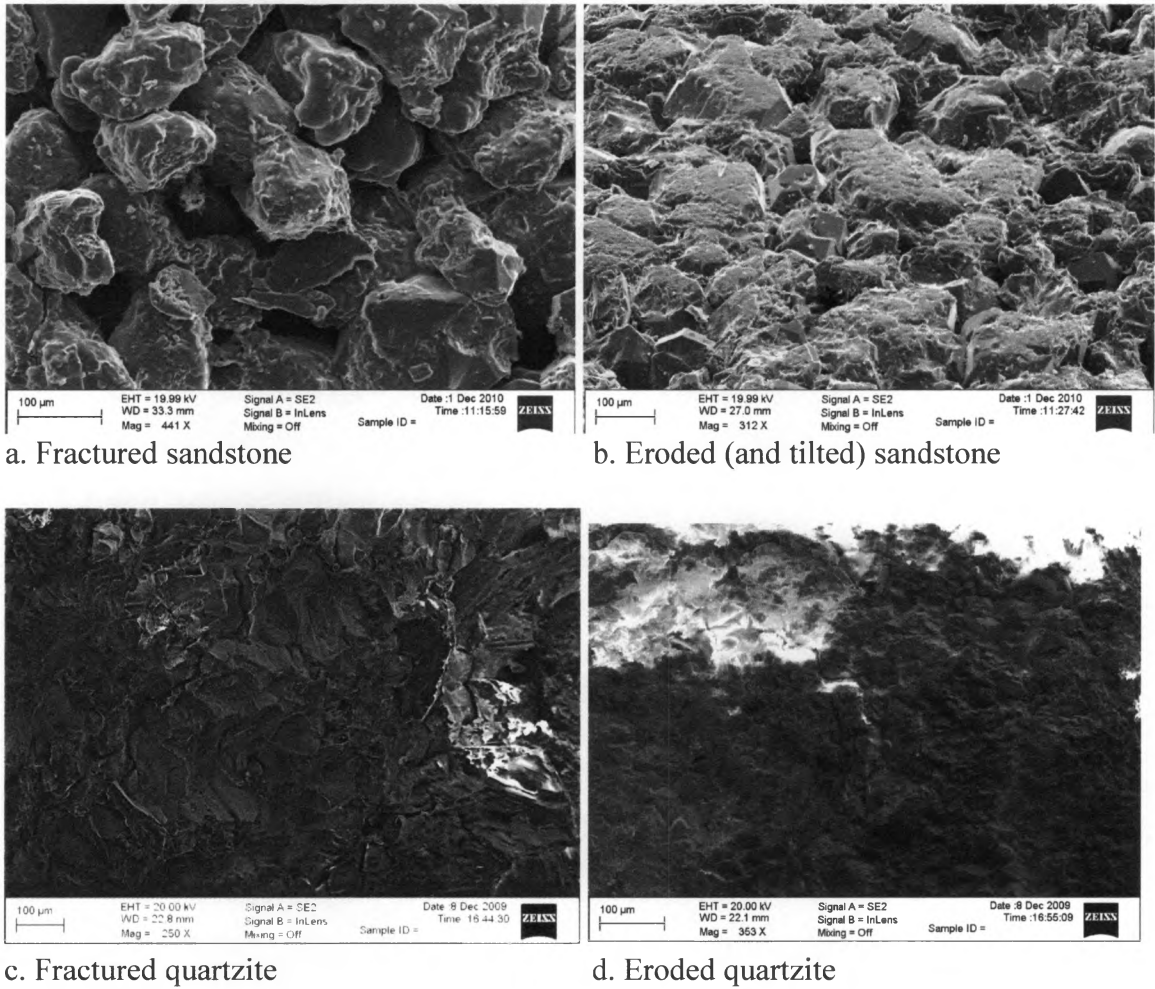
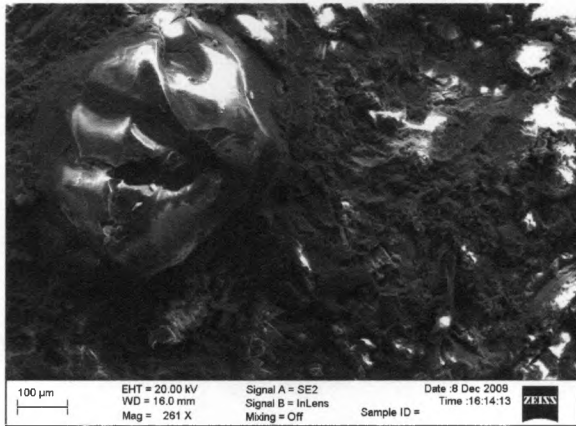
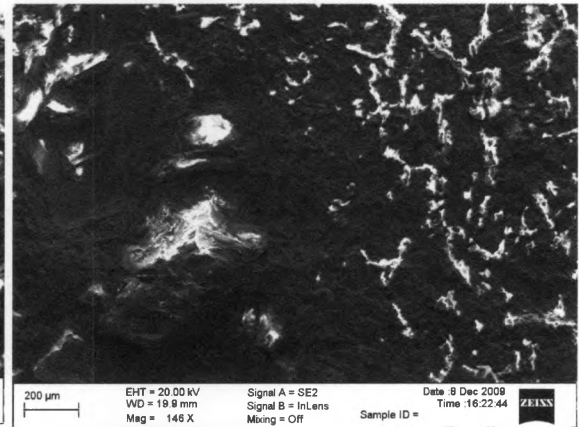


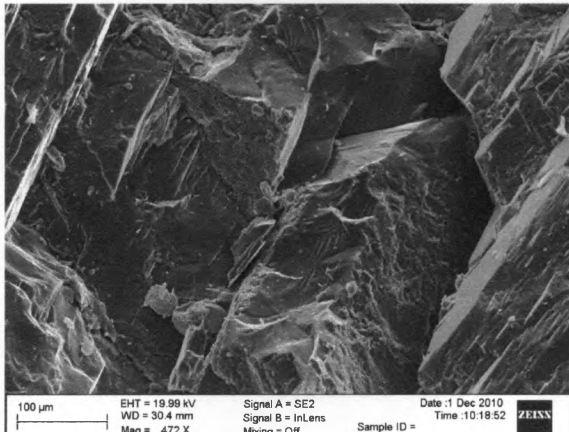
Figure 23: SEM images of bedrock erosion and fracture surfaces. Eroded surfaces were sampled directly from BAM discs used in eroded experimentally and compare sandstone (porous) and quartzite (nonporous).



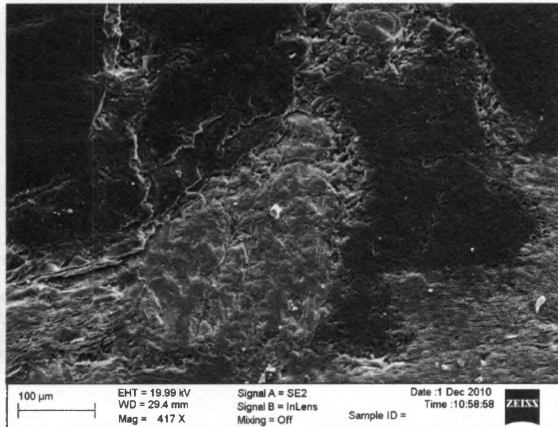
a. Fractured basalt



b. Eroded basalt



c. Fractured granite



d. Eroded granite

Figure 24: SEM images of bedrock erosion and fracture surfaces. Eroded surfaces were sampled directly from BAM discs used in experiments. Rocks shown are fine-grained basalt and coarse-grained granite. Note the silt particles in (d) on the surface of the granite.

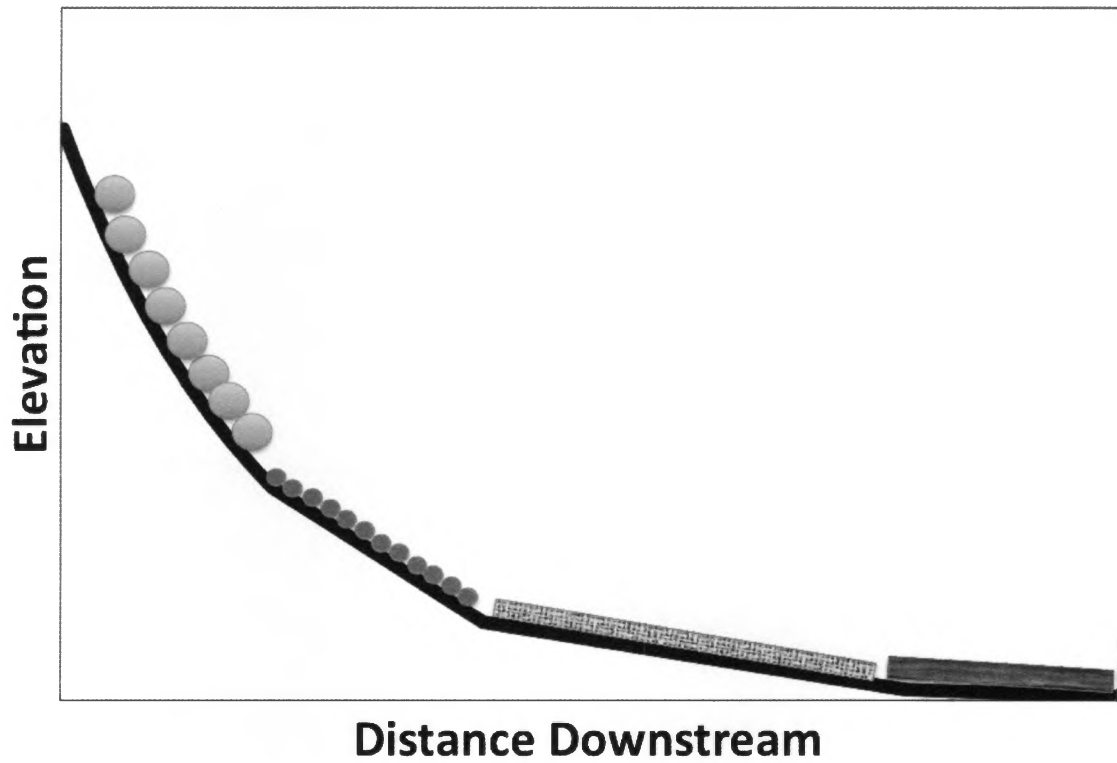
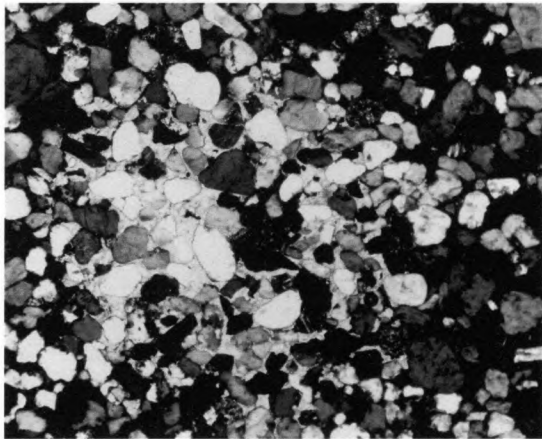
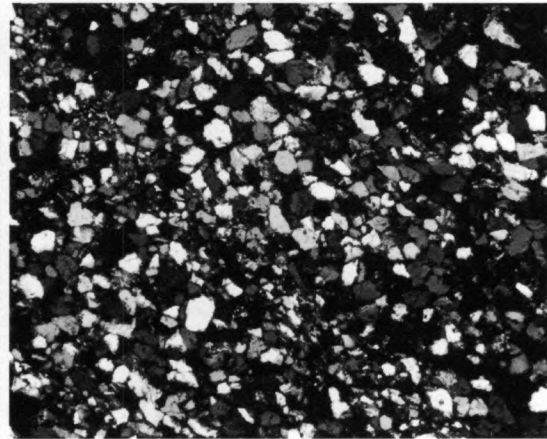


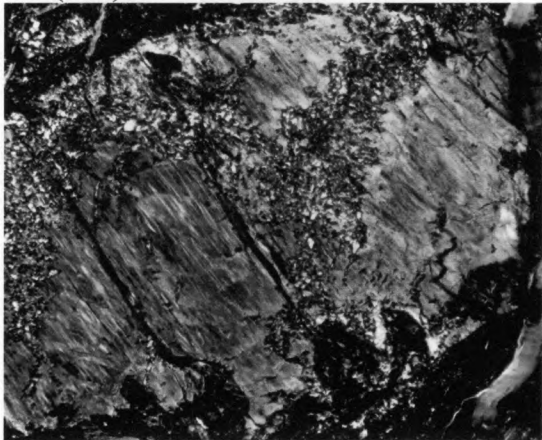
Figure 25: Schematic of downstream fining. Circles represent relative sediment size, showing that as slope decreases when rivers flow down slope, the grain sizes present in river channels also generally decrease in size; from boulders to gravel to sand to silt.



NS (05x)



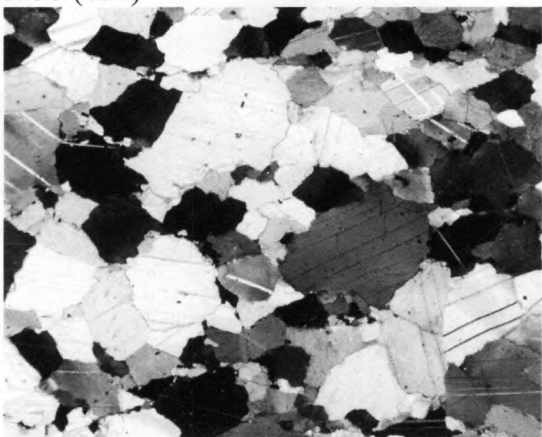
WSA (05x)



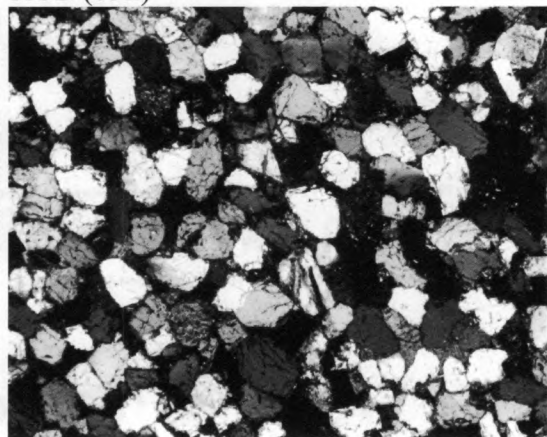
RCS (05x)



RCB (05x)



OQ (05x)

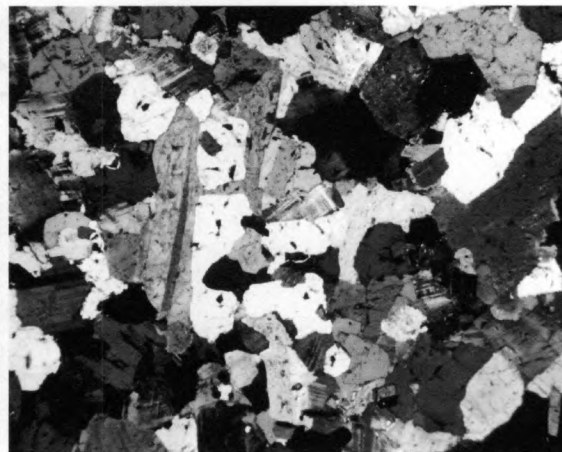


KSS (05x)

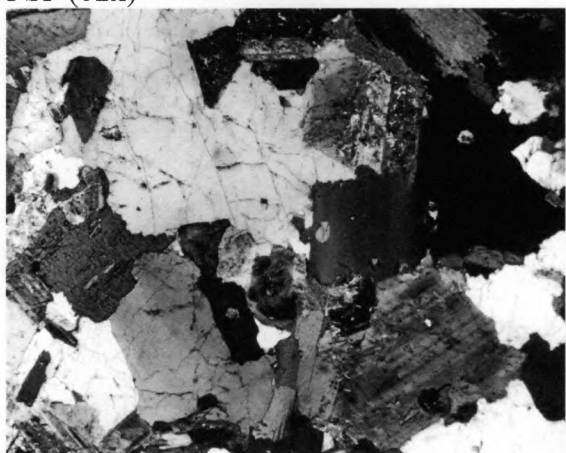
Figure 26: Photomicrographs for entire sediment tumbling data set.



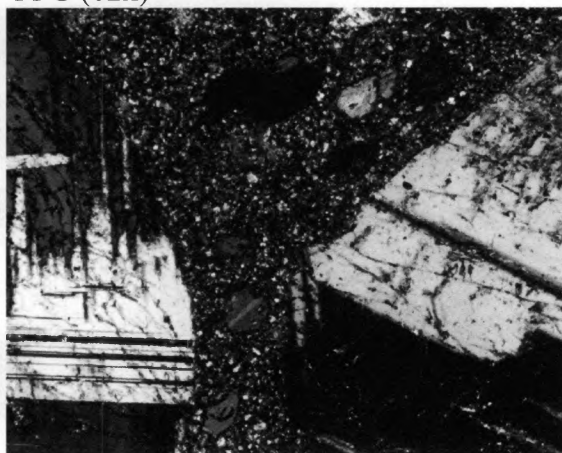
PSP (02x)



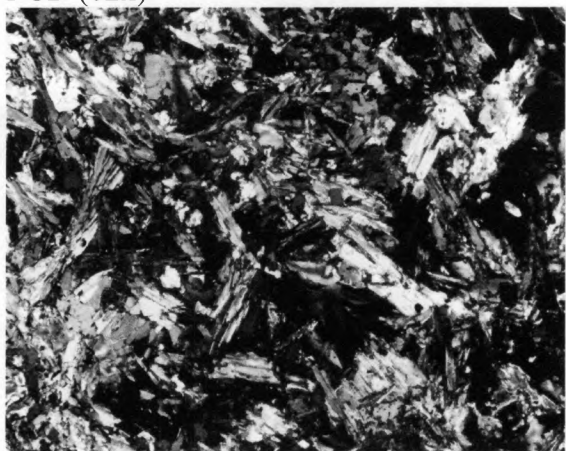
PFG (02x)



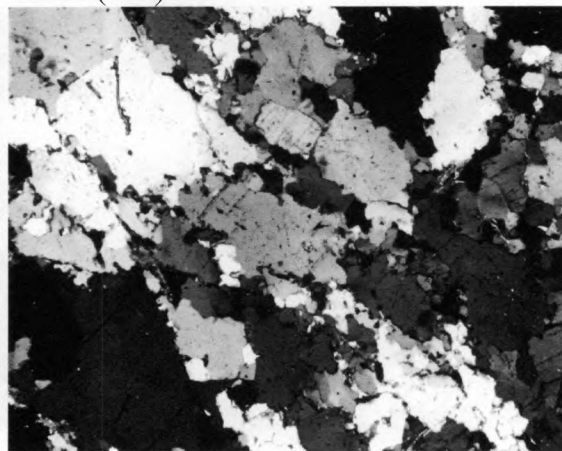
PGD (02x)



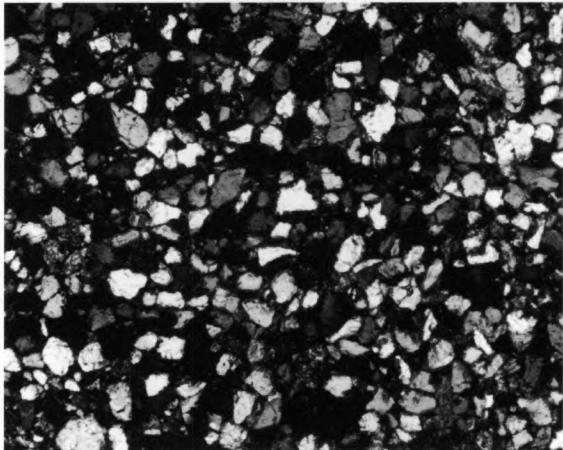
HMD (05x)



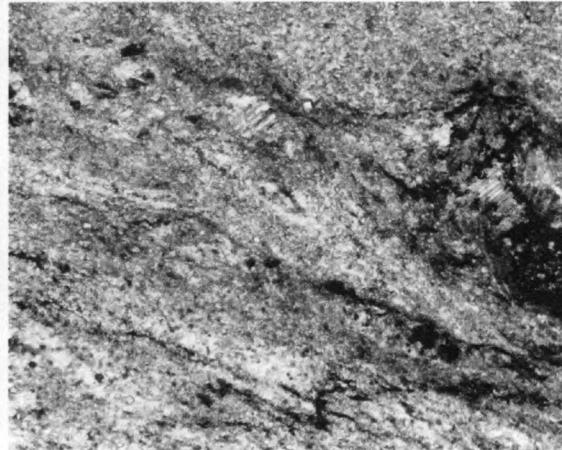
DSH (05x)



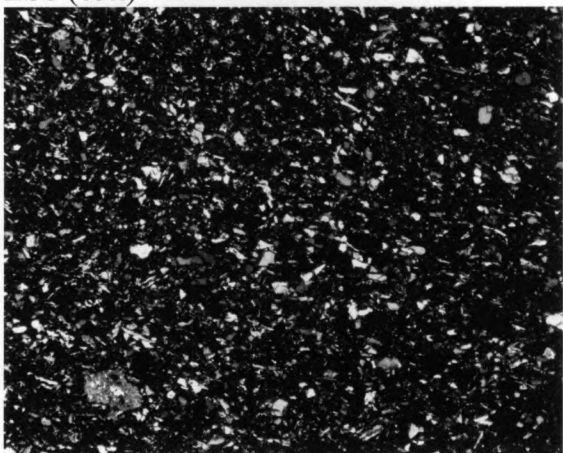
DCQ (05x)



ESS (05x)



L (05x)



RCG (05x)



Figure 27: Picture of tumbled rock types from the Sierra Nevada, CA. Clockwise from upper left: Providence Ck granite, Providence Ck granodiorite, Providence Ck diorite, Dinkey Ck biotite hornfels, and Dinkey Ck quartzite. Gravel clasts started at ~100 g and were tumbled until rounded and measured abrasion rates stabilized.

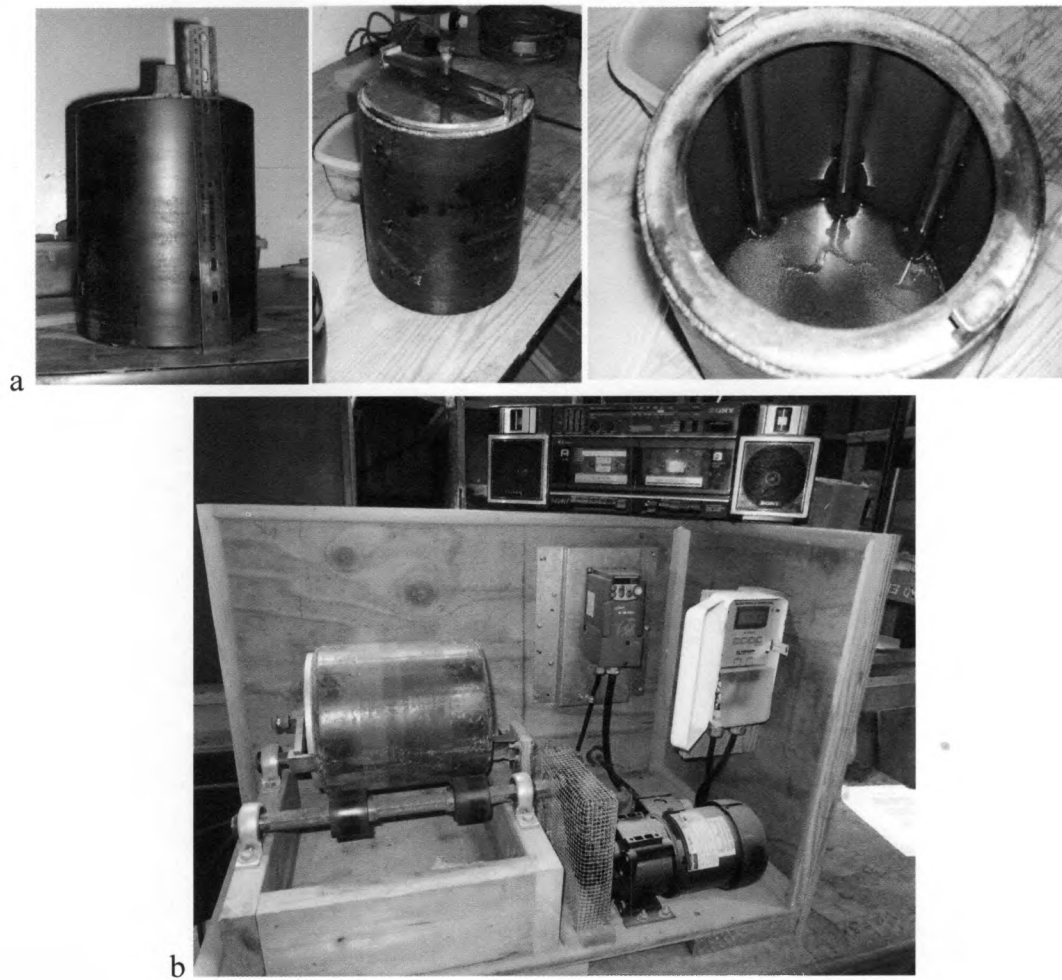


Figure 28: Barrel (a) and tumbler (b) used in sediment abrasion experiments. Tumbler setup consists of an electronic timer which turns on the frequency controller which engages the motor at desired rpm for the programmed time.

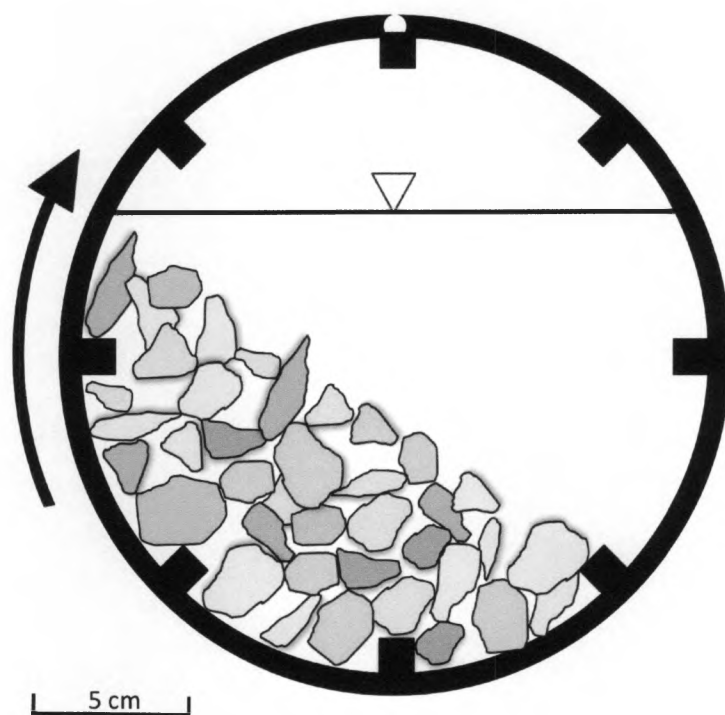


Figure 29: Schematic of barrel tumbler filled with sediment and water. Gray shapes represent sediment grains and triangle indicates water level, arrow shows direction of rotation. Sediment is lifted up with the rotation of the barrel and bounces and grinds past other grains on the way down.

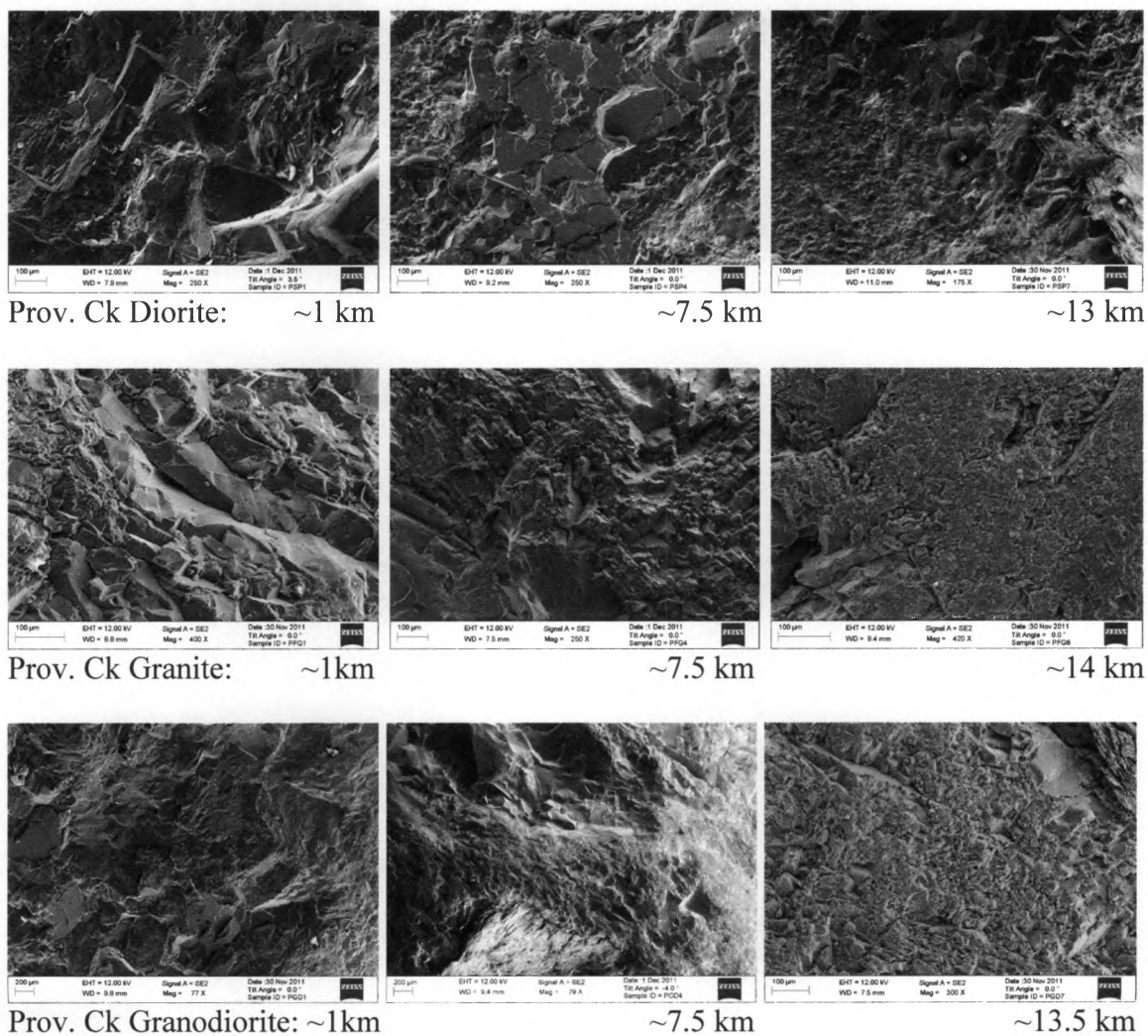


Figure 30: SEM images of the Providence Creek tumbled rocks. Tumbling progression (i.e., increased distance travelled in tumbler) from left to right for each lithology. Diorite is the finest grained rock, while granodiorite is the coarsest grained rock. Note that a similar texture evolves in all three cases, with a textural relief at the scale of mass loss to silt production. Note in many of the images that silt particles are present on the surface of the rocks.

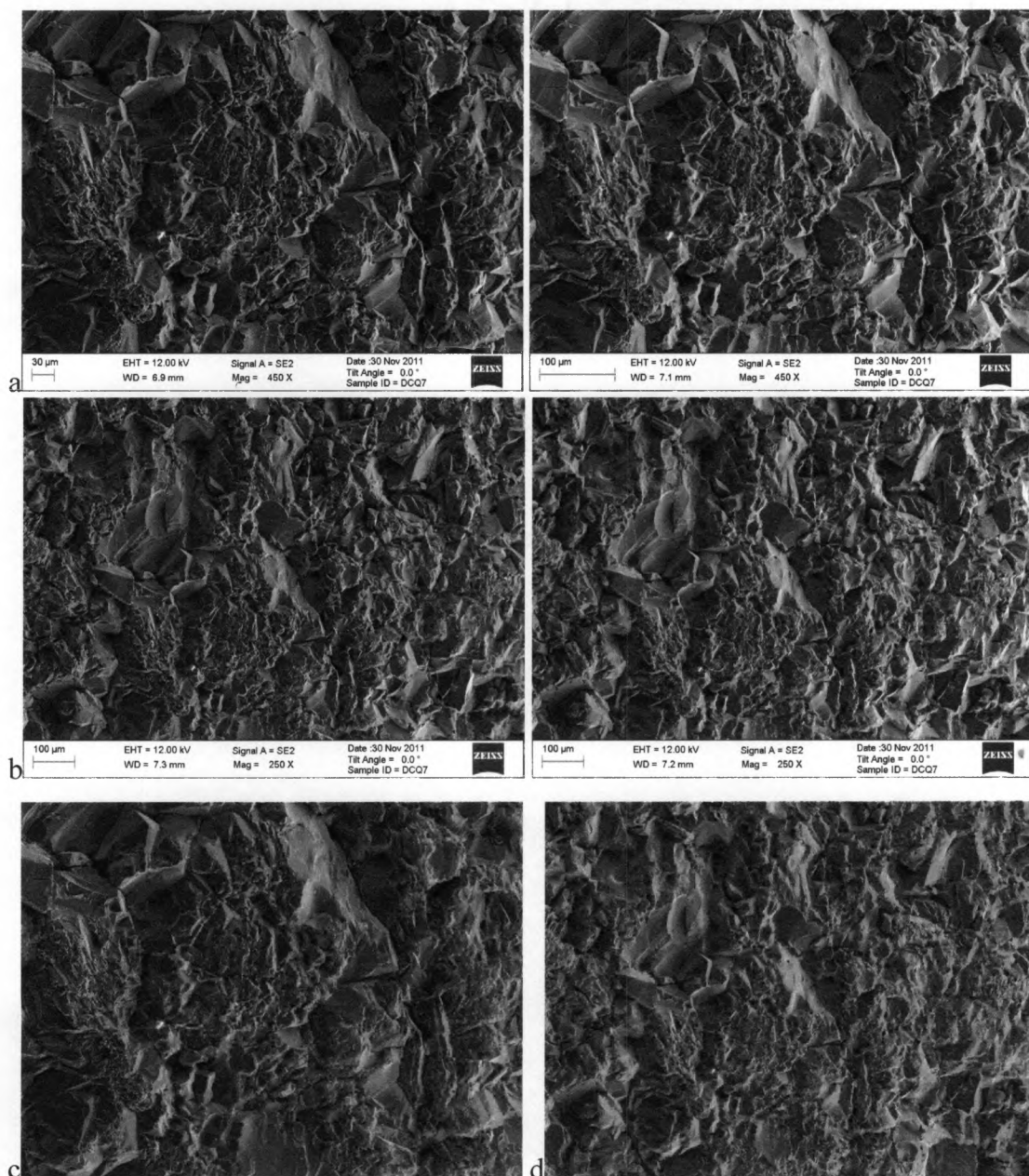


Figure 31: Examples of anaglyph creation. Stereo pairs are created through acquiring a focused image, tilting the surface up to 7° , and refocusing on the same point to acquire the second image. Using SE2 stereo-pairs of images of (a, b) Dinkey Creek quartzite, anaglyphs (c, d respectively) were created to investigate the scale of silt-production and other process-related textures.

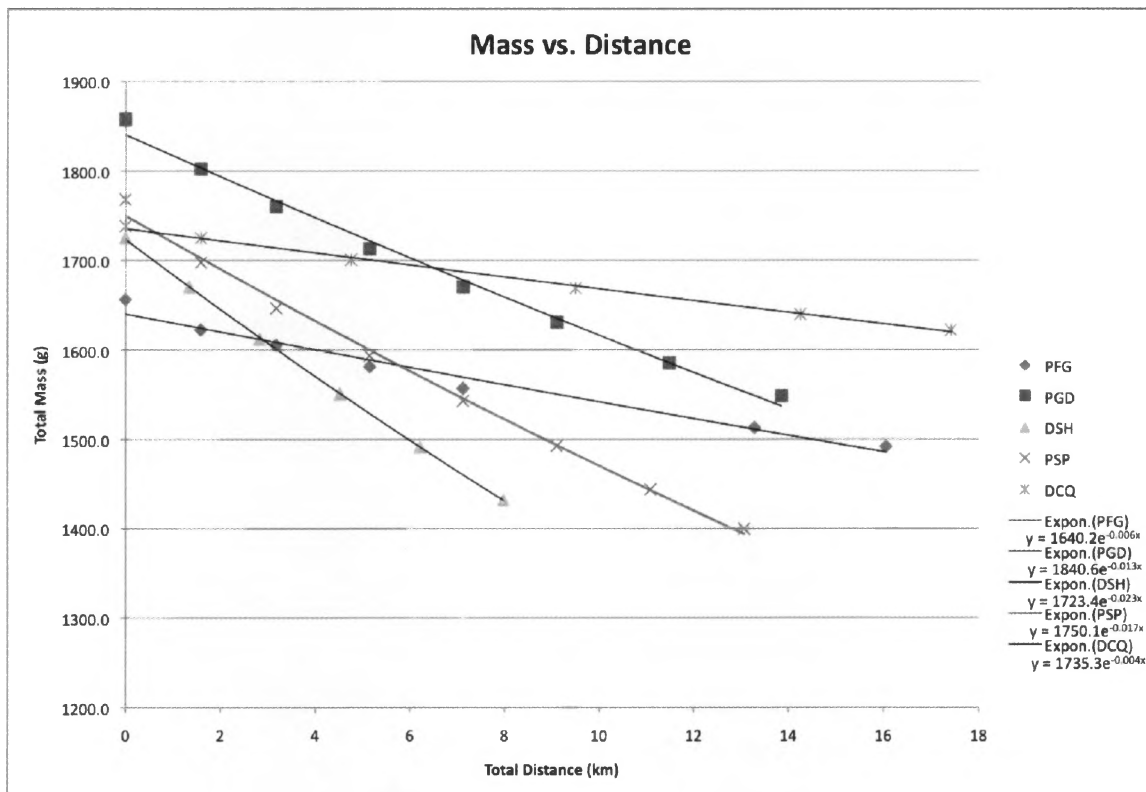


Figure 32: Total mass in tumbling barrel versus the total tumbled distance. Exponents of best-fit lines are the measured abrasion rates.

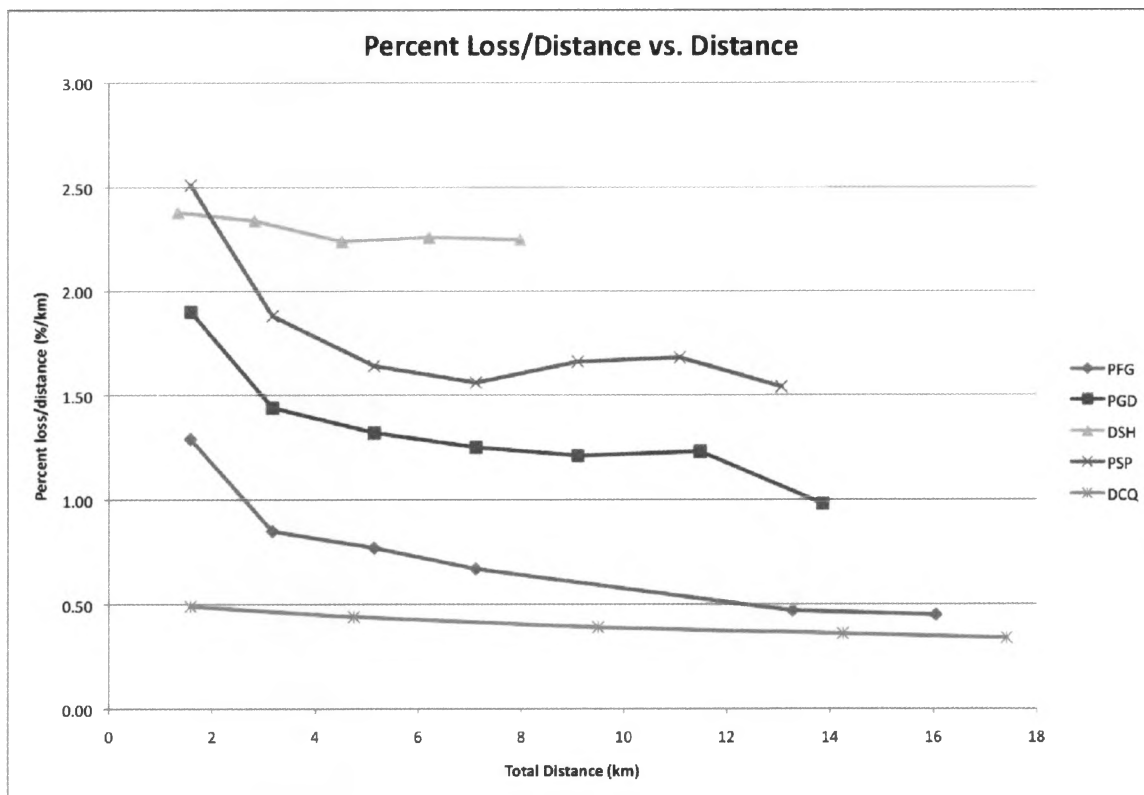


Figure 33: Abrasion rates (percent loss/distance) versus the total tumbled distance. Fresh angular fractured samples (sampled from a quarry in Big Creek, CA) were used for the tumbling experiments with the Providence rocks, whereas rounded stream gravels were used with the Dinkey Creek rocks. This explains the steep decrease in abrasion rates from the first to second data points, as the edges of the gravel clasts began to be rounded. The slight increase in abrasion rates seen in both the Prov. Ck granodiorite (PGD) and Prov. Ck diorite (PSP) represent clasts breaking into multiple pieces, larger than 2mm, but eventually abraded away through to the silt size range. No sand was produced in any of the tumbling experiments, only fine sediment.

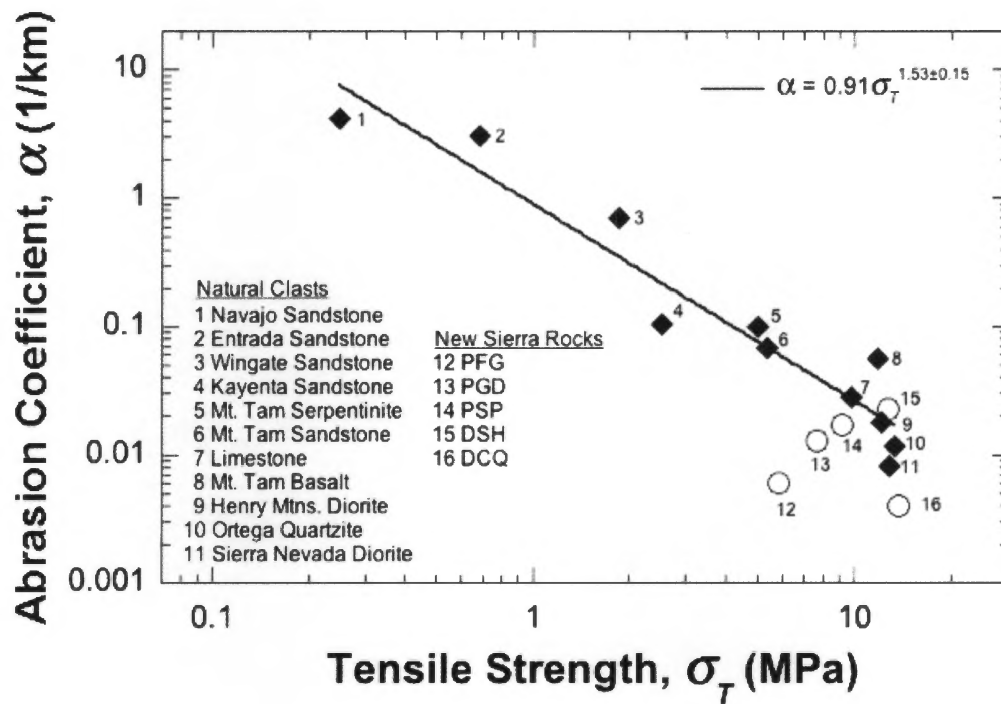


Figure 34: Experimentally measured abrasion rates vary with strength. Open circles represent new rocks collected from Providence and Dinkey Creeks in the Sierra National Forest, CA.

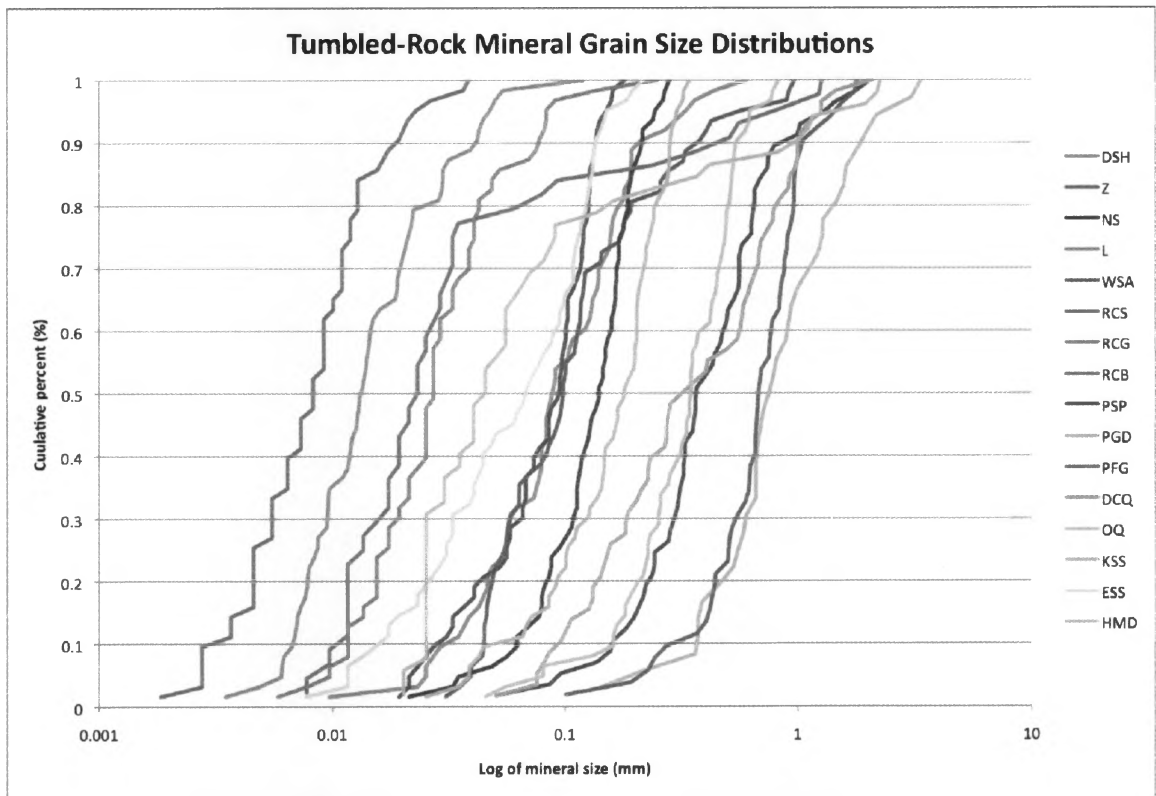


Figure 35: Tumbled data set cumulative mineral size distributions.

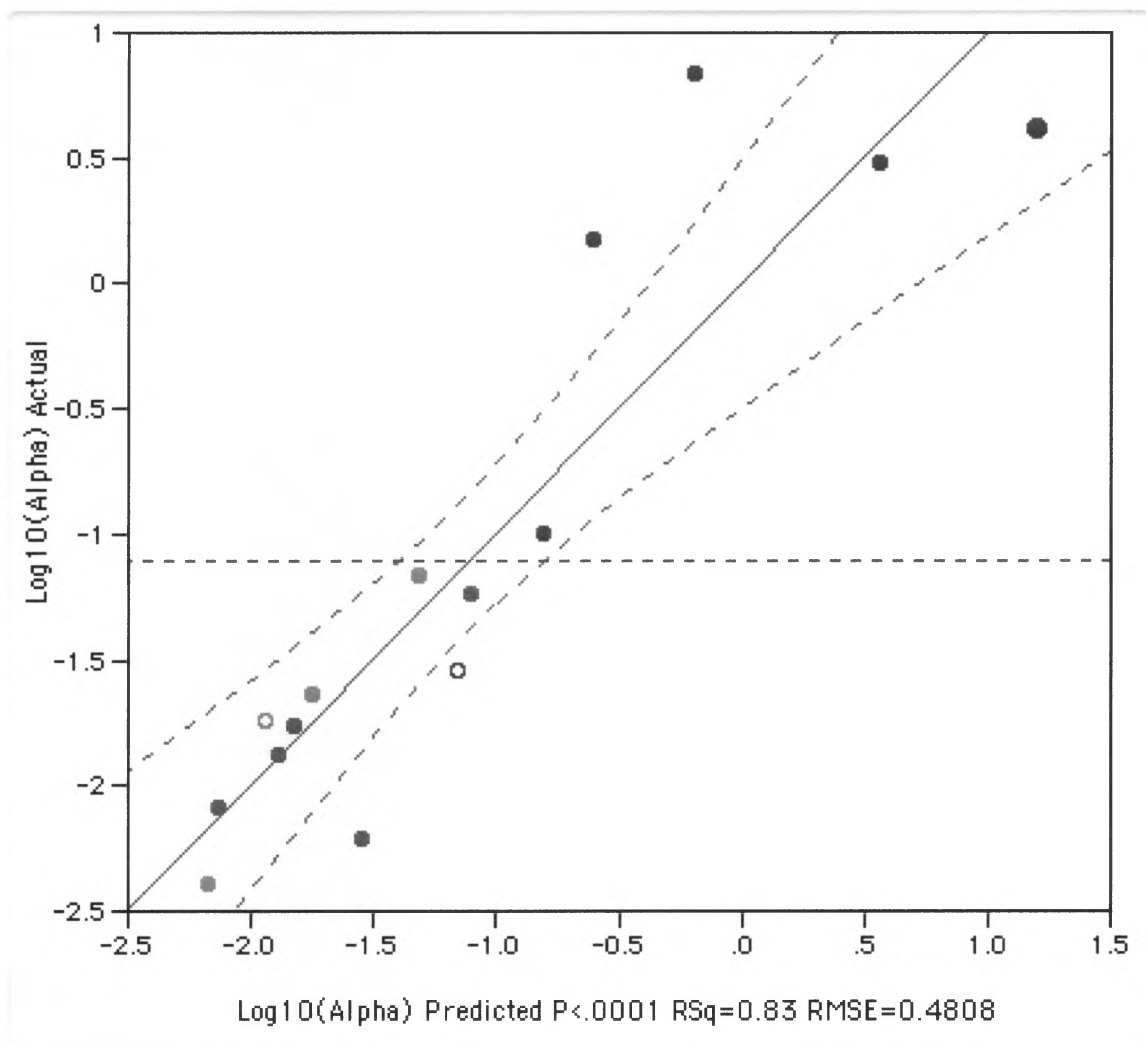
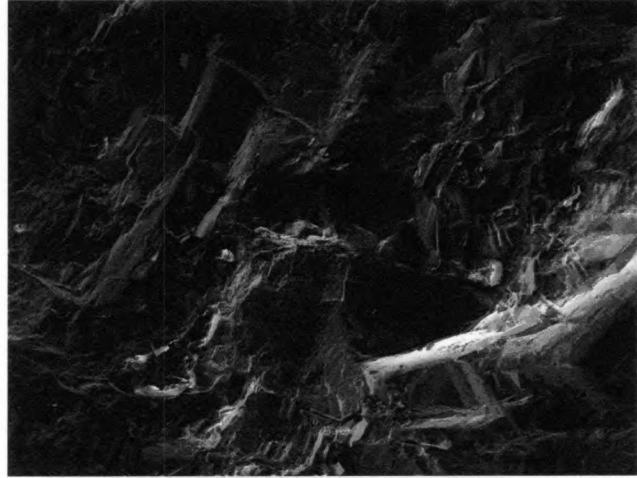
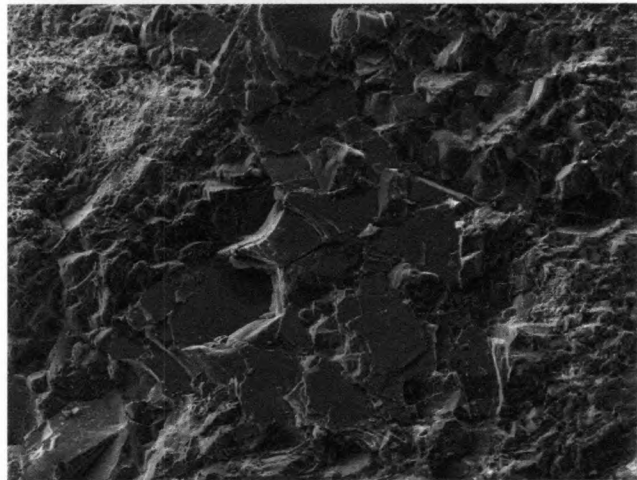


Figure 36: JMP statistical output regression of measured sediment abrasion rates vs. multivariate model in Log-Log space. The model yielding the best parameter estimates and R^2 value (0.83) models erosion as a function of strength and grain size. Modeling erosion only with strength, for the same data points, yields an R^2 value of 0.75; so grain size explains a third (~ 0.08) of the remaining variance. Red, green, and blue represent igneous, metamorphic, and sedimentary rocks. Open circles represent calcite cement, versus silica.

A) Prov. Ck. diorite after ~1 km:



After ~7.5 km of tumbling:



After ~13 km of tumbling:

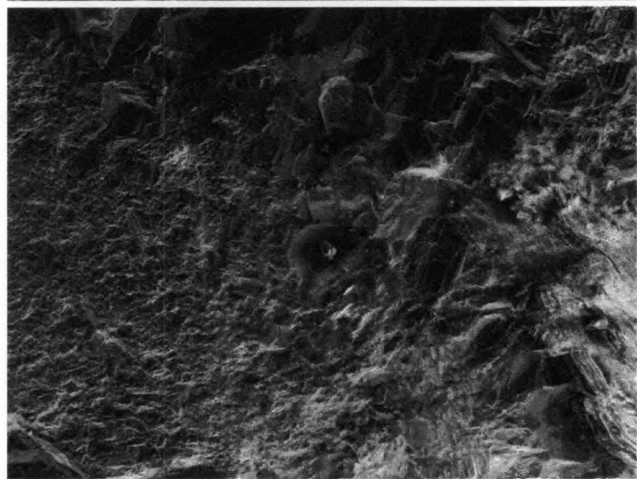
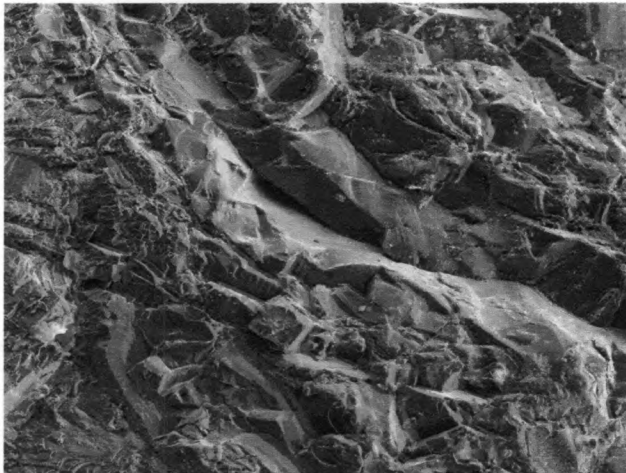
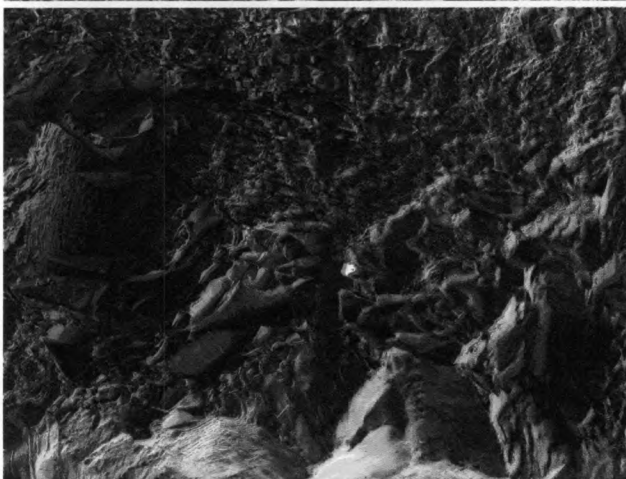


Figure 37: Corresponding anaglyphs of tumbling surface textures, from Figure30.

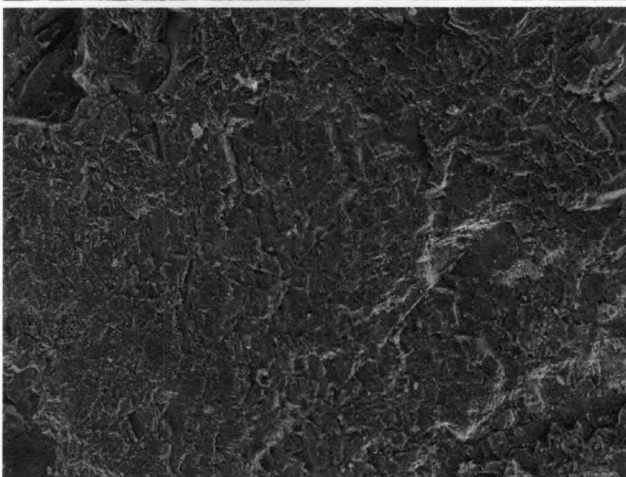
B) Prov. Ck. granite after ~1 km:



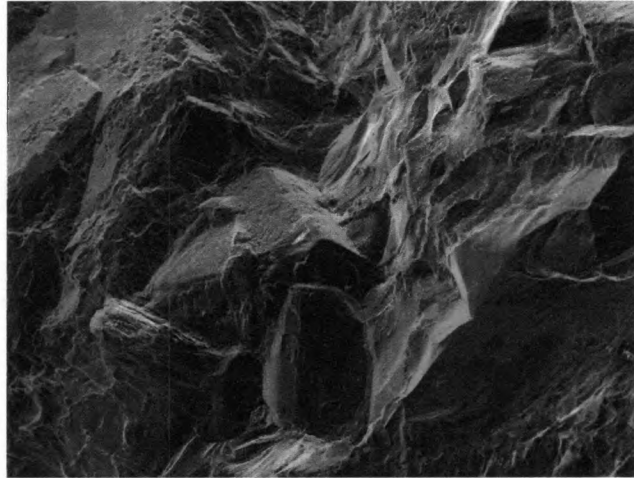
After ~7.5 km of tumbling:



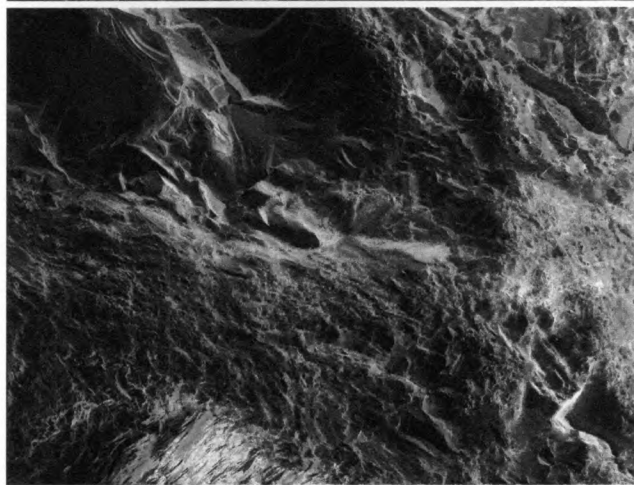
After ~14 km of tumbling:



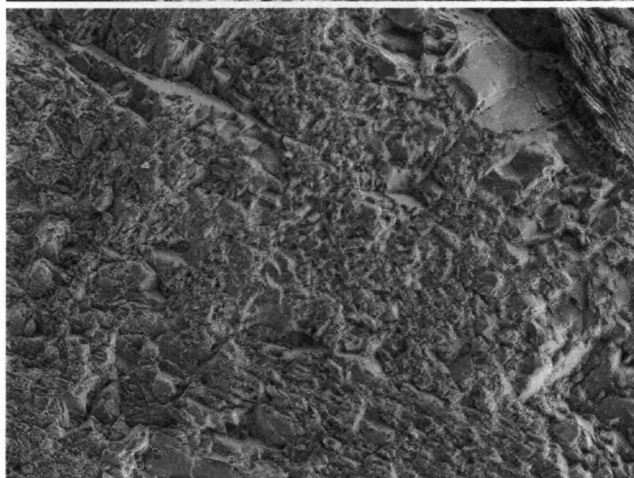
C) Prov. Ck. granodiorite after ~1 km:

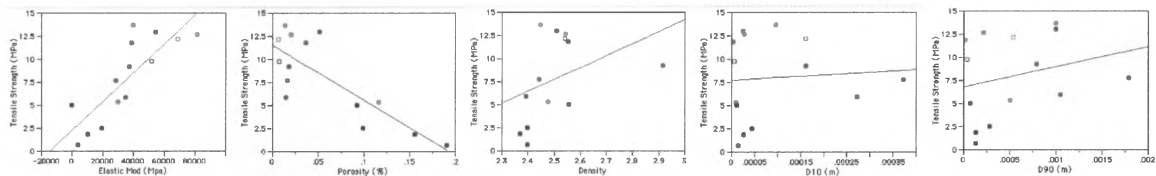


After ~7.5 km of tumbling:

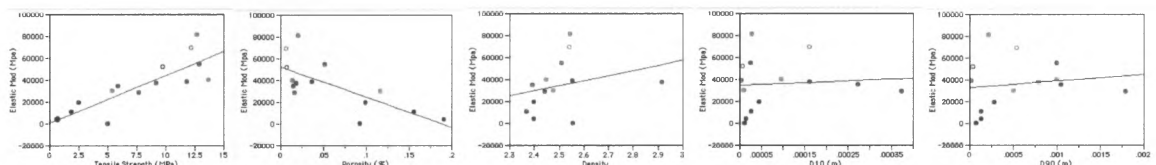


After ~13.5 km of tumbling:

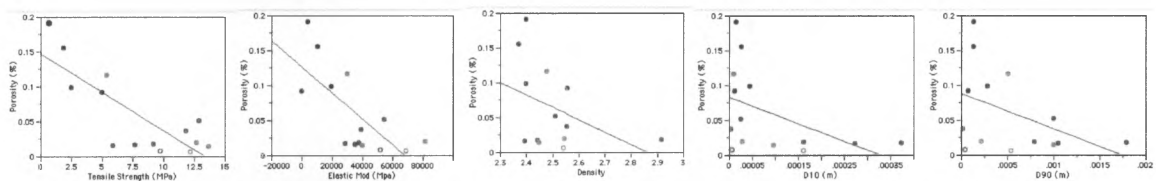




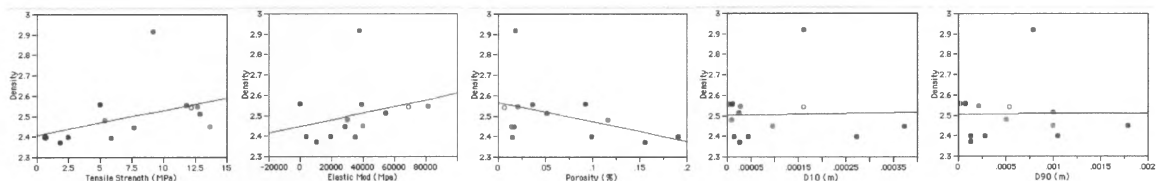
Covariation of properties with tensile strength as dependent variable.



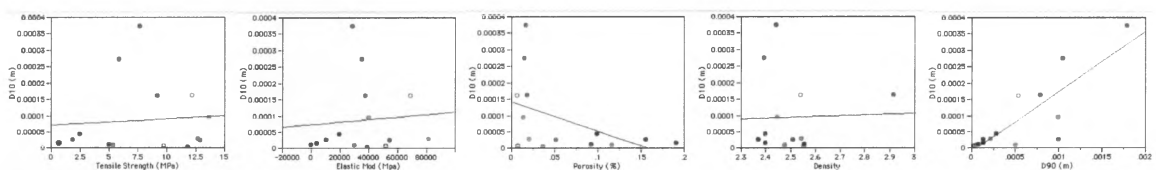
Covariation of properties with elastic modulus as dependent variable.



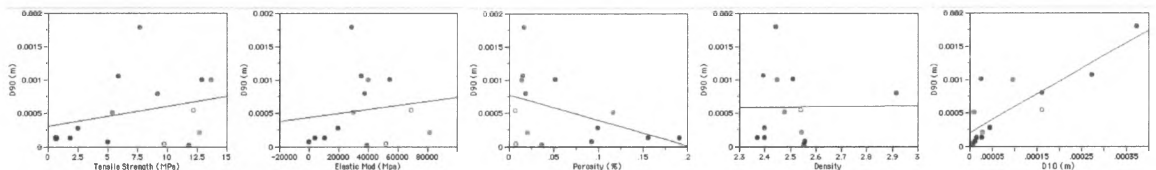
Covariation of properties with porosity as dependent variable.



Covariation of properties with density as dependent variable.



Covariation of properties with 10th quantile of grain size as dependent variable.



Covariation of properties with 90th quantile of grain size as dependent variable.

Figure 38: Covariation of measured rock properties of sediment dataset, including: tensile strength, elastic modulus, porosity, density, and grain size examined as D10 and D90.

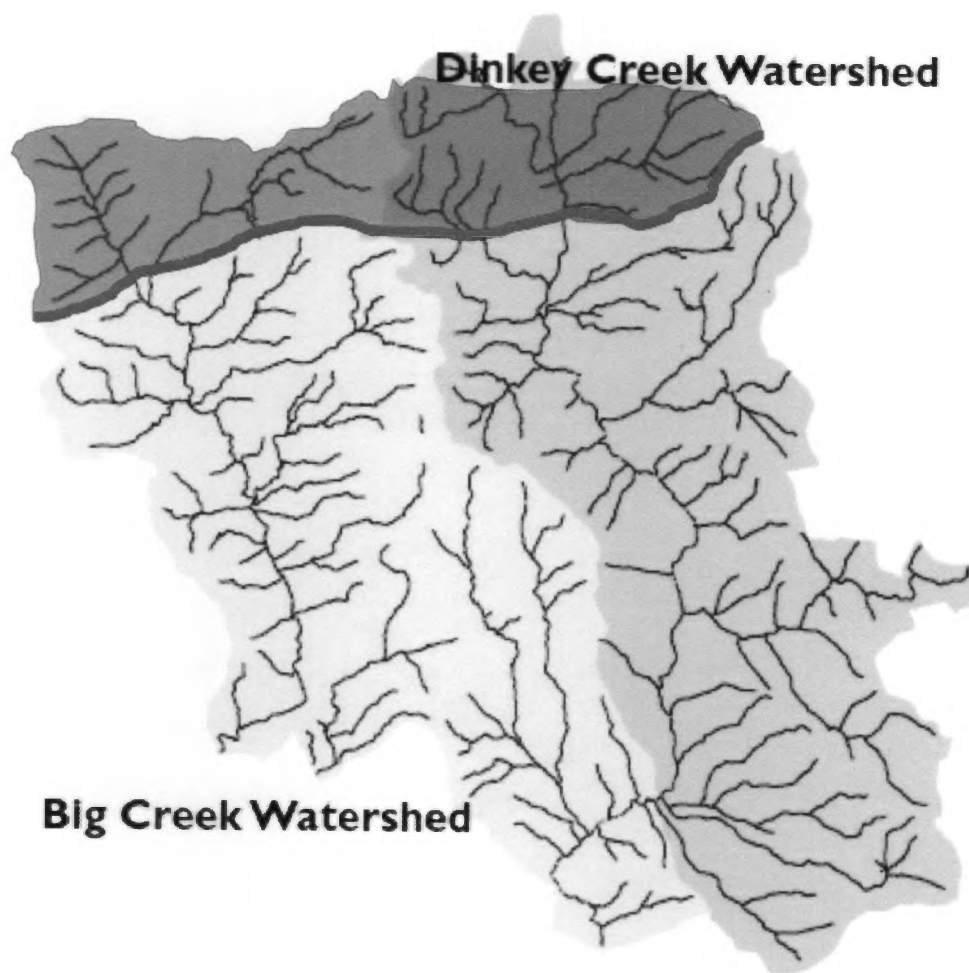


Figure 39: Schematic of the simplest form of a restricted source area; rivers flow generally southwards. Red line represents hypothetical lithologic contact limiting the red rock type to the headwaters of both watersheds. Modified from Gallegos (2002).



Figure 40: Photo showing country rock xenolith suspended in igneous intrusive basement rock.

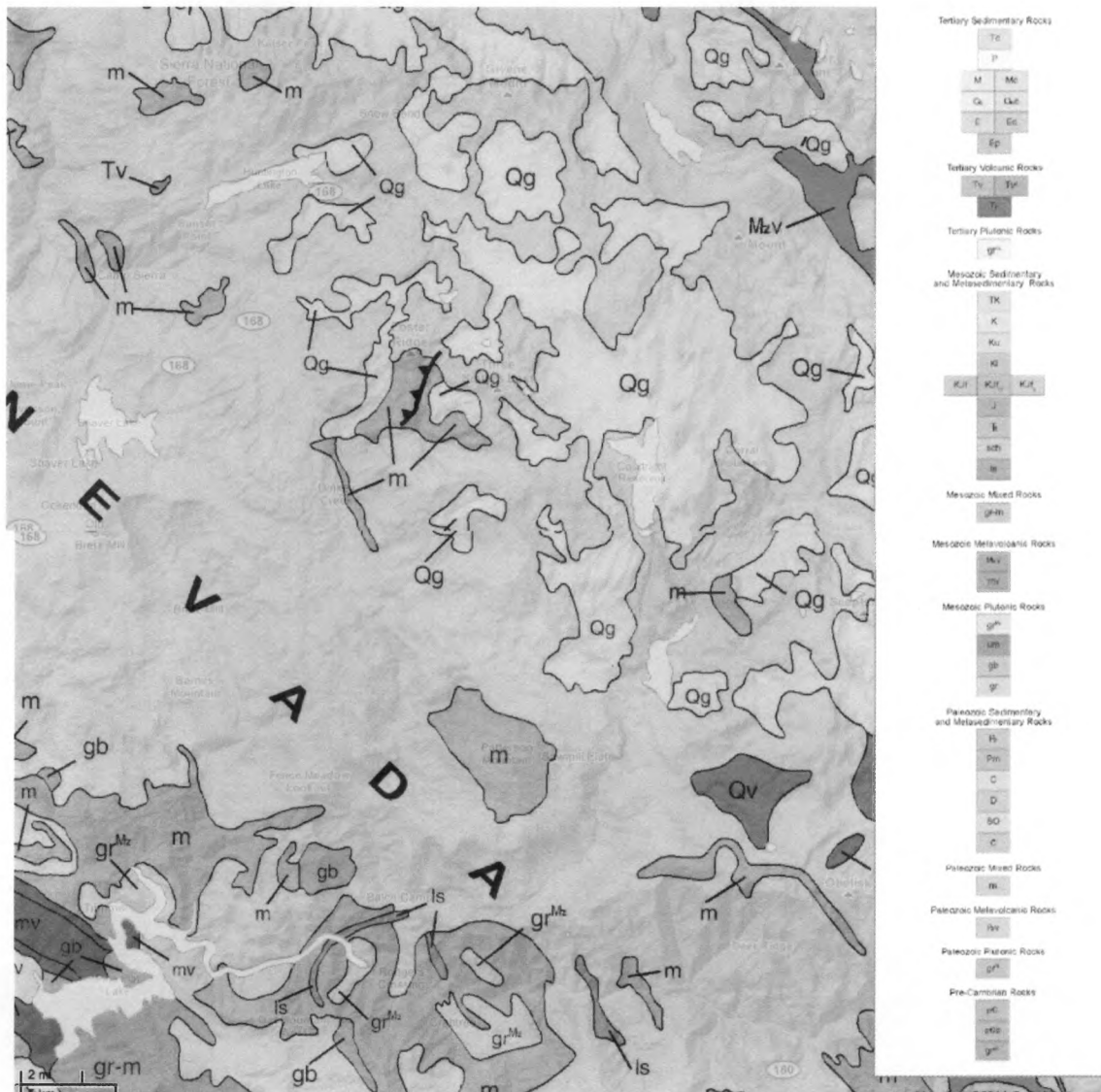


Figure 41: Generalized geologic map of Dinkey Creek field area, CA; from California Geologic Survey (*Strand, 1967*). Dinkey Creek flows from the middle of the map south and meets the North Fork of the Kings River before it flows into Pine Flats Reservoir. The roof pendant rocks are mostly restricted to the headwaters in the Dinkey Creek watershed, as well as high-elevation ridges and peaks.

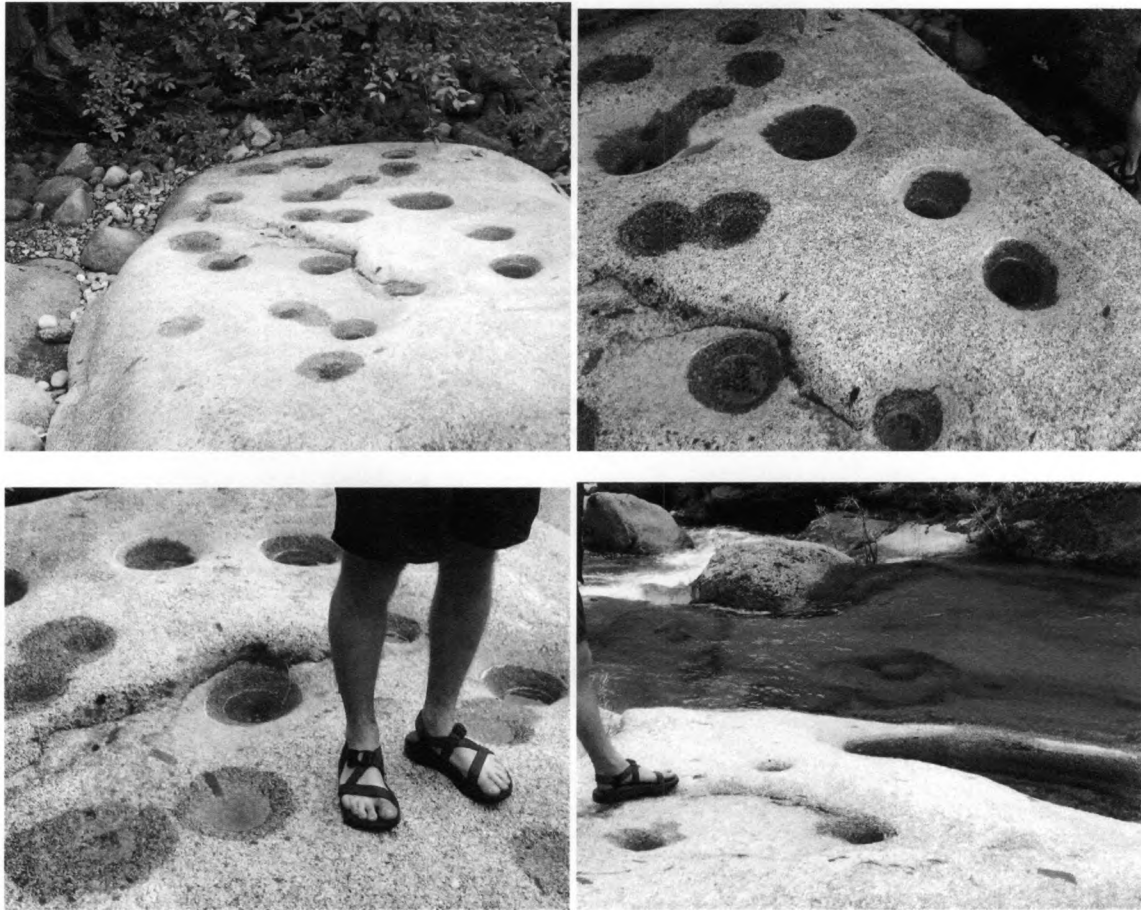


Figure 42: Native American grinding pits in Dinkey Creek granodiorite along channel margin, submerged at higher river discharges and showing asymmetrical abrasion, concentrated on the downstream side (upper right in top images, upper left in bottom).

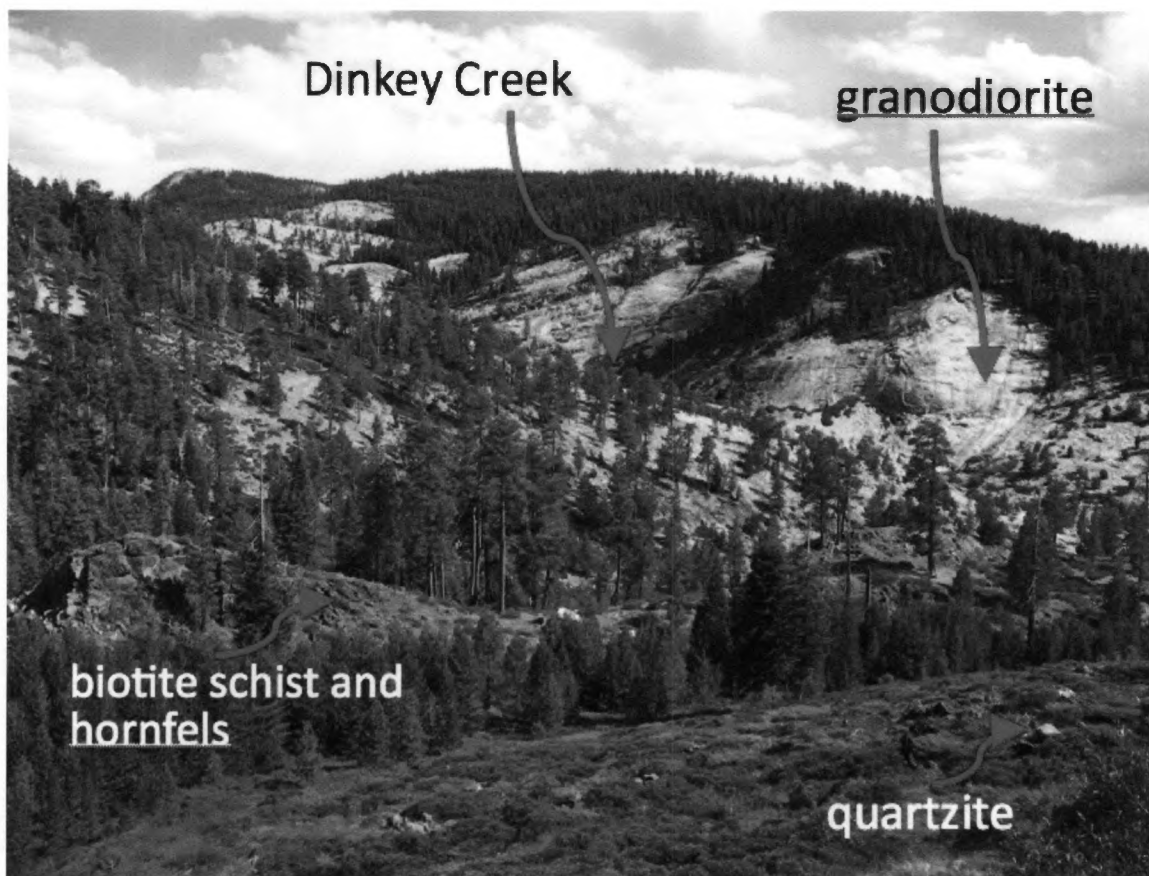


Figure 43: Headwaters of Dinkey Creek where biotite hornfels crop out and quartzite boulders are present on the surface as glacial deposits.



Figure 44: Generalized geologic map of Dinkey Creek field area, CA, showing topography and tributaries with potential resupply of roof pendant sediment. From California Geological Survey (*Strand, 1967*).

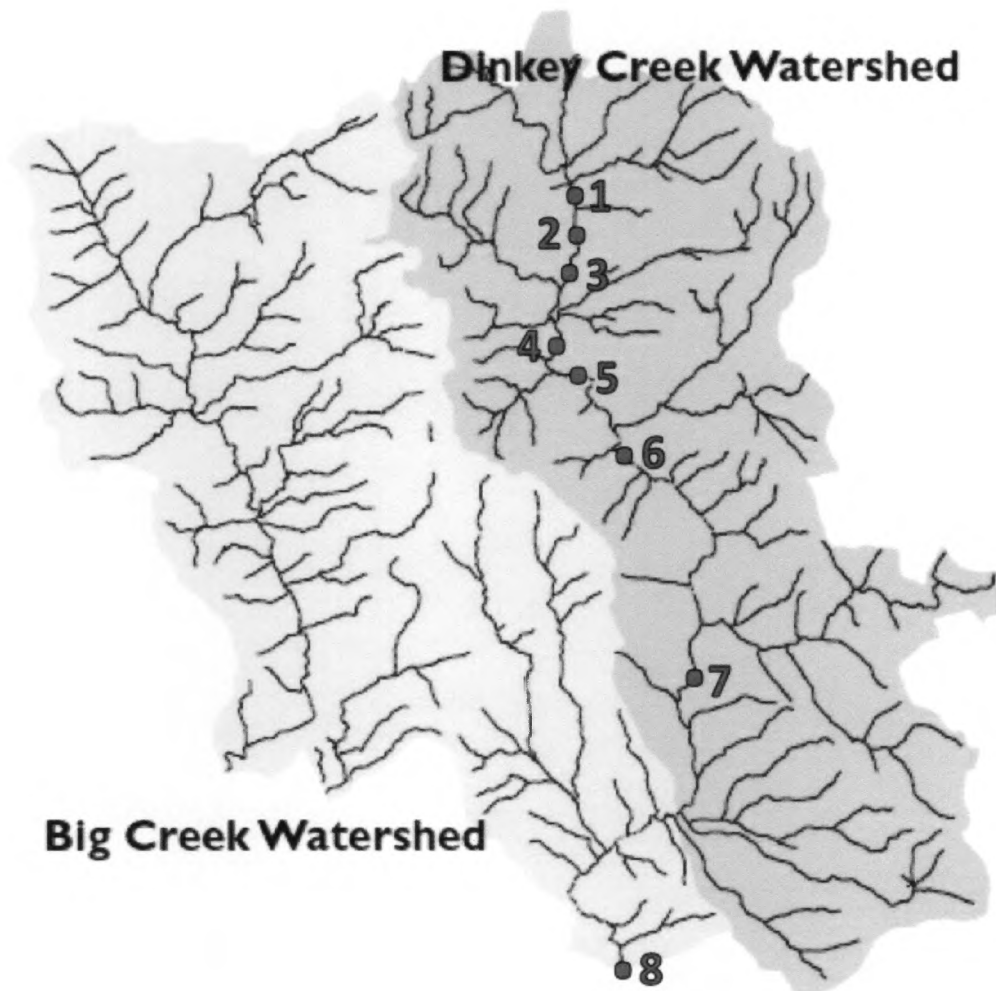


Figure 45: Pebble-count sites along Dinkey Creek, modified from Gallegos (2002).

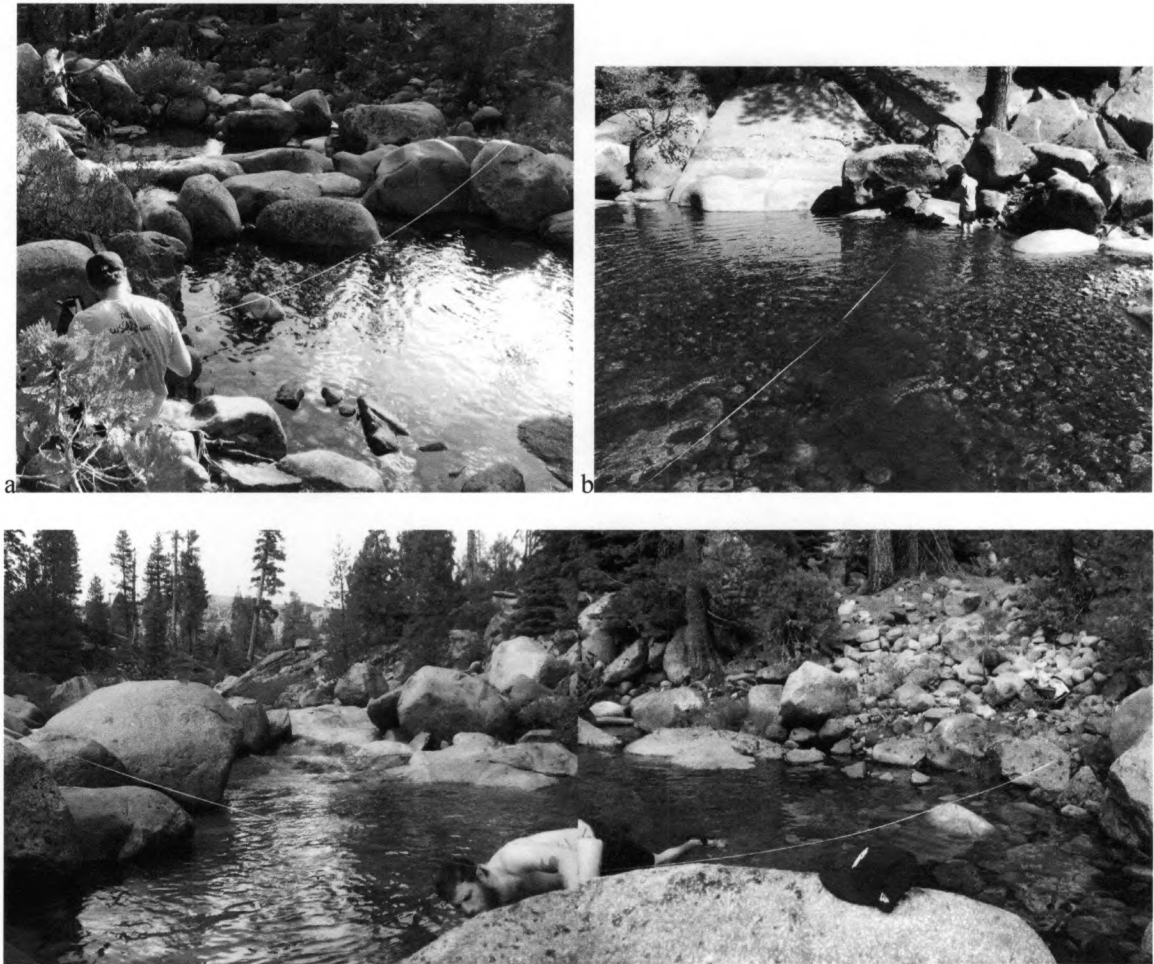
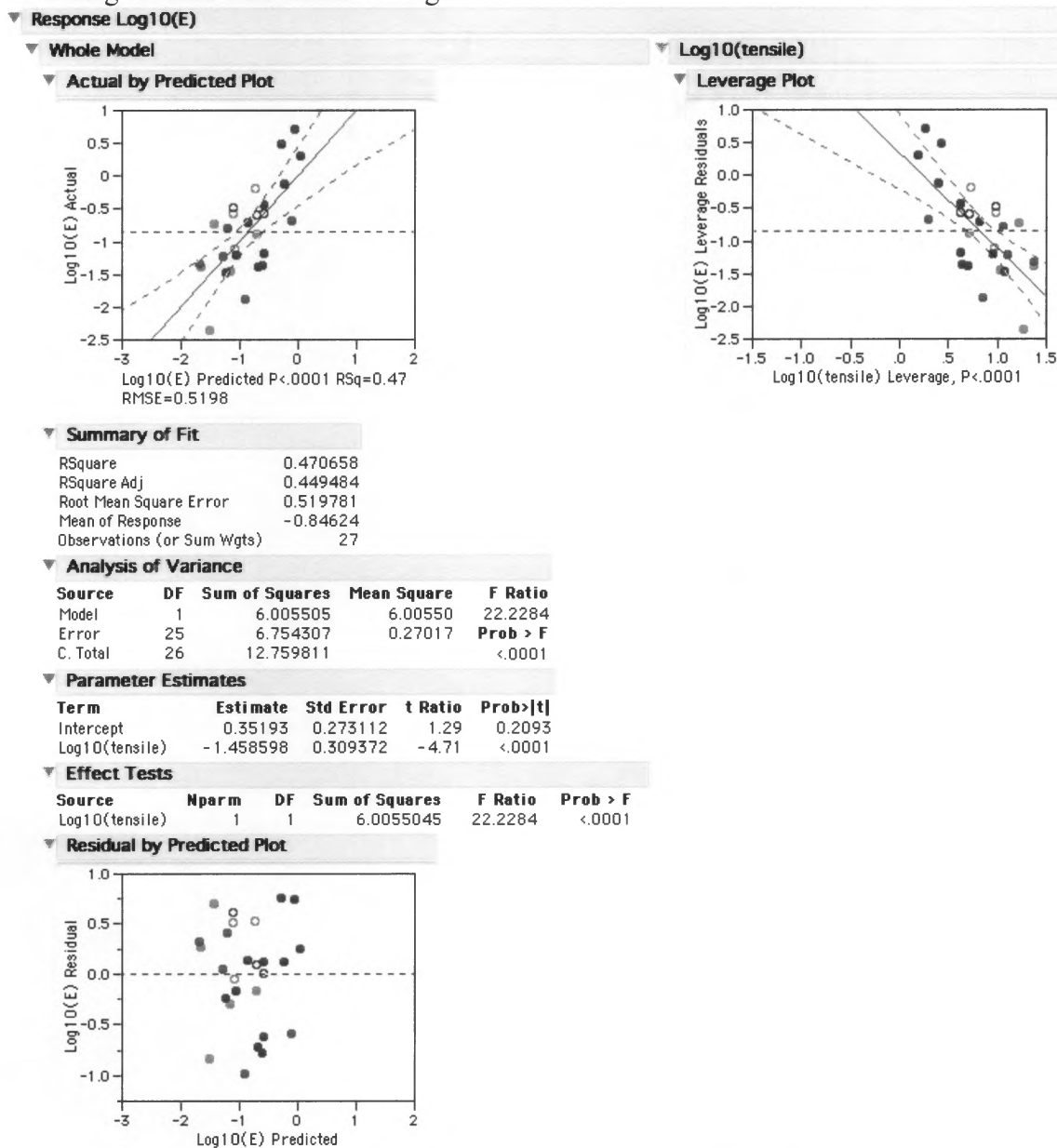


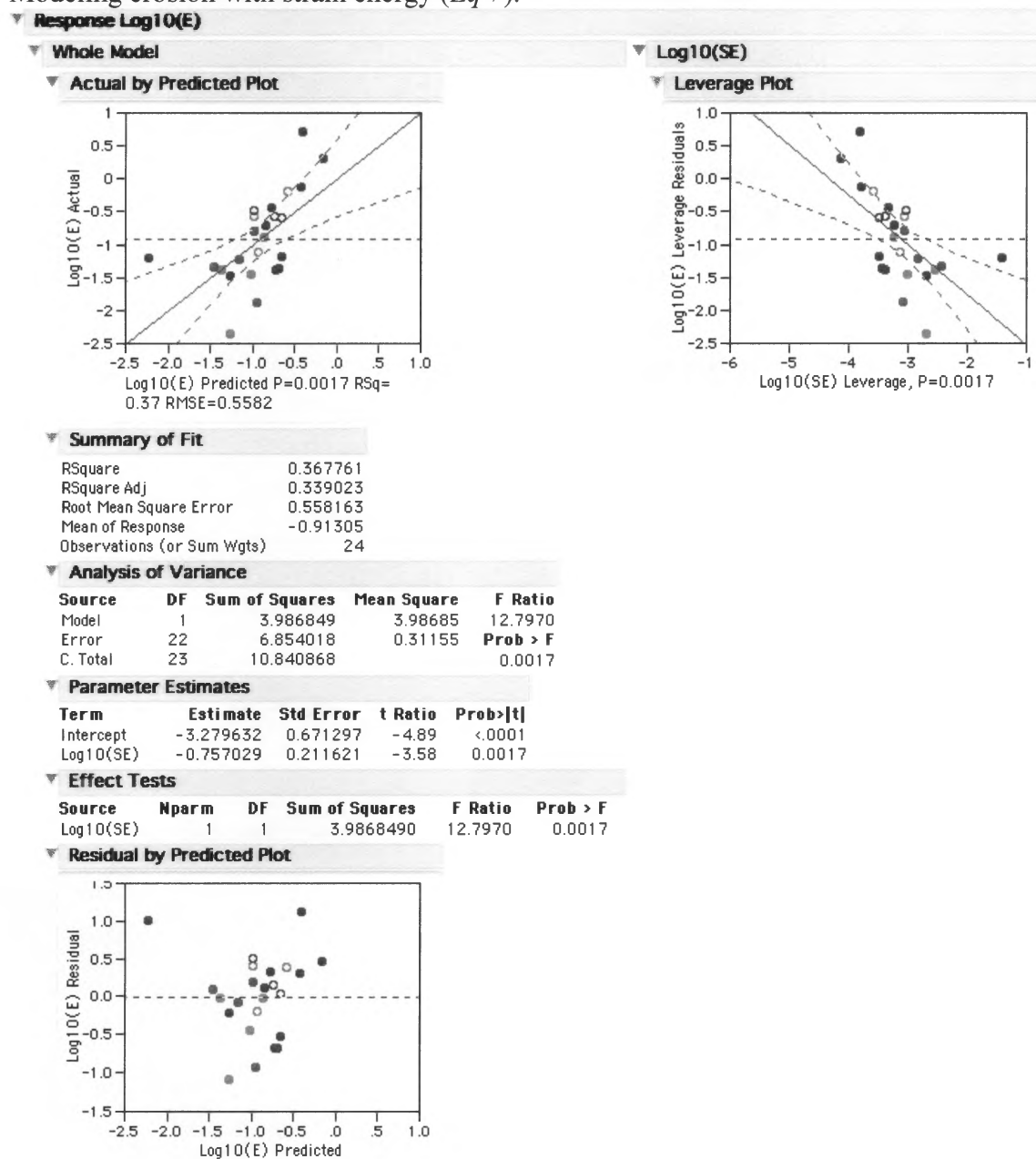
Figure 46: Photos of some pebble-count sites upstream (a) and downstream (b) along Dinkey Creek.

Appendix 1: JMP journals of various multiple regression model outputs for the bedrock dataset, with the best-fit model explanation at the end.

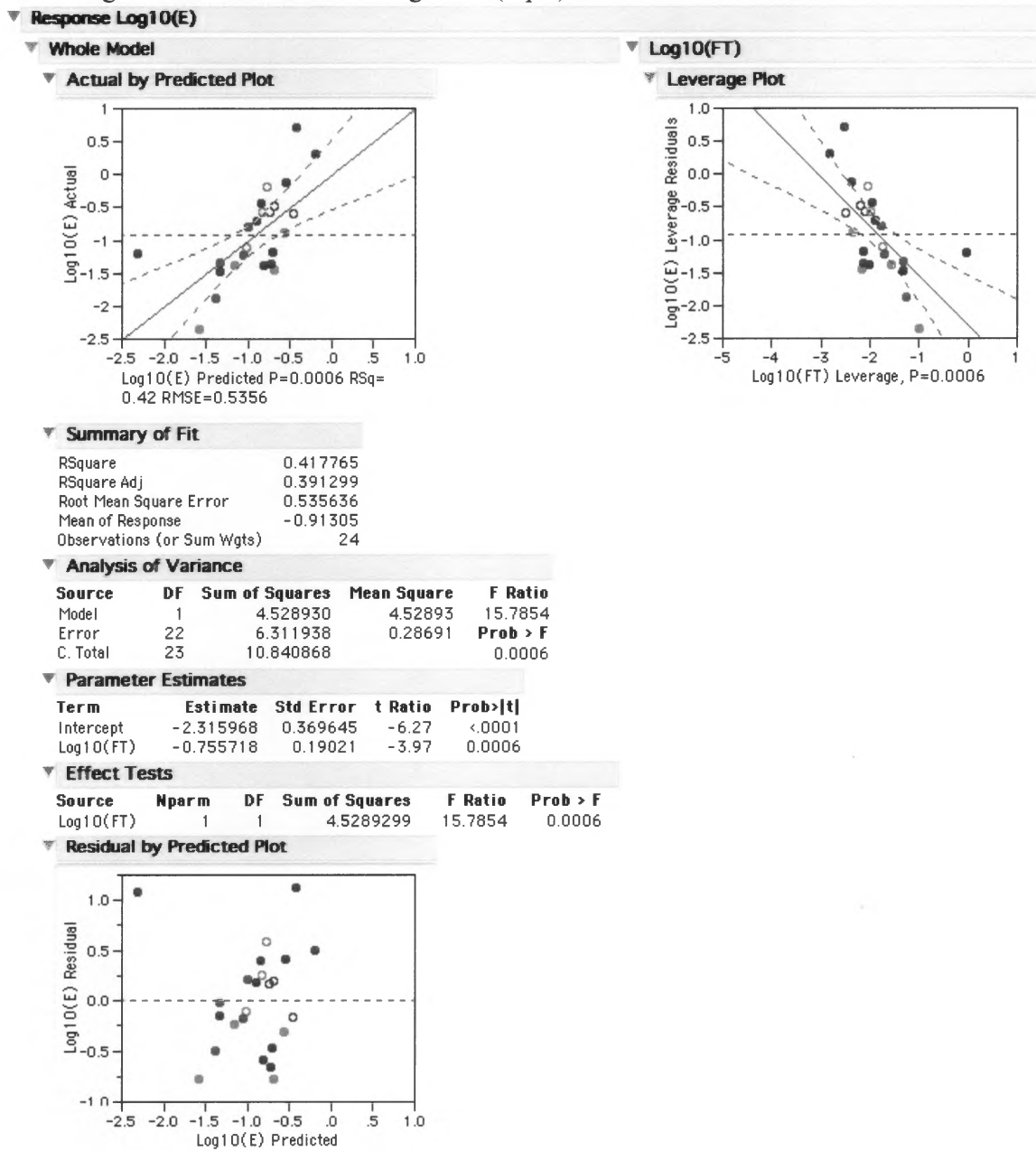
Modeling erosion with tensile strength.



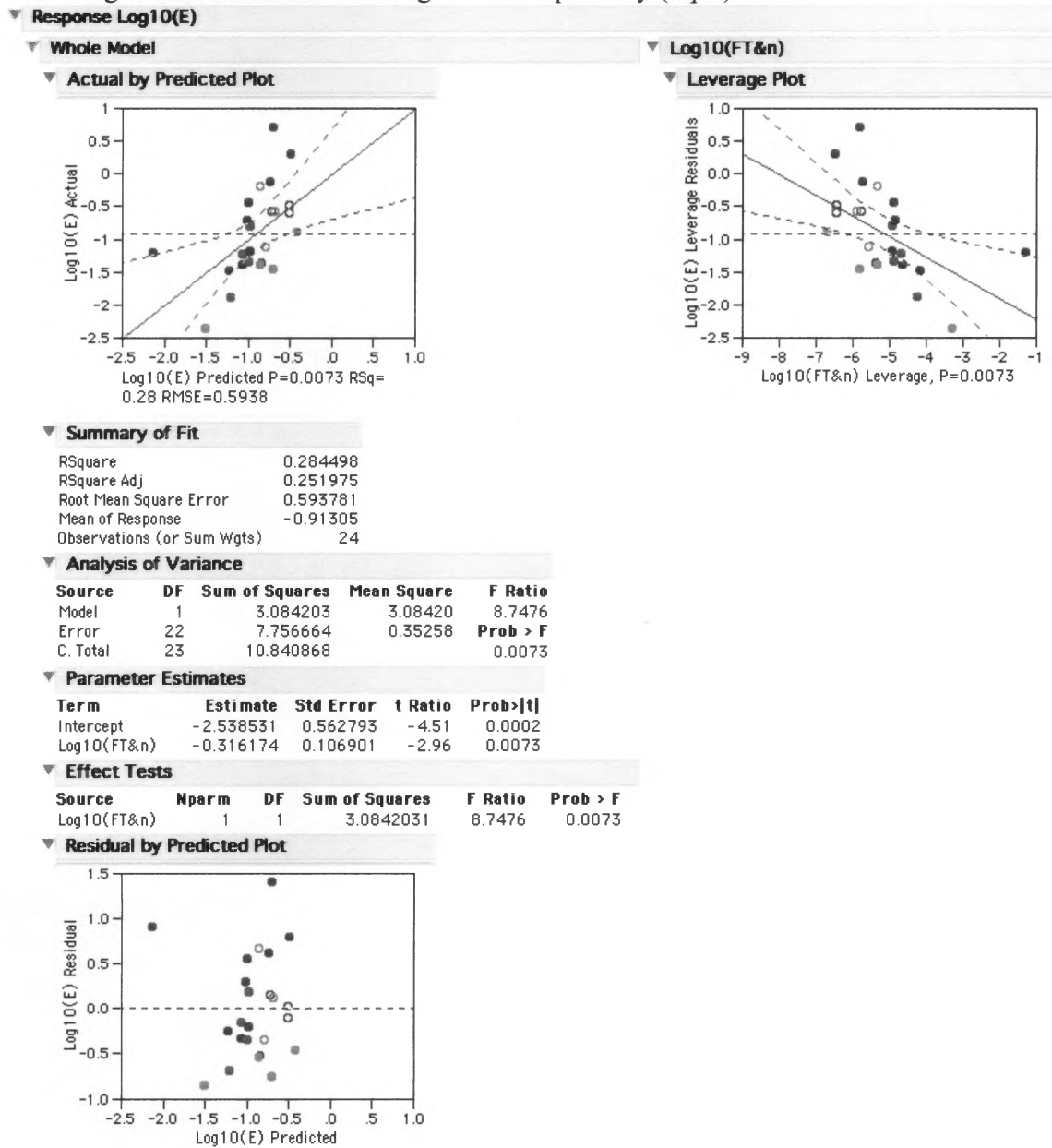
Modeling erosion with strain energy (*Eq 7*).



Modeling erosion with fracture toughness (Eq 8).



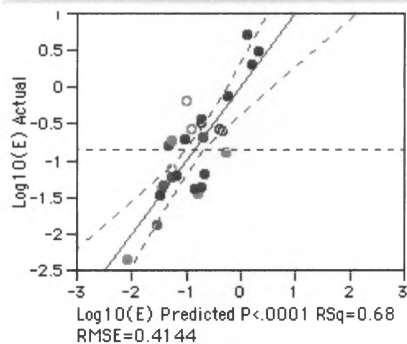
Modeling erosion with fracture toughness and porosity (Eq 9).



Modeling erosion with tensile strength and grain size.

▼ Whole Model

▼ Actual by Predicted Plot



▼ Summary of Fit

RSquare	0.677047
RSquare Adj	0.650134
Root Mean Square Error	0.414368
Mean of Response	-0.84624
Observations (or Sum Wgts)	27

▼ Analysis of Variance

Source	DF	Sum of Squares	Mean Square	F Ratio
Model	2	8.638993	4.31950	25.1571
Error	24	4.120818	0.17170	Prob > F
C. Total	26	12.759811		<.0001

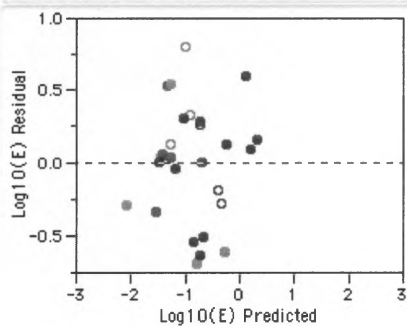
▼ Parameter Estimates

Term	Estimate	Std Error	t Ratio	Prob> t
Intercept	-2.049658	0.650728	-3.15	0.0043
Log10(tensile)	-1.641365	0.251007	-6.54	<.0001
Log10(D10)	-0.568427	0.145143	-3.92	0.0007

▼ Effect Tests

Source	Nparm	DF	Sum of Squares	F Ratio	Prob > F
Log10(tensile)	1	1	7.3419361	42.7601	<.0001
Log10(D10)	1	1	2.6334886	15.3377	0.0007

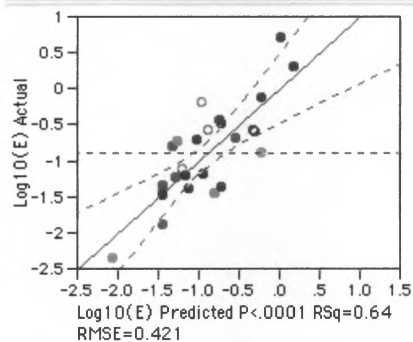
▼ Residual by Predicted Plot



Modeling erosion with tensile strength, grain size and porosity.

▼ **Whole Model**

▼ **Actual by Predicted Plot**



▼ **Summary of Fit**

RSquare	0.64281
RSquare Adj	0.594102
Root Mean Square Error	0.421017
Mean of Response	-0.89746
Observations (or Sum Wgts)	26

▼ **Analysis of Variance**

Source	DF	Sum of Squares	Mean Square	F Ratio	Prob > F
Model	3	7.017856	2.33929	13.1973	
Error	22	3.899611	0.17726		
C. Total	25	10.917468			<.0001

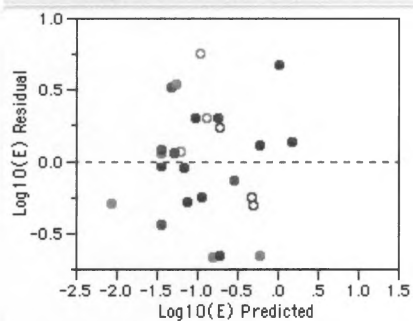
▼ **Parameter Estimates**

Term	Estimate	Std Error	t Ratio	Prob> t
Intercept	-1.499093	0.824841	-1.82	0.0828
Log10(tensile)	-1.761019	0.307812	-5.72	<.0001
Log10(D10)	-0.52706	0.161193	-3.27	0.0035
knudsen(n)	-0.190756	0.183072	-1.04	0.3087

▼ **Effect Tests**

Source	Nparm	DF	Sum of Squares	F Ratio	Prob > F
Log10(tensile)	1	1	5.8017063	32.7308	<.0001
Log10(D10)	1	1	1.8950672	10.6912	0.0035
knudsen(n)	1	1	0.1924484	1.0857	0.3087

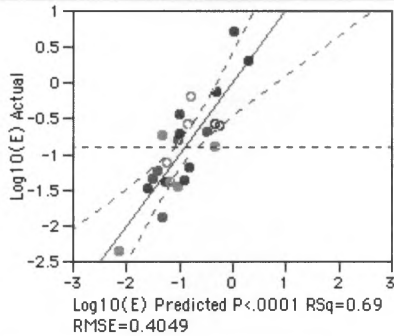
▼ **Residual by Predicted Plot**



Best model for erosion combines tensile strength, grain size, and density (Eq 14).

▼ **Whole Model**

▼ **Actual by Predicted Plot**



▼ **Summary of Fit**

RSquare	0.691767
RSquare Adj	0.645532
Root Mean Square Error	0.404923
Mean of Response	-0.90128
Observations (or Sum Wgts)	24

▼ **Analysis of Variance**

Source	DF	Sum of Squares	Mean Square	F Ratio	Prob > F
Model	3	7.359607	2.45320	14.9620	
Error	20	3.279248	0.16396		
C. Total	23	10.638855			<.0001

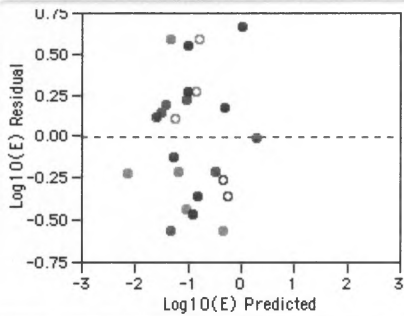
▼ **Parameter Estimates**

Term	Estimate	Std Error	t Ratio	Prob> t
Intercept	-4.605257	1.476802	-3.12	0.0054
Log10(tensile)	-1.952936	0.307899	-6.34	<.0001
Log10(D10)	-0.457418	0.162051	-2.82	0.0105
Density	1.2974373	0.615612	2.11	0.0479

▼ **Effect Tests**

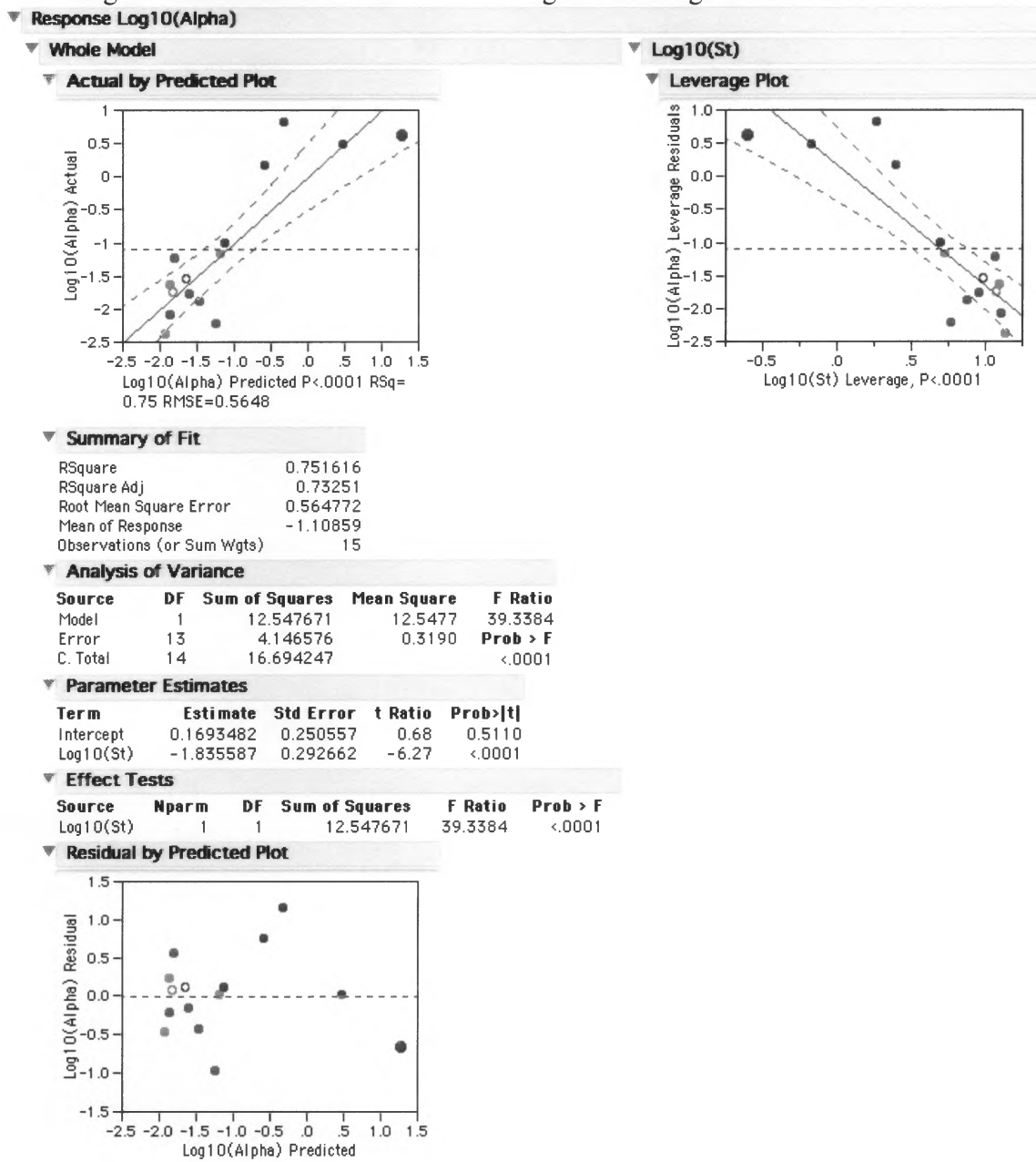
Source	Nparm	DF	Sum of Squares	F Ratio	Prob > F
Log10(tensile)	1	1	6.5963532	40.2309	<.0001
Log10(D10)	1	1	1.3063802	7.9676	0.0105
Density	1	1	0.7282873	4.4418	0.0479

▼ **Residual by Predicted Plot**



Appendix 2: JMP journals of various multiple regression model outputs for sediment abrasion with the best-fit model explanation at the end.

Modeling sediment abrasion with tensile strength is rather good.

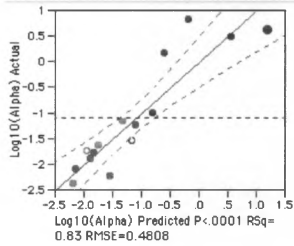


Modeling sediment abrasion with tensile strength and grain size, both highly significant.

Response Log10(Alpha)

Whole Model

Actual by Predicted Plot



Summary of Fit

RSquare	0.833847
RSquare Adj	0.806154
Root Mean Square Error	0.480781
Mean of Response	-1.10859
Observations (or Sum Wgts)	15

Analysis of Variance

Source	DF	Sum of Squares	Mean Square	F Ratio
Model	2	13.920442	6.96022	30.1112
Error	12	2.773805	0.23115	Prob > F
C. Total	14	16.694247		<.0001

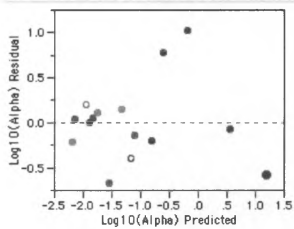
Parameter Estimates

Term	Estimate	Std Error	t Ratio	Prob> t
Intercept	-1.89569	0.873809	-2.17	0.0508
Log10(St)	-1.725403	0.253208	-6.81	<.0001
Log10(D90)	-0.560608	0.230042	-2.44	0.0313

Effect Tests

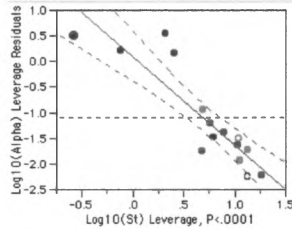
Source	Nperm	DF	Sum of Squares	F Ratio	Prob > F
Log10(St)	1	1	10.733006	46.4330	<.0001
Log10(D90)	1	1	1.372772	5.9389	0.0313

Residual by Predicted Plot



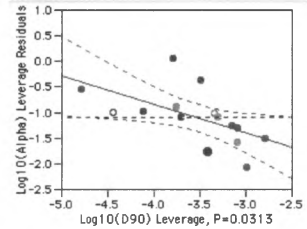
Log10(St)

Leverage Plot

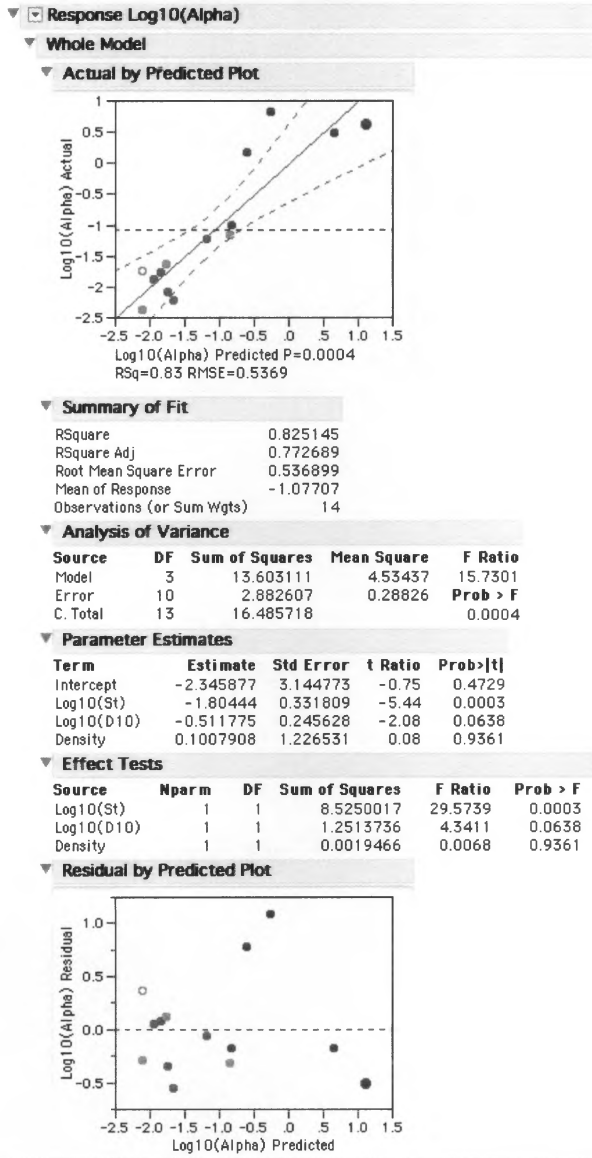


Log10(D90)

Leverage Plot



Modeling sediment abrasion with tensile strength, grain size, and density similar to results from bedrock erosion.

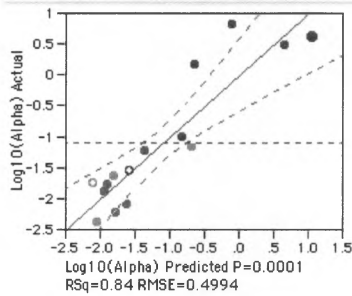


Modeling sediment abrasion with tensile strength, grain size, and porosity.

Response Log10(Alpha)

Whole Model

Actual by Predicted Plot



Summary of Fit

RSquare	0.835653
RSquare Adj	0.790831
Root Mean Square Error	0.499422
Mean of Response	-1.10859
Observations (or Sum Wgts)	15

Analysis of Variance

Source	DF	Sum of Squares	Mean Square	F Ratio	Prob > F
Model	3	13.950600	4.65020	18.6439	
Error	11	2.743647	0.24942		0.0001
C. Total	14	16.694247			

Parameter Estimates

Term	Estimate	Std Error	t Ratio	Prob> t
Intercept	-2.107915	1.002937	-2.10	0.0594
Log10(St)	-1.077025	0.824138	-1.31	0.2179
Log10(D10)	-0.300769	0.277116	-1.09	0.3010
Porosity (%)	5.9731372	6.313367	0.95	0.3644

Effect Tests

Source	Nparm	DF	Sum of Squares	F Ratio	Prob > F
Log10(St)	1	1	0.42597792	1.7079	0.2179
Log10(D10)	1	1	0.29381743	1.1780	0.3010
Porosity (%)	1	1	0.22326390	0.8951	0.3644

Residual by Predicted Plot

